Towards Quantitative Assessment of Human Functional Brain Development in the First Years of Life

Wei Gao

A dissertation submitted to the faculty of the University of North Carolina at Chapel Hill in partial fulfillment of the requirements for the degree of Doctor of Philosophy in the Department of Biomedical Engineering.

Chapel Hill
2010

Approved by:

Weili Lin

Hongtu Zhu

John H. Gilmore

Dinggang Shen

J. Keith Smith

David S. Lalush

Marija Ivanovic

©2010
Wei Gao
ALL RIGHTS RESERVED

ABSTRACT

Wei Gao
Towards Quantitative Assessment of Human Functional Brain Development in the First Years of Life
(Under the direction of Weili Lin)

Characterizing the developmental process of human brain function is of critical importance not only in gaining insight into its maturing architecture but also in providing essential age-specific information for assessment and monitoring of both normal and abnormal neurodevelopment. The recent development of non-invasive neuroimaging techniques, particularly resting-state functional connectivity magnetic resonance imaging (rfcMRI) has opened a window into very early functional brain development. Together with diffusion tensor imaging (DTI), rfcMRI offers the unique opportunity to tackle a largely unknown area – early functional brain development as well as its structural underpinnings.

In this dissertation, both rfcMRI and DTI were utilized to delineate early brain development. Structurally, we found that white matter fiber tracts experience most rapid axonal development as well as myelination in the first year, followed by a much slower but steady growth thereafter. Spatially, the central white matter tracts develop earlier than the peripheral ones.

Functionally, by focusing on one of the most salient high-order cognitive networks during the resting condition (absence of any goal-directed tasks) – the "default-

mode" network, our results showed early emergence of this network in neonates, followed by dramatic synchronization during the first year of life and an adult-like architecture in 2yr olds regarding the core regions. Moreover, we found the anti-correlation (competing functions) between the default network and the task positive network is largely mediated by the frontal-parietal control system using both regional and newly designed network-level approaches, shedding light on brain's functional interaction patterns at a network level. Finally, focusing on the whole brain architecture, our results showed interesting patterns of brain's functional organization development. Specifically, the brain's functional architecture develops from more anatomically sensible to more functionally sensible; for the functional hubs, they gradually shift from sensory-related cortices to higher-order cognitive function related cortices.

In conclusion, by focusing on neural circuit development at regional, network as well as whole brain levels and coupling with structural elements, our results delineated interesting and important functional circuits growth patterns and may shed light on the potential principles guiding normal early brain functional development.

A WORD OF GRATITUDE

Coming through the whole process of my graduate study, I feel deeply grateful to my advisor Dr.Weili Lin for his generous support, sound guidance and inspiring discussions throughout my research, which make this final dissertation possible. I also greatly appreciate my committee members, Drs. Hongtu Zhu, Dinggang Shen, John Gilmore, Keith Smith, David Lalush, and Marija Ivanovic, for their great scientific input as well as generous personal help during my research.

I thank Dr. Kelly Giovanello for her expert advice and help in several of my projects. I also thank people in our imaging lab, Dinggang's IDEA lab and Hongtu's statistics lab, particularly Drs. Hongyu An, Yasheng Chen, Feng Shi, Pew-Thian Yap, Qingwei Liu, Guorong Wu, Hongjun Jia, Mr. Qian Wang, Mr. Cihat Eldeniz, and Ms.Ying Yuan, for all their support and help during the past years.

Finally I would dedicate this dissertation to my parents and my wife, Xin, for their dedicated, unconditional love and support, which make all things possible.

TABLE OF CONTENTS

Page

LIST OF TABLES

LIST OF FIGURES

Chapter 1

Introduction

The brain is a complex, structured and dynamic system supporting a variety of functions, ranging from low level sensory functions to high level cognition. Yet, to a large extent, our understanding of the brain remains rather limited. Microelectrode recording methods have been extensively utilized in animals to obtain a wealth of data depicting the spiking electrical activity at a single or multi-neuron level as well as the post-synaptic input signal from a neural population (e.g. local field potential (LFP)) (1-3). However, due to the invasive nature of this method, its application in human subjects is largely limited. EEG (Electroencephalography), on the other hand, is non-invasive and capable of measuring the electrical activity produced by the firing activities of the underlying neuron population. As a result, EEG has been proved successful in neuroscience research as well as in clinical applications (4-9), especially in the diagnosis of epilepsy (4-7), coma (10, 11), brain death (8, 9), etc. However, the poor spatial resolution of EEG largely prohibits region-specific interpretations of the underlying functional activity and hence greatly restricts its domain of application.

Based on the assumption of a coupling between neuronal activity and microcirculation and using de-oxygen hemoglobin as an endogenous contrast agent (12-14), functional magnetic resonance imaging (fMRI) emerges as a primary tool for neuroscience research. In particular, with its superb spatial and reasonable temporal

resolution as well as decent sensitivity to the underlying neuronal activity, it has become the method of choice for modern functional neuroimaging studies. Since then, numerous exciting findings regarding the localization of various specific brain functions have been accomplished, greatly enhancing our understanding of brain's functional topology (15-19).

More recently, Biswal et al (20) further initiated the study of "resting state functional connectivity MRI (rfcMRI)", where they found that even during an "idling" state, human brain demonstrates a "synchronized" structure that greatly resembles the functional "activation" pattern during task states. This finding broadly opens the door to go beyond the "localization" of certain brain function. With the development of this method, the neuroscience community has witnessed a great resurgence of interest in the study of the "intrinsic" organization of the brain's functional architecture (21-25). Among these, the most representative and seminal work is the notion of the default mode of brain function, coined by Raichle and colleagues (26, 27) where they have identified a set of brain regions that consistently increase activity (high cerebral blood flow) during the resting condition. Although using PET (positron emission Tomography) in their original study, the topology and structure of this particular network has been consistently detected and duplicated in rfcMRI studies (22, 24, 28). Moreover, its anti-correlation with the "task-positive" network has also been well characterized and indicated as one of the "intrinsic" properties of the human brain organization (23). Besides the default and the "task-positive" networks, studies have also found sets of different resting state networks (RSNs) with distinct spatial patterns corresponding to a variety of different functions, including motor-sensory(20), visual(29), attention(30), memory(31, 32),

among others. As a result, the brain's "modular" structure, i.e., there are different functional modules responsible for distinct brain functions, becomes increasingly accepted and experimentally validated in neuroscience community.

In addition to studying the matured brain functional organization, characterizing its corresponding developmental process is also of critical importance not only in gaining insight into its matured architecture but also in providing essential age-specific information for critical assessment and monitoring of both normal and abnormal development (33-35). For example, information can be gained to potentially reveal brain function that develops more rapidly, so as to determine when and how to intervene when needed. More importantly, such information may also reveal the time window of vulnerability to neurological disorders such as autism spectrum disorders (ASD) and attention deficit/hyperactivity disorder (ADHD), which is of great clinical interest in preventing and treating such developmental disorders. Together, the main focus of this dissertation is to provide quantitative evaluation of brain functional and structural development in normal pediatric subjects during the first years of life.

One of the central techniques towards such a quantitative exploration is rfcMRI(20). This technique is uniquely suitable for assessing early brain functional development as it is non-invasive and is conducted in the absence of any explicit task so that subjects can be in a naturally sleeping condition. On the other hand, neurophysiological development provides the structural basis for functional development. Specifically, white matter fibers - the structural pathway between functional regions, will also be studied using another important MRI technique - diffusion tensor imaging (DTI) (36, 37). Combing these two most recent MRI techniques specialized for studying

functional and structural connectivity, respectively, we hope to pave a way towards quantitative assessment of human brain functional development.

This dissertation is organized as follows: the first three chapters (2, 3, and 4) will present the background information on: the acquisition of DTI and fMRI signal; the neurophysiological underpinnings of BOLD signal and functional connectivity study; and the structural and functional early brain development, respectively, providing both theoretical and empirical basis for later discussion. Chapter 5 will focus on the spatial and temporal development pattern of white matter (WM) fiber properties during the first two years of life using DTI technique, providing the structural underpinnings of functional connectivity development. Chapter 6 will specifically delineate the emergence and developing pattern of the most salient and well documented "default-mode" network during the first two years of life, primarily due to its central role during the resting state; Chapter 7 is dedicated to the relationship between these two "competing brain networks" – dorsal attention and default networks, and test the hypothesis of whether frontal-parietal system mediates the interaction between the dorsal attention and default networks. In addition, a new multivariate approach is described as an extension of this chapter to specifically address the problem of network-level interaction, which is highly relevant given the network-centered analysis throughout this dissertation. Going beyond specific networks, Chapter 8 will provide a global picture of how the whole brain functional organization develops during the first two years of life and compares it with adult subjects aiming to reveal the underlying principles guiding development. From a perspective of image acquisition, Chapter 9 will describe a technical improvement on one

of the techniques used in this study: a unified method for DTI experiment optimization. Finally, Chapter 10 will present the concluding remarks and future directions.

Chapter 2
Diffusion Weighted Imaging (DWI) and Functional Magnetic Resonance Imaging (fMRI)

Since its discovery in the 1970's, magnetic resonance imaging (MRI) has become a versatile tool for various clinical and research applications. Arising from the local precession of proton assemblies, MRI provides a number of different contrast mechanisms through the manipulation of the bulk precession using different magnetic field combinations, which include different relaxation factors (T_1/T_2), susceptibility difference, magnetization transfer contrast, flow, contrast agent, and diffusion. Among these, diffusion weighted imaging (DWI), which is sensitive to the diffusion property of water molecules and functional magnetic resonance imaging (fMRI) which detects the local susceptibility changes under external sensory stimuli and/or performing cognitive tasks, are two of the widely applied MR techniques to probe brain white matter property/connectivity and function, respectively. In this chapter, the basic principles of MR signal detection and the underpinnings of the above mentioned two techniques are reviewed to provide necessary technical background for the following discussion.

2.1 General MR signal formation

2.1.1 Interaction of a proton spin with the magnetic field

The formation of MR signal relies on the interaction of a nuclear spin with an external magnetic field, $\vec{B}_0$. Given the natural abundance, the proton in hydrogen is selected as the primary nucleus in MR imaging. Precession, the circular motion of the

axis of a spinning body about another fixed axis caused by the presence of an external magnetic field, is the fundamental phenomena on which MR detects signal. Specifically, due to this circular motion, the charged spin possesses an effective current loop, which interacts with the external field as well as produces its own magnetic field and its strength is characterized in terms of the magnetic moment vector. This magnetic moment vector tends to align itself along the external magnetic field through a similar precession process and the angular frequency for this process is given by

$$\omega_0 = \gamma B_0 \tag{2.1}$$

where γ is a constant called the gyro magnetic ratio, which varies with nucleuses and this precession frequency is called Larmor frequency.

At the presence of an external magnetic field, the magnetic moment vector of a typical proton has only two possible energy states: parallel or anti-parallel. Due to the external field, this vector tends to align itself with it but this alignment is disrupted by the existence of thermal energy, which is millions of times larger than the quantum energy difference between parallel and anti-parallel alignments at the normal human body temperature. As a result, during an equilibrium state, there is only a tiny net portion of spins that have magnetic moment vector parallel to the external filed. Specifically, this excess is given by

$$spin\ excess \sim N \frac{\bar{h}\omega_0}{2kT} \tag{2.2}$$

where N is the total number of spins present in the sample, $\bar{h}$ is the Plank's quantum constant and T is temperature. At a magnetic field strength of 0.3 Tesla, this spin excess ratio is only one in a million. However, given the Avogadro numbers of protons in a few grams of sample, we can still detect signal despite this small ratio.

In order to detect signal, spins have to be set into precession, as described above. In MRI, this is achieved by applying another radiofrequency (rf) magnetic field for certain amount of time to "push" the magnetic moment vector of protons away from the longitudinal direction (the direction of the external magnetic field) so that the precessing spins can produce a changing flux in the receiver coil hence producing signal. This rf magnetic field is specifically tuned to be on "resonance" with the precession frequency of protons so that the spins can get a continuously synchronized "push". The magnetization produced by this rf pulse experiences different relaxations thereafter which therefore determine the signal strength that we can detect at a certain acquisition time.

2.1.2 Relaxation and Bloch Equation

Magnetization is a measure of local magnetic moment per unit volume and for a small enough volume that the external field can be viewed as approximately uniform, it is defined as

$$\vec{M} = \frac{1}{V}\sum_{\substack{proton\ i \\ in\ V}} \vec{\mu_i} \tag{2.3}$$

where $\vec{u_i}$ is the magnetic moment for each spin. Such a volume of spins is called a spin "isochromat" in which they are deemed to have the same phase. With the neglect of proton interactions with their environment, a sum over the equations of motions for the individual spins yields

$$\frac{d\vec{M}}{dt} = \gamma\vec{M} \times \overrightarrow{B_{ext}} \tag{2.4}$$

which can be decomposed into parallel and perpendicular components defined relative to the static external field

$$\frac{dM_z}{dt} = 0 \tag{2.5}$$

and

$$\frac{d\overrightarrow{M_{\perp}}}{dt} = \gamma\vec{M} \times \overrightarrow{B_{ext}} \tag{2.6}$$

However, consideration of the interactions of spins with either their surrounding environment or neighboring spins leads to additional terms in the above equations, which we termed as T_1 and T_2 relaxation, respectively. Generally, through the interaction/energy exchange with their surroundings (spin-lattice interaction, T_1 effect), the longitudinal (parallel) magnetization tends to realign itself with the external field through "re-growth" while through spin-spin interactions (T_2effect) transverse magnetization tends to dephase and decay to zero.

The re-growth rate due to the spin-lattice interaction is proportional to the difference $M_0 - M_z$. The proportionality constant is just T_1 and is empirically determined, which represents the inverse of the time scale of the re-growth rate:

$$\frac{dM_z}{dt} = \frac{1}{T_1}(M_0 - M_z) \tag{2.7}$$

The solution of equation 2.7 can be found as

$$M_z(t) = M_z(0)e^{-t/T_1} + M_0(1 - e^{-t/T_1}) \tag{2.8}$$

where M_0 is the equilibrium value.

The spin-spin interaction accounts for the decay of transverse magnetization. Specifically, since each spin experiences different local field as a combination of the applied field and the field of their neighboring spins, this field difference leads to phase differences for their precession and this "fanning out" effect on phase will finally result in a net reduction of transverse magnetization, which is simply a sum of all individual magnetic moment vectors. As a result, the transverse magnetization differential equation 2.6 is changed by the addition of a decay rate term:

$$\frac{d\overrightarrow{M_\perp}}{dt} = \gamma\vec{M} \times \overrightarrow{B_{ext}} - \frac{1}{T_2}\overrightarrow{M_\perp} \tag{2.9}$$

while in rotating reference frame, it has a standard decay-rate form:

$$(\frac{d\overrightarrow{M_\perp}}{dt})' = -\frac{1}{T_2}\overrightarrow{M_\perp} \tag{2.10}$$

with a solution of

$$\overrightarrow{M_\perp}(t) = \overrightarrow{M_\perp}(0)e^{-t/T_2} \tag{2.11}$$

In practice, in addition to the spin-spin interaction there is another source for the dephasing effect as introduced by the external field inhomogeneity. The decay time constant related to field inhomogeneity is often characterized as T_2' and the collective effect of T_2 and T_2' produces an overall relaxation time T_2^*

$$\frac{1}{T_2^*} = \frac{1}{T_2} + \frac{1}{T_2'} \tag{2.12}$$

The difference between T_2' and T_2 is that T_2 is resulted from the internal spin-spin interaction and is time-variant. The dephasing effect from such interaction is impossible to recover while the T_2' effect is static and its induced dephasing effect is recoverable using a specially designed sequence structure, which will be introduced later.

Combining the differential equations 2.7 and 2.9 yields the equation for magnetization in the presence of a magnetic field and with relaxation terms:

$$\frac{d\vec{M}}{dt} = \gamma\vec{M} \times \overrightarrow{B_{ext}} + \frac{1}{T_1}(M_0 - M_z)\hat{z} - \frac{1}{T_2}\overrightarrow{M_\perp} \tag{2.13}$$

This empirical vector equation is referred to as the Bloch equation, which is one of the most fundamental equations for MR signal detection.

2.1.3 Free Induction Decay, Spin Echo, and different contrast mechanism

Free induction decay (FID) is the simplest MRI experiment that detects a global signal from a sample. The basic FID sequence comprises a π/2 pulse which uniformly

rotates all protons into the transverse plane and a sampling period to collect signal induced by the time-varying magnetic field from the freely and collectively precessing spins. The signal from a repeated FID sequence, assuming that TR>>T_2^*, implying that the transverse magnetization has decayed completely by the end of any given repetition, can be found as

$$M_{\perp}(t_n) = M_0(1 - e^{-TR/T_1})e^{-t_n/T_2^*} \tag{2.14}$$

where TR is the time of repetition and t_n is the time of signal acquisition for each repetition (the application of π/2 pulse as time zero for each repetition).

FID presents the simplest sequence structure for MR signal detection but is not particularly useful in most practical applications. In the circumstance of field inhomogeneity, the time constant T_2' as described earlier can be sufficiently small that the $1/T_2'$ dominates $1/T_2$ and a severe signal loss may result before we acquire signal. The case is worse in applications where we want to manipulate the signal acquisition time to get different contrast images (e.g. spin-density weighted, T_1 weighted, or T_2 weighted) because of this fast decay. Fortunately, this dephasing effect caused by the external field inhomogeneity can be reversed by a well-known rf pulse sequence called "spin-echo". The basis of spin-echo is the application of two rf pulses: a π /2 pulse (applied at time t0), which tips all spins into the transverse plane, followed by another π pulse (applied after time τ) which reverses the phase accumulation direction induced by the time-independent field inhomogeneity. Hence after another time period of τ, the phase accumulated during the two time period before and after the π pulse will cancel each other and forms an "echo" at time 2τ. Therefore, the signal acquired at this time - TE (time to echo) will

only have T_2 effect with the T_2' decay recovered and the signal expression for repeated spin echo sequence is given by

$$M_{\perp}(TE + nTR) = M_0(1 - e^{-TR/T_1})e^{-TE/T_2} \quad (2.15)$$

Using the spin echo signal (2.15) as an example, we can see that the acquired MR signal is a function of three variables: M_0, TR, and T; it is based on the manipulation of these parameters that leads to numerous contrast mechanisms, of which the three most important are spin density, T_1 and T_2. Specifically, in order to get contrast primarily based on M0, the T_1 and T_2 dependence of the spin echo tissue signals must be minimized. In this case, the TR should be much longer than the longest T_1 and TE should be sufficiently shorter than the shortest T_2 to minimize their effects, respectively. For T_1 contrast, the TE should again be much shorter than the T_2 values to minimize its effect but the TR should be an intermediate value comparable to the T_1 values of interest. Finally, for T_2 weighting, TR should be much longer than T_1 to avoid contribution from T_1 and TE should be chosen to be comparable to T_2 to maximize contrast. In practice, since there is typically a positive relationship between spin density and T_1, T_2 value for certain tissue types, there is always an optimal value for TR/TE to maximize T_1/T_2contrast, respectively, which can be found analytically.

Besides spin density, T_1 and T_2, there are other contrast mechanisms including flow, magnetic susceptibility differences, magnetization transfer contrast, tissue saturation methods, contrast enhancing agents, and diffusion, among others. The next two sections will separately focus on (1) the contrast induced by diffusion for diffusion weighted imaging technique; and (2) the magnetic susceptibility effect for BOLD fMRI study to illustrate their signal formation principles.

2.2 Diffusion Weighted Imaging (DWI)

2.2.1 Intrinsic T2 Relaxation

As described above, the intrinsic T2 relaxation results from the depahsing effect induced by spin-spin interaction (38). The accumulated phase of a set of spins can be approximated by the central limit theorem. At each time point, assuming that the accumulated phase ϕ_i for the i^{th} spin is independent and random over all spins following the same Gaussian distribution and with the mean phase at each time point being zero, the probability density function of the accumulated phase is then

$$P(\phi) = \frac{e^{-\phi^2/(2\langle\phi^2\rangle)}}{\sqrt{2\pi\langle\phi_i^2\rangle}} \tag{2.16}$$

Hence the overall magnetization from the set of spins is:

$$M_+ = \frac{M_0}{\sqrt{2\pi\langle\phi_i^2\rangle}} \int_{-\infty}^{\infty} e^{i\phi} e^{-\phi^2/(2\langle\phi_i^2\rangle)} d\phi \tag{2.17}$$

which yields

$$M_+ = M_0 e^{-\langle\phi_i^2\rangle/2} \tag{2.18}$$

Under Brownian motion and assuming the imaging sample is homogeneous, each spin is expected to experience a phase change once every τ_2 seconds. If a given spin *i* experiences a local field $\vec{B}_i$, after N time steps over different local fields, its accumulated phase is

$$\phi_i(N, \tau_2) = -\sum_{j=1}^{N} \gamma B_{i,z,j} \tau_2 \tag{2.19}$$

where $B_{i,z,j}$ denotes the local filed around the *z*-axis at j^{th} position. Again the average value for the ensemble is zero, i.e., $\langle B_{i,z,j} \rangle = 0$ and $\langle \phi_i \rangle$=0 yielding

$$\langle \phi_i^2(N\tau_2) \rangle = \gamma^2 \tau_2^2 \sum_{j=1}^{N} \langle B_{i,z,j}^2 \rangle \tag{2.20}$$

Since there is no preferred direction in the microscopic field

$$\langle B_{i,x}^2 \rangle = \langle B_{i,y}^2 \rangle = \langle B_{i,z}^2 \rangle = \frac{1}{3} \langle B^2 \rangle \tag{2.21}$$

in terms of a generic field magnitude *B*. Combining Eq.(2.20) and (2.21)

$$\langle \phi_i^2 \rangle = \frac{1}{3} \gamma^2 \tau_2^2 N \langle B^2 \rangle \tag{2.22}$$

let $t = N\tau_2$ and combine Eq(2.22) and (2.18) to give

$$M_+ = M_0 e^{-\gamma^2 \tau_2 \langle B^2 \rangle t/6} = M_0 e^{-t/T_2} \tag{2.23}$$

where $T_2 = \frac{6}{\gamma^2 \tau_2 \langle B^2 \rangle}$, which is the expected exponential decay for spin-spin relaxation. Note here T_2 is tissue specific in terms of the average fluctuation period, the gyro magnetic ratio and the average local field, which reflects the spin-spin relaxation induced by thermal dynamic interaction among spins. As mentioned in the last section, other sources can also contribute to the loss of signal such as inhomogeneities in the external static filed, in which case Eq(2.23) can be rewritten

$$M_+ = Me^{-t/T_2^*} \tag{2.24}$$

where $T_2^* < T_2$ reflecting the combined effects of spin-spin relaxation of external field inhomogeneities.

2.2.2 Diffusion Model under Diffusion Sensitive Gradient

The spin echo method can correct for spin dephasing induced by the field inhomogeneities experienced by different spins at different positions (static) as described above. However, the dephasing resulting from the change of position of a given spin in an inhomogeneous field through diffusion is more complicated and can be utilized to generate a diffusion-weighted signal as described below.

In the presence of a non-uniform field, spins undergo Brownian motion, leading to random changes in phase. By applying an extra gradient along a certain direction, the signal loss due to this Brownian motion can be derived. For simplicity, we here assume a random walk of spins in a single spatial dimension and the sensitizing gradient (G) is applied along the same direction. A spin at the position x moves to a new position $x+\varepsilon_i\mu$ every τ_d seconds, where μ is the step size and $\varepsilon_i = \pm 1$ randomly. Therefore, the spin experiences a new field $B(j\tau_d) = B(0) + G\mu\sum_{i=1}^{j}\varepsilon_i$ after j steps and the field change is $\Delta B(j\tau_d) = B(j\tau_d) - B(0)$. After N steps, the total phase change for the spin is then

$$\phi_i = -\sum_{j=1}^{N}\gamma\tau_d\Delta B(j\tau_d) = -G\mu\gamma\tau_d\sum_{j=1}^{N}\sum_{i=1}^{j}\varepsilon_i \tag{2.25}$$

After some approximation, $\langle\phi_i^2\rangle$ can be approximated as

$$\langle\phi_i^2\rangle = \frac{1}{3}G^2u^2\gamma^2N^3\tau_d^2 = \frac{1}{3}G^2\mu^2\gamma^2t^3/\tau_d \tag{2.26}$$

where $t = N\tau_d$. Combining Eq(2.26) and (2.18)

$$M_+(diffusion) = M_0e^{-\gamma^2G^2\mu^2t^3/(6\tau_d)} \tag{2.27}$$

The overall signal decay from both local (T_2) and diffusion effects can be obtained by combining (2.27) and (2.23)

$$M_+ = M_0 e^{-t/T_2} e^{-\gamma^2 G^2 D t^3/3} \quad (2.28)$$

where $D = \mu^2/(2\tau_d)$ is the standard diffusion constant, which is usually termed as "diffusivity" in practice. It is common to rewrite (2.28) in the form

$$M_+ = M_0 e^{-t/T_2} e^{-bD} \quad (2.29)$$

where $b = \gamma^2 G^2 t^3/3$ is the so-called b-value for the diffusion weighted imaging experiment. Notice here there is an extra exponential decay term induced by the underlying diffusion sensitive gradient parameter *b*, which leads to the fundamental principle of DWI.

2.2.3 Practical implementation and applications

Notice in the above derivation, only one diffusion sensitive gradient direction is applied. In practice, multiple directions are usually applied and different techniques can be used to reconstruct the underlying diffusion properties within an imaging voxel, including diffusion tensor imaging (DTI) (36) and various high angular resolution diffusion imaging (HARDI) (39) techniques. The possible improvement on these techniques is one of the focuses of this dissertation and will be discussed in Chapter 9.

Various applications are made possible by diffusion weighted imaging in determining the diffusion properties of both white matter (WM) and gray matter (GM) under normal or pathological brain conditions. DTI has been extensively applied in studying brain development and effects of aging by either investigating the local diffusion properties (40, 41) or studying the structure of anatomical/functional networks using tractography or connectivity mapping (42). DTI has also found wide applications in delineating various brain pathologies such as cerebro-vascular diseases, multiple sclerosis, Alzheimer's and Parkinson's disease, schizophrenia and brain tumors (43, 44). However,

a well known limitation of DTI is its inability to depict fiber crossings, which accounts for one-third to two-thirds of imaging voxels in the human brain's white matter. Subsequently, the HARDI techniques (39) such as Diffusion Spectrum Imaging (DSI) (45) or Q-Ball Imaging (QBI) (46) have been proposed and proven to be promising in recovering fiber crossing information. With these techniques, whole brain tractograghy is made possible, allowing the study of structural/anatomical connection information and providing an integrated understanding of brain functioning mechanism. Development of various diffusion properties in WM is one of the focuses of this dissertation and will be discussed in the Chapter 5.

2.3 Functional Magnetic Resonance Imaging (fMRI)

FMRI is based on the coupling of MR signal changes with the change of local brain activity. The underlying mechanism is that the local susceptibility property is modulated by the oxygenation level of the blood, which is further related to neuronal activation.

2.3.1 Dependence of Blood Susceptibility on Oxygenation Level

Blood can be approximated as a two-compartment system consisting of both red blood cells and plasma. With the magnetic property of plasma much like water, the magnetic properties of the red blood cell depends on the relative concentration of oxyhemoglobin and deoxyhemoglobin. Oxyhemoglobin is diamagnetic with no unpaired electrons and negative susceptibility while deoxyhemoglobin is paramagnetic with unpaired electrons and positive susceptibility. Since deoxyhemoglobin is more paramagnetic than oxyhemoglobin, its presence will increase local inhomogeneities and decrease T_2^* in Eq.(2.24), leading to faster dephasing and signal drop.

Assuming the oxygenation of the blood is dominated by the formation of oxyhemoglobin, a model for the susceptibility of the whole blood system is given as

$$\chi_{blood} = Hct\,(Y\chi_{oxy} + (1-Y)\chi_{deoxy}) + (1-Hct)\chi_{plasma} \tag{2.30}$$

where χ represents susceptibility, *Hct* is the fraction of the volume of packed red blood cells to the volume of the whole blood, Y is the oxygenation level. A change of ΔY in the oxygenation level alters the susceptibility according to

$$\Delta\chi_{blood} = -\Delta Y(\chi_{deoxy} - \chi_{oxy})Hct \tag{2.31}$$

When neglecting any oxygenation in blood plasma.

2.3.2 Dependence of Blood Oxygenation Level on Blood Flow

Considering both the blood flow and the cerebral "metabolic rate" or oxygen utilization, the change of the number of deoxyhemoglobin is given by (38)

$$\Delta N_{deoxy} = \beta N_{deoxy}/(1+\alpha) - N_{deoxy} \tag{2.32}$$

where α is the relative blood flow change and β is defined as oxygen utilization. In terms of oxygenation level change

$$\Delta Y = -\Delta N_{deoxy}/N_0 = \frac{1+\alpha-\beta}{1+\alpha}\frac{N_{deoxy}}{N_0} = \frac{1+\alpha-\beta}{1+\alpha}(1-Y) \tag{2.33}$$

2.3.3 Practical implementation and applications

In a simple experiment where a volunteer moves his/her thumb, the blood flow will increase in the primary motor cortex while the oxygen utilization does not change much ($\beta \approx 1$) and hence ΔY will increase, which decreases the local blood susceptibility and increase MR signal as described in last section. Of course this is only a simple example while in practice more complex imaging paradigms have been utilized to study the activation patterns of different brain functions such as visual, attention, auditory, and

many others (13, 18, 47). These task-related fMRI studies have proved to be very successful in delineating various brain functions. Alternatively, Biswal et al. (20) proposed a different approach in investigating brain function during a "resting state", which is termed as functional connectivity MRI (fcMRI). Since then, numerous studies have been conducted and different resting state networks (RSN) have been identified and studied (22, 24, 48). One exciting possibility of the "resting brain" approach is the ability to investigate brain function of the pediatric subjects which would be otherwise impossible given the requirement of a task.

To depict brain's functional development during early brain development is the primary focus of this dissertation and will be extensively discussed in Chapter 6-8. But before that, the neurophysiological underpinnings of BOLD signal as well as functional connectivity will be discussed in the next chapter to provide a link between these techniques and the underlying neuronal activity.

Chapter 3

Neurophysiological underpinnings of BOLD Contrast and Functional Connectivity Study

Functional magnetic resonance imaging (fMRI) using BOLD contrast has been one of the back-bone techniques in neuroscience for decades (14). However, till now, how exactly neuronal activity triggers the overcompensation of blood supply which thus leads to BOLD signal change is still partially unknown. Neuronal activity changes can readily occur at millisecond levels within a spatial scale of hundreds of transiently "synchronized" neurons, but the "sluggish" BOLD changes usually come after one or two seconds and with a massive over-perfusion covering a much broader spatial territory than the underlying neuronal activity. Why and how brain does this is still an open question. But thanks to the active research in this field, there has already been some clues of what's happening during this coupling period. Moreover, there are also empirical evidence on the coupling between neuronal activity and BOLD signal changes(49-51). The first section of this chapter will review such mechanisms and evidences to pave the ground for the following discussion using this technique.

Despite the fundamental role of an individual neuron/neuron population, it is perhaps the "wiring" between them that makes human brain uniquely powerful. A single neuron can have up to a thousand afferent/efferent connections to other neurons and there

are approximately 100 trillion of neuronal connections within the entire brain. Thus, it is not surprising that the majority of the brain's energy is spent to maintain this massive communication, which facilitates efficient cooperation of different units and forms various "functional networks" for different and complex cognitive functions. As a result, after a long period of interest in localizing specific cognitive functions to specific brain regions using fMRI, the new area of "functional connectivity" using low-frequency BOLD fluctuations is gaining more attention and is also the central technique used in this dissertation. The second section of this chapter will describe the neurophysiological basis for functional network and BOLD-based functional connectivity. Moreover, its applications and limitations will also be discussed.

3.1 Neuronal basis of BOLD contrast

3.1.1 Potential Mechanisms of coupling between neuronal activity, blood flow, and energy metabolism

As described in the previous chapter, BOLD contrast is based on the overcompensation of oxygen to the local brain regions where an increased neuronal activity has occurred. This overcompensation is through an increase of local blood flow, which brings two of the most important "fuels" to local brain tissue: glucose and oxygen. PET and fMRI studies have well documented the parallel increase of blood flow and glucose utilization in response to local increase of neuronal activity but minimal increase in oxygen consumption (52). It is this mismatch that increases local oxygen concentration and decreases the susceptibility effect which in turn boosts BOLD signal. Hence two events act in concert leading to the observed BOLD signal change: the increased blood flow and unparalleled oxygen consumption, revealing an intricate

relationship between neuronal activity, cerebral blood flow and energy metabolism. In this section, potential mechanisms underlying the coupling between these three parties will be described to help understand the neuronal basis of BOLD contrast.

Although it is a general principle in brain physiology that neuronal activity is tightly coupled with blood flow and energy metabolism, the actual cellular and molecular mechanisms underlying this coupling are nevertheless far from being firmly established. Intensive research has been conducted searching for potential candidates responsible for neurovascular coupling. Thus far, those that have been identified can be classified into two broad categories, including (a) molecules/ions that accumulate in the extracellular space after neuronal activity and (b) neurotransmitters released by activated neuronal pathways. However, current understanding is that the temporal and spatial resolution of actions of potential candidates in category (a) such as H^+ and K^+, released by active neurons, can hardly explain the observed rather tight neurovascular coupling while the second category-vasoactive neurotransmitters appear considerably better fitted for this coupling (53, 54).

Glutamate, the predominant excitatory neurotransmitter in the brain, is believed to play an essential role in neurovascular coupling. However, the role of glutamate on vasomotor response is generally reported to be indirect; it is mediated by nitric oxide (NO) that is released by the activation of postsynaptic glutamatergic neuron receptors (55). The formation of NO in the presence of glutamate is a well established fact (56-58) and it is through this potent vasodilator that glutamate stimulates local increase of blood flow. In addition to neurons, astrocytes have also been reported to be involved in glutamate-induced increases in CBF. The suggested working hypothesis is that astrocytes release

epoxyeicosatrienoic acids in response to glutamate, which may activate smooth muscle K^+ channels, increase outward K^+ current and hyperpolarize the plasma membrane, which in turn inhibits voltage-gated Ca^{2+} channels and leads to arteriolar dilation (59).

As possible mechanisms for neurovascular coupling have been reviewed, the next question is the relationship between the neuronal activity and glucose utilization. A long-held assumption in neurometabolic coupling has been that neuronal signals released by synaptic activity directly act on brain capillaries to increase local energy supply. However, an alternative is recently emerging - mediation through astrocytes. Astrocytes possess extensive end-feet surrounding intraparenchymal capillaries while at the same time extend processes that ensheath synaptic contracts. These unique features imply that astrocytes are ideally positioned to sense changes in synaptic activity and to couple them with the import of glucose for metabolism, which promotes the hypothesis of a functional "triad", consisting of the neuropils, astrocytes and capillaries that are responsible for the local regulation of brain energy metabolism concomitant with neuronal activity. Actually, a detailed working model has been established for the cellular processes occurring within this functional "triad" (60-62). In short, at glutamatergic synapses, pre-synaptically released glutamate depolarizes postsynaptic neurons by acting at specific receptor subtypes. However, the released glutamate is rapidly uptaken by surrounding astrocytes. Since glutamate is co-transported with Na^+, this leads to an increase in intra-astrocytic concentration of Na^+, which in turn leads to the activation of Na^+/K^+-ATPase. The activation of Na^+/K^+-ATPase stimulates glycolysis and produces lactate which can be taken up by neurons and serves as energy substrate for them. Thus this chain provides a

potential mechanism for coupling neuronal activity with glucose utilization, within which the astrocyte-mediated, glutamate-triggered glycolysis is the central process (60-62).

This transient lactate production through glutamate-mediated glycolysis in response to local neuronal activity increases is consistent with experimental observations both in laboratory animals and humans. MRS in human reveals a transient lactate peak during activation of the visual system (63) and PET studies by Fox et al (52) observed that oxygen consumption does not increase in parallel with blood flow and glucose utilization in activated brain areas, raising the possibility of activity dependent glycolysis (52).

Overall, glutamate is deemed to be a central candidate for both neurovascular and neruometabolic coupling. Although the general picture of neurovascular coupling is still obscure, experimental evidence supports the involvement of glutamate, among others, in this process. For the glutamate-driven meurometabolic coupling process, there is clear evidence on the important role of astrocytic glycolysis as an essential step. Moreover, glutmate-mediated signaling pathways may regulate CBF and glucose utilization in parallel rather than in series. Through glutamate receptor mediated stimulation of NO formation in neurons/astrocytes, it leads to local vasodilation and through glutamate transporter-mediated glycolysis, it stimulates glucose uptake into astrocytes from local blood flow.

3.1.2 Experimental evidence of the neurophysiological basis of BOLD signal

BOLD response only measures hemodynamic changes which far lag behind the neuronal activity, leaving many unanswered questions concerning the relationship between them. Many studies tried to combine fMRI with EEG or optical imaging in an

effort to reveal their relationship, but these two techniques have their own limitations that prevent precise characterization. Optical imaging essentially also measures hemodynamic responses and EEG suffers from poor spatial resolution and imprecise localization of the underlying electromagnetic field.

Micro-electrode recording can precisely quantify neuronal activity at both single neuron, multiple neurons or a neuron population level and has been used in animal studies for decades(2, 3). Hence the combination of fMRI with microelectrodes will be an ideal combination to reveal the relationship between BOLD signal and neuronal activity. Specifically, single unit (SUA) and multiple unit activity (MUA) reflect primarily the spiking output of a specific or a small set of neurons surrounding the electrode tip. On the other hand, local field potential (LFP) represents mostly a weighted average of synchronized dendro-somatic components of the input signals into a neural population within a few millimeters of the electrode tip. As a result, the combination of fMRI with microelectrode recording can not only answer the question of whether there is a neuronal substrate for BOLD signal but also potentially differentiate the source between the spiking activity (SUA/MUA) and integrated dendritic activity (LFP).

Such a seminal study was performed in 2001 by Logothetis and colleagues (49) on a monkey model using a specially designed electrophysiological measurement technique coupled with fMRI. Their findings show that a localized increase in BOLD contrast directly and monotonically reflects an increase in the underlying neural activity, providing strong evidence on the neuronal basis of BOLD contrast. Moreover, in order to better understand the neural mechanisms underlying the BOLD responses, they separately examined spiking activity (MUA) and local field potential (LFP). They found

that the increase in LFPs during stimulation was significantly stronger than that of MUA. Moreover, while MUA often demonstrated adaptation by returning to baseline levels 1 or 2 seconds after stimulus presentation, LFP activity was always maintained throughout the whole stimulus period and was better correlated with BOLD signal. In addition, convolving neuronal activity with the neural-vascular impulse response function to predict the BOLD signal, the average LFP response was always found to give better estimates of the true BOLD signal than MUA. Overall, they conclude that BOLD response seems to be better correlated with the LFPs, suggesting that BOLD activation likely reflects the integrated input and local processing rather that the spiking output activity, which for the first time provides empirical evidence on the neural basis of BOLD signal. Following this, a series of studies have been performed and consistent findings have been reported (50, 51, 64, 65).

There are also studies to directly relate the neuronal firing pattern, local field potentials with BOLD signal in human subjects rather than in anesthetized animal models (66, 67). Mukamel et al (66) performed such a study by recording 53 single neurons in the Heschl's gyrus (auditory gyrus) of two epilepsy patients who were monitored with intracranial depth electrodes for potential surgical treatment. Signals were recorded when the patients were watching two repetitions of a 9-min popular movie segments. FMRI study was performed on another 11 normal subjects when they were watching the same movie segment. Strikingly, using the "spike predictor"- convolution of averaged spiking activity with a standard hemodynamic response function, they were able to derive a group "activation" map from the 11 normal subjects, demonstrating robust activation around the Heschl's gyrus in close proximity of the electrode's location. Moreover, by sampling the

BOLD signal from ROIs within the Heschl's gyrus of each subject and averaging across subjects, they showed that this average signal was highly correlated with the spike predictor (0.75, $p<10^{-47}$ for patient 1 and 0.56, $p<10^{-28}$ for patient 2). This striking inter-subject correlation between neuronal spiking activity and BOLD signal proves that BOLD contrast can be "trusted as a faithful measure of the average firing rate of the underlying population".

Overall, although the exact mechanism underlying the coupling between neuronal activity and hemodynamic response measured by BOLD signal remains partially elusive, empirical data, however, strongly support the neuronal basis for the observed fMRI signal hence pave the ground for its application in human functional studies.

3.2 Functional connectivity study of brain's network organization

It is the belief that large scale networks of distributed and interconnected neuronal populations underlie human cognition that drives the study of "functional connectivity". The belief comes from the reconciliation of two opposite views, namely "localizationism" claiming that complex cognitive functions reside in specific brain regions and "globalism" supporting the notion that they are global functions of the brain. With increasing evidence, modern neuroscientists view cognitive function as intermediate between the two opposing views: it is a result of an integrated process between distributed brain regions where each deals with individual elementary functions. However, numerous issues such as the principles guiding this organization, the dynamics of this organization at different time scales and its pathological implications, are far from clear. This is particularly true for human studies primarily because of the lack of non-invasive and spatially resolved techniques targeting this problem. However, the advent of functional connectivity MRI

(fcMRI) brought a unique opportunity to directly study this network organization non-invasively and gained wide-spread interest in the past decade. In this section: (1) the basic presumptions underlying functional connectivity as well as the network organization of the central nervous system will be reviewed and (2) the applications of rs-fcMRI together with its limitations will be discussed.

3.2.1. The neurophysiological Basis of functional network and connectivity

The neuron is the basic constructing unit of the central nervous system. However, it does not function as an isolated unit and is not generally considered to be the major operational unit for cognitive function. Instead, dozens to hundreds of neurons, densely inter-connected, form anatomically distinct minicolumns oriented perpendicular to the surface of the cortex. Tens of such minicolumns are aggregated into a macrocolumn, which receives synaptic inputs and sends out axonal projections as a whole. Such a minicolumn is perceived to be a candidate unit for elementary cognitive operations (68, 69). Further, the dense short-range interconnections between a set of macrocolumns in a local area form a neuron assembly and give rise to a local cortical area network. In the context of functional connectivity, such a local area network, composed of neighboring macrocolumns sharing common input and output pathways and showing a specialized rudimentary function will be considered as the basic neruophysiological component (70).

The communications of neurons within such an assembly have been extensively studied and the general concensus is that it is achieved through the synchronous activity of the participating neurons (71-75), i.e., synchronized excitatory/inhibitory postsynaptic potentials, EPSP/IPSP). Although many other aspects of neuronal interactions exist, the temporal synchronization is considered to be one of the most important factors (76). This

temporal synchronization or correlated activity within a neural assembly is sensitive to shifts of functional states. Therefore, during a functional "activation", such synchronized activity leads to an increase in the field potential while a disruption of such synchronization may lead to a decrease in field potential, as readily measured by EEG/MEG (77).

The observation of connectivity, either neuroanatomical or functional, between remote neural assemblies across the whole neocortex promotes the idea of the "network" organization (78). The anatomical foundation of this connectivity is well documented through both traditional histological tracing studies and contemporary DTI studies as described in the earlier chapters. Different cortical/subcortical areas are highly inter-connected by well-myelineated, high velocity, white matter fiber tracts. Moreover, there is also evidence that cortical areas with similar functional attributes are preferentially interconnected (68, 69). The anatomical connections between remote neural assemblies provide structural basis for the communication between them which in turn make possible the necessary functional integration to form distributed networks. However, there is still a big gap between them. Evidence of functional coordination between remote neural assemblies can be derived from studies directly measuring neuronal activities such as local field potential (LFP). As described in the last section, LFP measures the synchronous post-synaptic activity of a group of neurons from a localized volume within several millimeters vicinity of the implanted microelectrodes. Different from single-unite or multiple unite spiking activity, LFP is capable of revealing the synchronous dendritic activity while obscuring the specific contributions from specific neurons. This non-specificity is nevertheless advantageous in cognitive function studies since the

transmission of pulse activity from one area to another, especially when they are a distance away, is effective only at the level of neural assemblies not that of single neurons (68, 69). Thus, directly related to the integrated inputs at the post-synaptic dendritic trees of the corresponding neural assembly and also to the intergral of the pulse outputs, LFP reflects the actions exerted by cortical areas on each other through axonal pathways. Frequently, LFP is analyzed in the frequency domain by coherence, which is a normalized quantity between zero and one, indicating perfect relative phase synchronization and no synchronization, respectively. As a result, large coherence values represent a stronger correlated LFP activity (with certain phase lag) hence stronger correlated neuronal activity between different sites of the brain. In a seminal study by Bressler et al (79), they showed a widely distributed increased broad band (12.5Hz~87.5Hz) coherence from sensory, motor and high-order cortical sites of macaque monkeys when performing a visual discrimination task, without involving other intervening sites during an extended time after stimulus presentation, strongly supporting the coordination between multiple distributed brain regions in motor behavior. Subsequently, a follow-up study showed that during the time of elevated coherence, bidirectional (both feedforward and feedback) causal influences are exerted between one site in the striate cortex and the other in inferior temporal cortex during the same task performance (80). Moreover, a series of other studies have reported synchronizations of LFP oscillations in the gamma frequency range (30-80 Hz). Several groups (81, 82) reported an increased gamma-correlation between different visual areas during visual stimuli in cat studies and others have reported different patterns of transient synchronization within striate cortex, superior temporal cortex and motor-sensory cortex

in monkey studies (83-86). Overall, these studies together provide strong evidence for the coordination of distributed brain regions for specific brain network to facilitate the performance of certain cognitive tasks. This coordination, or "binding", is essential for the brain to integrate otherwise "fragmentary" events at multiple locations to achieve a unified perception and behavioral goal (79).

3.2.2 Connectivity at different spatial/time scales and corresponding detection techniques

Despite the general consensus that normal brain function relies on the coordination between distributed but interconnected neuronal assemblies, the brain's network structure at different spatial and time scales are far from clear (68).

Spatially, the brain's connectivity ranges from between remote regions through large white matter fiber bundles to within cortical layer neuronal communication through axon-dendrite wiring. In time, on the phylogenetic time scale of generations, the basic pattern of anatomical connectivity of the brain is determined by the evolution of each unique species, which forms the basis for any neurocognitive operations. On the ontogenenic time scale of years, the modification of brain's structural/functional connectivity is modulated by developmental and experience based factors to achieve a functional setting unique to each individual for neuro-cognitive functions. On a time scale of seconds to minutes and hours, brain's connectivity may undergo short-term modulations responsible for the transmission of brain states to accommodate various cognitive functions including emotion, attention, and memory. Finally, transient coordination between neuronal populations works on a sub-second time scale to initiate or maintain neurocognitive operations (68-70)

From fiber bundle modulation lasting for years or even generations to transient neuronal coordination changes occurring within a second, there is an intricate relationship between the spatial and time scale of brain's connectivity. Our awareness of this intricate relationship relies on the development of different measuring and analysis methods based on a variety of underlying physiological parameters. For example, based on the differential diffusion properties within brain's white matter, diffusion weighted MRI (DWI) is able to non-invasively reveal brain's white matter property with a great spatial precision (36, 37). Moreover, fiber tractography made available by diffusion tensor imaging (DTI) and high-angular resolution diffusion-imaging (HARDI) provides the unique opportunity to look at brain's anatomical connectivity non-invasively which has gained wide spread interest during recent years (42). On the other extreme, single unite recording and multiple unite recording, by directly measuring the spiking activity of one to tens of specific neurons, provide us millisecond time resolution (>400Hz) of neuronal activity recording, pushing forward our understanding of brain communication scheme at a single neuron level. At a slightly slower time scale (<300Hz) and a broader spatial resolution, LFP recording, as mentioned earlier, measures the synchronous postsynaptic activity of a neuronal population within several millimeters vicinity, providing us probably the most relevant functional activity information of neuronal assembly.

Despite their high spatial and temporal resolution, the applications of LFP and single/multiple unite recording are largely prohibited in human studies because of their invasive nature. EEG provides a non-invasive alternative, which also measures the synchronous postsynaptic electrical activity at a similar time resolution with LFP. As a result, EEG has been widely applied in human functional connectivity studies as well as

clinical use especially in the case of epileptic seizures (4, 5, 9, 11, 83, 87). However, the non-invasive nature of EEG comes with a cost. Signal recorded at a single scalp electrode reflects not only the electrical neural activity directly beneath it, but also the neural activity at more distant locations propagated through electromagnetic fields as mediated by the intervening tissue and other matter, known as volume conduction. This, together with the spatial smoothing effect of the lead field linking the intracranial electrical activity to scalp electric fields, severally degrades the spatial resolution of EEG signal to over centimeters, resulting in poor functional connectivity localization.

On the other hand, BOLD fMRI is a powerful neuroimaging tool to localize various brain functions with highly resolved spatial resolution (~millimeter or sub-millimeter with the high field scanner (>3T)). Being totally non-invasive and with high spatial resolution, fMRI has been the primary tool for decades enabling researchers to assign brain regions to specific cognitive function using carefully designed task paradigms, which has fundamentally improved our understanding of the local brain functions and will continue to do so in the future.

In the mid-1990's, it was the observation that the correlation pattern of spontaneous low-frequency BOLD signals within the motor-sensory system during a resting state highly resembles the activation pattern during motor tasks that flourished "functional connectivity" studies to investigate the functional synchronization/ coordination of distributed but interacted brain regions (20). After its inception, this new derivative of fMRI incurs great interests among neuroscientists in uncovering the global interaction pattern among distributed brain regions, which is potentially responsible for different cognitive tasks such as motor control, memory, attention, etc (20, 23, 30, 32, 88).

Among all functional networks, the "default-mode" network coined by Raichle et al (26), which composes a set of regions that consistently increase activity during an idling/resting state when compared with a goal-directed task state, incurs particular interest to look into its functional relevance and more generally the "intrinsic" whole brain organization during the resting state (25, 27).

Overall, defined as the statistical correlations between the MR signal fluctuations in different brain areas, functional connectivity studies based on BOLD fMRI (fcMRI) – the central technique used in this dissertation – represents a new tool in neuroimaging analysis. The typical temporal resolution of fcMRI (around seconds) is enough for functional connectivity at two of the four time scales mentioned earlier: (1) the ontogenenic level, which involves functional connectivity modulation by developmental/aging factors and (2) the seconds to minutes/hours level which explores short-term modulations of functional connectivity responsible for smooth transition of different brain states incurred by emotion, attention, working memory, etc. Hence, despite the losts of sub-second temporal resolution to reveal transient connectivity patterns, fcMRI is still capable of answering important questions regarding both the "intrinsic" and "dynamic" properties of brain organization at different time scales.

Given the discrepany in time scale between fcMRI studies (usually <0.1Hz) and neuronal activity (~10^2 Hz), one of the prerequisites for fcMRI to be interpretable is the association between the observed correlation and the underlying neuronal activity synchronization. Although we have demonstrated the association between neuronal activity and BOLD signal in the previous Chapter, the association at the "connectivity" level has not been directly illustrated, which will be discussed in the next section. In

addition, the various applications of fcMRI in detecting functional connectivity modulation at different time scales as well as the limitations will be reviewed in the next section.

3.2.3 The essence and limitations of fcMRI

3.2.3.1 The neuronal events underlying the slow (<0.1Hz) spontaneous BOLD fluctuations

Till now, we have reviewed evidence on: (1) the tight coupling between neuronal firing, field potentials (LFP) and BOLD signal (Section 3.1); and (2) the synchronization of integrated neuronal activity between remote but functionally related neuronal assemblies as revealed by LFP coherence at different frequency bands (around 12Hz~80Hz) (Section 3.2.1). The combination of these two channels of information thus seems to provide a firm rationale for the use of BOLD signal as a means to investigate brain's functional connectivity. However, the observed coherent neuronal activity is at a much shorter time scale (>10Hz) when compared with the low-frequency synchronization of BOLD fluctuations (<0.1Hz). Without knowing what aspect of neuronal activity is behind this low-frequency BOLD synchronization, the interpretations of fcMRI studies might still suffer.

One seminal study by Nir et al (89) might provide some insights, however. They combined single-unit, local field potentials (LFPs) and intracranial electrocorticograhy (ECoG) recordings in individuals undergoing clinical monitoring during both wakeful rest and sleeping and reported four major findings. Firstly, by filtering the single unit firing rate modulations into three frequency bands: slow (<0.1Hz), medium (0.1-1Hz) and fast (>1Hz), they found that the single unit activity manifested the highest and most

significant interhemishperic correlations at low temporal frequencies (<0.1Hz, r=0.32, p<0.0005); Secondly, through the identical procedure, they found the same bias of interhemispheric correlations in LFP power fluctuations (gamma-band, 40-100Hz) toward low frequency range of <0.1Hz (r=0.43, P<0.0005). Moreover, the correlations between spiking activity and gamma-band LFP power were significantly higher at low-frequency range (<0.1 Hz). Thirdly, using the EcoG gamma-power measurement, they demonstrated high spatial selectivity of spontaneous fluctuations where they showed that interhemishperic correlations were robust within auditory cortices (r=0.61) and within visual cortices (r=0.34), respectively, but minimal across the two functional systems (r=0.02). Finally, they made a connection between their findings using direct neuronal activity recording (single unit and LFP) and BOLD fluctuations by analyzing fMRI dynamics in the same manner and showed similarity.

This study rigorously demonstrated that the synchronization of firing rate and LFP power dynamics is dominated by low frequency (<0.1Hz) and this temporal synchronization is highly spatially selective to be within functionally similar systems. These findings match well with the characteristics of spontaneous BOLD fluctuation synchronizations. Takn together with the previous observations of the tight LFP-BOLD coupling, they provide decent evidence to the hypothesis that spontaneous modulations in firing rate and gamma LFP power are the neuronal correlates of spontaneous fMRI fluctuations.

3.2.3.2 "Intrinsic" or "dynamic"?-rfcMRI at a different time scales

As described above, the spontaneous modulation in the firing rate and gamma LFP power likely reflect the neuronal correlates of spontaneous fMRI fluctuations, but

the exact role of the correlated spontaneous fluctuations is far from clear. One view, as mentioned in Nir et al (89), is that they serve some role in maintenance and renormalization of synaptic contracts driven through neuroanatomical connectivity. Although not fully validated, the hypothesis that BOLD fluctuations are "intrinsic" and constrained by anatomic connectivity receives several lines of evidence.

The first line of evidence comes from animal studies which usually involve tracer injections to define anatomical pathways. For example, patterns of correlated spontaneous fluctuations in the oculomotor system of the macaque monkey are highly consistent with the anatomical network revealed by retrograde tracer injections (90-92). Margulies et al (93) also showed correspondence between functional connectivity and structural connectivity for four distinct pathways revealed by tracer injection. Secondly, quantitative structural imaging studies such as those using DTI have also reported that a significant portion of variance in spontaneous connectivity can be explained by structural connectivity measures such as FA, number of fibers and physical fiber distance (42, 94). Finally, some studies have directly performed fiber tracking using the functionally connected ROIs as foci and qualitatively demonstrated the anatomical connections underlying the functional connectivity (95).

In contrast, sets of evidence on the "dynamic" component of functional connectivity have also been reported, which support the notion that it reflects spontaneous cognitive process and will be modulated under task performance. A greater activity in the default-network regions is associated with more reported task-independent thoughts and delayed response during task performance (96). Kelly et al (97) also reported that task performance is positively related to the "anti-correlation" between the

task-negative default network and the task-positive dorsal attention network, underscoring the cognitive aspect of functional connectivity. Moreover, several recent studies also reported modulation of functional connectivity by recent task performance experience. More interestingly, this modulation seems to predict the future performance of the specific task previously performed, implying one potential important functional role of functional connectivity in memory consolidation and learning (98, 99).

Combining these evidences, it is not hard to conclude that functional connectivity actually is capable of reflecting brain's connectivity at different time scales: the ontogenetic level modulated by developmental/aging factors and the more dynamic scale influenced by cognitive states of the brain. Actually, there are already numerous studies, including ours, which have successfully applied fcMRI to show corresponding developmental/aging modulations of brain's functional connectivity either for a specific brain network or whole brain organization (100-102). One thing particularly interesting along this direction is the ability to look at the interplay of functional and structural connectivity during early brain development since it is likely that they will influence each other during the experience-based tuning process. This area will be one of the future directions that we will look into. On the other hand, the short-time scale modulation of functional connectivity is also extremely important to find out the cognitive relevance of functional connectivity and its possible role in the most fundamental aspects of brain function such as learning and memory, which occurs right at the time scale that fcMRI is able to handle. Actually, fcMRI's ability to reveal modulation of functional connectivity at these two different time scales will be explored in this dissertation in the following Chapters as well as in our future research.

3.2.3.3 Artifacts and limitations of fcMRI

No technique comes with perfection. The rfcMRI is also destined to be contaminated by different sources of noise related with both image acquisition process within the scanner and the physiological fluctuations inherent to human subjects. Confounding factors from the scanner include system noise, subject motion, and field inhomogeneity among others, which to some extent can be alleviated by spatial smoothing, averaging within ROIs, image registration and careful shimming of the magnetic field of the scanner, etc.

Another more complex noise source comes from the rhythmic physiological process inherent to human subjects such as respiratory and cardiac motion. These sources of noise are of particular importance given their rhythmic nature which will inevitably generate artificial "correlation" between BOLD signals through similar mechanism as the BOLD contrast (rhythmic change of deoxygen-hemoglobin concentration). The fact that these noise sources operate at a much higher frequency (around 0.3 Hz for respiratory cycle and 1 Hz for cardiac cycle) than that we are interested in for BOLD fluctuations (<0.1Hz) does not prove particularly useful. This is due to the fact that the TR of fcMRI studies typically lasts for several seconds, meaning that the higher frequency noise signal will inevitably alias into the measured BOLD signal and is impossible to be eliminated by simply low-pass filtering.

One approach for solving the problem is independent component analysis (ICA), which has the ability to separate different sources of information. Indeed, spatial ICA has been demonstrated to be useful in separating the whole brain signals into functionally relevant components mainly residing in the gray matter regions and noise dominated

components, which typically cover cerebral spinal fluid (CSF) space, white matter regions, large vessels or brain boundary areas (103). Although being able to spatially separate different sources, the signals within the "functionally-relevant" regions are not free of noise since their effect can be equally expressed, if not more, through the much smaller arterioles within the gray matter regions.

So besides low-pass filtering of the BOLD signal to remove the high frequency noise (>0.1 Hz), another common procedure typically applied in fcMRI studies is the regression technique to remove possible sources of noise. Usually, signals from the ventricle space (CSF), white matter regions and the whole brain average signal will be treated as noise regressors and the signal in each voxel is orthogonalized to these sources through regression. These procedures have been proved to be effective in minimizing the influences of respiration and cardiac cycle as well as increasing the specificity of brain correlations. However, there are still controversies regarding the removal of global signal and for review on this issue, please refer to these review articles (104, 105). In our study, a combined strategy including low-pass filtering, ICA, and noise source regression have been applied to minimize the physiological artifact, which will be discussed in detail in Chapter 6 to 8.

Chapter 4

Early Brain Development: Structures and Functions

As studies focusing on matured brain functioning are abundant, studies targeting at its development during very early periods, esepcially the first few years, are much fewer largely due to the lack of non-invasive brain imaging techniques. However, with the development of DTI and fcMRI, as described in previous chapters, there is currently great opportunity to look into this issue with these powerful and non-invasive tools. The central focus of this dissertation is the delineation of the functional development and structural underpinnings during this critical period through the application of these two techniques. Befroe we describe the specific findings made in our study, an overall view of early brain structural and funcitonal devepment will help build a general picture. In this chapter, such a general review is provided to pave the way for the following specific discussions.

The brain undergoes rapid, diverse and integrated development both structurally and functionally starting as early as the fetus. Knickmeyer et al (106) revealed that, globally, the total brain volume doubles in the first year, followed by a 15% increase in the following year. However, this dramatic growth is not uniform for different brain tissues; gray matter increases about 150% in the first year while hemispheric white matter volume increases by only 11%. Other noticeable growth patterns are cerebellum volume increased by 240% in the first year, lateral ventricle volume increased by 280% in the

first year and a small decrease in the second; and the caudate and hippocampus increased by 19% and 13%, respectively in the second year of life.

Other studies also have investigated the maturation of neural pathways for proper functioning, and/or the correlates between structural and functional development. Gottlieb (107) distinguished between two models for this combined developmental process; “predetermined epigenesis” assumes that there is a unidirectional causal chain from genes, structural changes to psychological function while “probabilistic epigenesis” assumes bidirectional interactions between genes, structural brain development and psychological function (108). Although different theories concerning this process exist, the direct evidence proving any specific assumption remains highly challenging and demands further investigation.

4.1 Gray and White Matter development from Human Fetus to Infant

Starting from the third trimester of pregnancy to 2 years of age is a critical period for human brain development. During this time, brain undergoes rapid development through various processes such as neurogenesis, axonal and dendritic growth, synaptogenesis, cell death, axonal pruning, myelination, and gliogenesis (109).

As early as 7-10 gestational weeks, initial cortical plate formation starts in the human telencephalon, followed by neuronal proliferation at 8-16 gestational weeks, neuronal migration at 12-20 weeks and the development of six-layered cortex (110). Subsequently, cortical neurons start to develop dendrites and axons, followed by rapid elongation of axons to their intra- and subcortical target structures accompanied by the establishment of synapses and hence connectivity. Redundant axonal processes that do

not make synaptic contacts are finally selectively eliminated which is termed “axonal pruning”.

Histology-based studies also possess the potential to depict the onset and completion of various developmental events regarding critical white matter (WM) development during this period. Haynes et al (111) conducted such a study and reported the major developmental time lines for axonal maturation from midgestation through infancy. Using anti-SMI 312, a pan-marker of neurofilaments, stained axons can be observed as early as 23 weeks; GAP-43, a marker of axonal growth and elongation, showed a high level of expression from 21-64 post-conceptional (PC) weeks and progressed to a lower adult-like level beyond 17 postnatal months (~1.5 postnatal year). In contrast, myelination begins from 54 PC weeks (~ 2.5 postnatal months) to 72-92 PC weeks (~6.5 postnatal months to 11.5 postnatal months).

While knowledge gained from the above histological-based studies iss highly informative, the ability to probe white matter maturation process in vivo is highly desirable. Diffusion tensor imaging (DTI) has recently been proved to be a powerful tool in depicting the underlying structural development due to its sensitivity to microscopic motion of water molecules. Using this technique, an overall water content loss indicated by the decrease of mean trace as well as axonal growth indicated by the increase of fractional anisotropy (FA) during the first years of life have been reported (41). Further, Song et al (112) proposed that radial diffusivity ($\lambda_{\perp} = (\lambda_2 + \lambda_3)/2$) may reflect myelination process and a rapid decrease of radial diffusivity in the first 12 postnatal months has been reported, consistent with histology studies and indicating that myelination may be a dominant developing process in the first year of life (40, 41).

For specific fiber tracts, Huang et al. (113) studied both fetal (19-20 PC weeks) and neonate brains delineating various degrees of maturation status of a series of white matter structures. Specifically, they found that the limbic fibers develop first and the association fibers last. The commissural and projection fibers are forming from anterior to posterior part of the brain. Other studies also suggest WM development of the central WM regions may be earlier than the peripheral WM regions (114).

4.2 Brain functional development during early infancy

The brain undergoes continuing functional developments after birth, including motor coordination, vision, auditory perception, language, etc, during the first few years of life. Several lines of evidence suggest that even some primitive versions of "high-level" cognitive functions may already be present in very young pediatric subjects. Davidson (115) suggested that implicit memory is robustly presented in neonates and toddlers. Studies have shown that the sensorimotor experiences of the fetus (116) and the voice of mother (117) can be memorized. Fivush and Hamond (118) showed that at 2-year-old, children can already retrieve much detail about a trip to the zoo while episodic memory starts to develop at the age of four (119).

Amsterdam (120) found that infants from 6 through 12 months of age demonstrate prolonged and repeated reaction to their mirror images as a sociable playmate. Wariness, withdrawal, self-admiring and embarrassed behavior start at 14 months and has been observed in 75% of the children after 20 months of age. Finally, from 20 to 24 months of age, the majority of subjects demonstrate recognition of their mirror images. These temporal behaviors demonstrate an evolving trajectory of self-consciousness before the age of two, which is essential for self-projection or self-referential activity. In addition,

studies on toddlers also revealed that 18- to 24-month-olds are able to use speaker's gaze direction (121), affective expression (122) and other behaviors (123) as cues leading to speaker's communicative purposes. Akhtar and Tomasello (124) further proposed that children are able to infer the meaning of words through an understanding of people's minds although here the "understanding" is narrowly limited to "a sensitivity to others' referential intentions, desires and knowledge states" (125). These primitive mental functions may actually act as a promising source where more sophisticated function such as mentalizing and "theory of mind" can be originated and developed; most normally developing children acquire "theory of mind" between the age of 3 and 5 years (126).

4.3 Structural Correlates of Infant Functional Development

The development of cognitive functions and neuroanatomical maturation process are intertwined. Realization of certain cognitive function relies on the building of certain neuroconnections/pathways while the developing of function may further strengthen the corresponding pathways.

One potential connector of the brain between structural and functional development is the process of myelination. Since myelination increases the electrical conduction rate along axons, its development should be correlated with improved information transmission and a correspondingly stronger and fast connection/pathway. To test this assumption, Dubois et al(127) examined both the structural and functional development of the visual system between 1 and 4 month old infants using DTI and visual event-related potentials (VEPs) and found that the apparent conduction speed, computed from the latency of the first positive VEP wave was significantly related with DTI indices such as FA and radial diffusivity, highly suggestive of the microstructural

correlates of infant functional development. Nevertheless, only the visual system was studied, additional studies are needed to discern other potential mutual dependences between early brain structural and functional development.

Overall, brain undergoes rapid and important development during the critical first few years of life both structurally and functionally but the exact mechanisms underlying this development are currently poorly delineated. Towards quantitative assessment of early brain development, this dissertation focuses on the delineation of such mechanisms and the later chapters will describe the specific improvements/findings made in this process.

Chapter 5

Temporal and Spatial Developments of Axonal Maturation and Myelination of White Matter in the Developing Brain

Brain function has been considered to primarily originate through the cerebral cortex which is mainly composed of gray matter (GM). However, information exchange/connection between various brain cortical areas are mostly fulfilled by white matter (WM) fibers, whose dysfunction may significantly interrupt proper brain functioning. Therefore, how the development of WM is coupled with brain functional development is extremely interesting and of importance. In this Chapter, as a first step, the temporal and spatial developments of WM in normal and healthy pediatric subjects in the first years of life are discussed based on our published paper "Temporal and Spatial Developments of Axonal Maturation and Myelination of White Matter in the Developing Brain" (40). The functional development is discussed in the next Chapter and the combination of the two elements will be tackled in future work.

5.1 Introduction

The understanding of early human brain development especially the maturation process of white matter is of both great scientific and clinical importance.(41, 111, 128, 129) Several studies have specifically focused on the development of white matter in pediatric subjects using MRI. While it has been suggested that the most rapid pace of

maturation of white matter occurs during the first 2 years of life(129, 130), most of the studies to date have been carried out on either preterm babies(41, 111, 131, 132), older children(133, 134), or with a relatively small sample size during this critical period of time – from birth to 2-years of age.(128, 130, 135-138) Therefore, information on normal development of white matter in very young children is insufficient. To this end, quantitative assessment of the white matter in normal and healthy children during this critical period of time are highly desirable for the understanding of early white matter maturation.

Due to its sensitivity to microscopic motion of water molecules, diffusion tensor imaging (DTI) has become the method of choice for the measurement of local water diffusion characteristics. The underlying physical mechanism is that the relative angle (θ) between the direction of the applied diffusion gradients and the direction of water diffusion determines the extent to which MR signal is altered in the presence of diffusion gradients; the maximum signal reduction occurs at θ=0 (parallel) whereas no signal change is anticipated at θ=90-degree (perpendicular). Therefore, applying diffusion gradients along non-collinear directions, a tensor matrix can be used to characterize the directions of water diffusion. Subsequently, the three eigenvalues (λ_1 , λ_2 and λ_3) obtained through matrix diagonalization of the tensor matrix can be used to derive diffusion indices such as the relative anisotropy (RA), fractional anisotropy (FA), and volume ratio (VR). Although these indices, especially FA, have been widely employed to characterize diffusion anisotropy in various brain tissues, they lack the ability to provide more insights into the underlying micro-structural changes of white matter.

Recently, Song et al proposed to separate the three eigenvalues (λ_1, λ_2 and λ_3) into two parameters that may have different physiological implications: parallel (λ_1) and perpendicular (λ_2 and λ_3)(139-141), also known as axial diffusivity ($\lambda_{\|} = \lambda_1$) and radial diffusivity ($\lambda_{\perp} = (\lambda_2 + \lambda_3)/2$), respectively. With animal models of neurodegenerative diseases(112, 142, 143), they demonstrated that a reduction of axial diffusivity may be indicative of axonal injury whereas an elevation of radial diffusivity may reflect demyelination. Therefore, they concluded that utilizing both the axial and radial diffusivities may provide more specific physiological underpinnings of the microstructural changes in white matter than that available through FA.

In this study, Axial and radial diffusivities together with FA were employed to characterize the temporal and spatial development of axonal maturation and white matter myelination during the critical first two years of brain development. Rapid axonal growth and elongation, forming of new barriers to water mobility such as microtubules and myelination in white matter are likely to affect both axial and radial diffusivities in different ways(112, 142, 143). Characterizing the changes of these directional diffusivities should shed new light on our understanding of the underlying microstructural development in white matter over this critical period.

5.2 Materials and methods

5.2.1 Subjects

The study subjects were part of a large ongoing study of brain development in normal and high risk children. Pregnant women were recruited during the second trimester of pregnancy from the outpatient obstetrics and gynecology clinics at UNC hospitals. Exclusion criteria were the presence of abnormalities on fetal ultrasound or

major medical or psychotic illness in the mother. Informed consent was obtained from the parents and the experimental protocols were approved by the institutional review board. None of the subjects was sedated for MR imaging. Before neonates were imaged, they were fed, swaddled, and fitted with ear protection. In contrast, for the 1yr- and 2yr-olds, the parent or a study coordinator held them and sat on a rocking chair inside the MR scanner until the subject fell asleep. Headphones were put on the subject who was then placed in the head coil. With these procedures, most of the subjects slept during the imaging examination. We retrospectively identified 60 normal subjects including 20 neonates (12 male and 8 female, mean age 22 ±10 days (SD)); 20 1-year-olds (8 male and 12 female, mean age 13 ±0.5 months) and 20 2-year-olds (10 male and 10 female, mean age 24 ±0.5 months) who met the following inclusion and exclusion criteria. Inclusion criteria were birth between the gestational ages of 35 and 42 weeks, weight that was appropriate for gestational age, and the absence of major pregnancy and delivery complications as defined in the exclusion criteria. Exclusion criteria included maternal pre-eclampsia, placental abruption, neonatal hypoxia, or any neonatal illness requiring greater than 1 day NICU stay, mother with HIV, any mother actively using illegal drugs/narcotics during pregnancy, or any chromosomal or major congenital abnormality. In addition, all DTI images were visually inspected and subjects with apparent motion in DTI images were excluded. Finally, a board-certified neuroradiologist (JKS) reviewed all images to verify that there were no apparent abnormalities in the acquired MR images.

5.2.2 MR Acquisition

All imaging was performed on a head-only 3.0-T MR imaging unit (Allegra; Siemens Medical Systems, Erlangen, Germany). One image without diffusion gradients

together with diffusion weighted images along six gradient directions with a b-value of $1000\,mm^2/s$ were obtained. The acquisition was repeated 5 times for averaging. Other imaging parameters were: TR/TE=7500/73 ms; slice thickness=2 mm with an inter-slice spacing of 2mm; matrix size =64x64; and an in-plane resolution=2*2 mm^2.

5.2.3 Post-processing

Diffusion weighted images were transferred off-line for post-processing using software developed in-house. Six elements of the diffusion tensor were determined by multivariate least-square fitting. Three eigenvalues and eigenvectors were obtained by tensor diagonalization and subsequently the axial and radial diffusivities were calculated. Fractional anisotropy was calculated to measure degree of anisotropy.(36, 37, 144)

BET algorithm of the FSL (FMRIB, Oxford University, U.K.) was applied to exclude all voxels outside of the brain for further analysis. Subsequently, one subject in each age group was chosen as the template and bi-directional B-spline co-registration, which ensured symmetry between source images and template images. The distance between knots of the 3D B-spline model was gradually decreased by half, leading to an increase of grid size of the 3D control point array from 5*5*5, 7*7*7, 11*11*11 and finally to 19*19*19. This allowed registration of individual subjects to their corresponding template using the FA maps. The transformation matrices were saved for each individual with subsequent co-registration of the axial and radial diffusivity maps to the templates. After registration, mean FA maps were calculated for each age group.

5.2.4 Region-of-Interest (ROI) Analysis

Eight ROIs were placed on the mean FA maps for each age group by a board certified neuroradiologist (VJ). These ROIs include: genu of corpus callosum (GCC);

splenium of corpus callosum (SCC); body of corpus callosum (BCC); posterior limb of internal capsule (IC); cortical-spinal tract (CST); optic radiation (OR); frontal peripheral white matter (FPW); and posterior peripheral white matter (PPW). These ROIs were chosen such that both central and peripheral white matter areas were included so as to assess the temporal and spatial alterations of diffusion anisotropy and directional diffusivities across different white matter regions. The ROI sizes varied between different groups owing to the changes in brain size. For the neonate group, the number of voxels in each ROI ranged from 8 to 20 with a median of 10 while the ROI sizes were similar between the 1 and 2yrs old groups and ranged from 10 to 45 with a median of 18 voxels. The values of FA, and axial and radial diffusivities for each ROI were then obtained for each individual subject, which were then used for subsequent group analysis.

5.2.5 Statistical Analysis

The analysis of variance (ANOVA) for multiple comparisons with age as the single factor was used for statistical analyses. A $P<0.05$ was considered significance.

5.3 Results

Representative examples of the axial and radial diffusivities and FA for the three age groups are shown in Fig.5.1, demonstrating the excellent image quality. It is apparent that marked changes in all three parameters are seen between neonates and 1 yr olds while the differences between 1yr and 2yr olds are more subtle. A direct comparison of the three diffusion parameters among the three age groups is shown in Fig. 5.2 where the values represent the mean of all ROIs of each age. Consistent with the reported results in the literature, FA increases as a function of age; a significant increase in FA is observed from neonates to 1 yr olds ($p<0.0001$) while the FA is comparable

between 1yr and 2yrs olds ($p>0.05$). In contrast, both axial and radial diffusivities decrease with age. Similar to that observed in FA, the major changes of axial and radial diffusivities occur between neonates and 1 yr olds ($p<0.0001$) while only the radial diffusivity exhibits significant reduction from 1 yr to 2 yrs olds ($p=0.0014$).

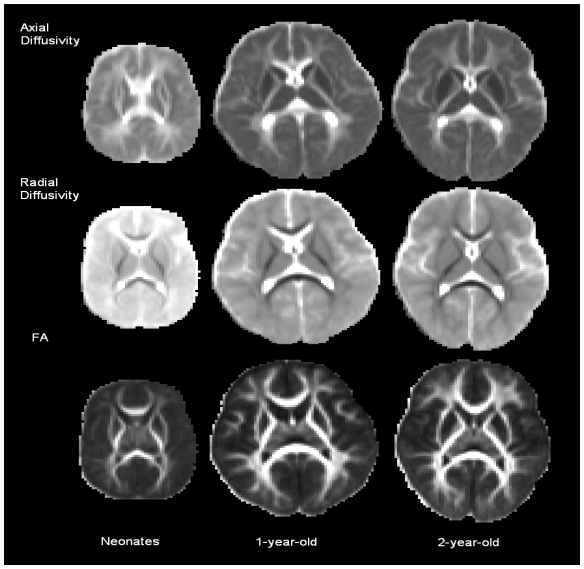

Figure 5.1 Representative examples of axial diffusivity, radial diffusivity and FA from three subjects, one subject for each age group, are shown. All images were scaled to the same window and level settings to allow a direct comparison across subjects. It is apparent that both the axial and radial diffusivities decrease whereas the FA increases with age.

To further examine how white matter maturation differs with age across different anatomical regions, the general pattern are showed in Fig. 5.3; FA increases and both axial and radial diffusivities decrease with age for all ROIs. However, there is a substantial variability across different anatomical regions. Fig.5.3 provides more detailed analysis on anatomical locations exhibiting statistical differences among groups. All

three diffusion parameters are highly significantly different between neonates and 1yr olds for all ROIs. In contrast, anatomical regions exhibiting statistical changes differ among the three diffusion parameters between 1yr and 2yrs old groups. For the axial diffusivity, only the frontal peripheral WM area (FPW) and OR show significant changes. Interestingly, with the exception of SCC, all ROIs exhibit significant changes for radial diffusivity from 1yr to 2yr olds albeit the statistical significance levels are different. Finally, with the exception of the FPW and SCC, the FA is statistically different between 1 yr and 2yr olds for all remaining ROIs.

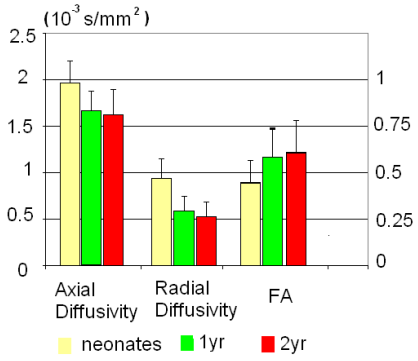

Figure 5.2: The mean values of the axial diffusivity, radial diffusivity and FA from all 8 ROIs are shown. A significant reduction ($p<0.0001$) of both axial and radial diffusivities and elevation ($p<0.0001$) of FA are observed from neonates to 1 yr olds. The changes from 1yr to 2yrs olds are more subtle for both axial diffusivity and FA while a significant reduction ($p=0.0014$) in radial diffusivity is observed. The labels for left and right Y-axis represent the directional diffusivities and FA, respectively. Error bars indicate standard deviation.

The rates of increase/decrease of diffusion parameters with age are shown in Fig. 5.4 for different anatomical regions. The axial and radial diffusivities and FA of 1 and 2 yrs old groups were normalized to the corresponding values at each ROI of the neonatal

group. A rapid decrease in both axial and radial diffusivities while a marked increase in FA are observed from neonates to 1yr olds, followed by a relatively stable axial and radial diffusivities and FA from 1 yr to 2yrs olds. Comparing between axial and radial diffusivities, radial diffusivity reveals a much larger reduction than that of axial diffusivity from neonates to 1yr olds. The reduction of axial diffusivity between neonates and 1yr olds ranges from almost no changes (94.5%) for CST to 76% of that at neonates for FPW. In contrast, the smallest reduction of radial diffusivity is 79% (OR) and the largest is 44% (SCC) of that of neonates. The most substantial increase in FA from neonates to 1yr olds is the FPW while the smallest is CST.

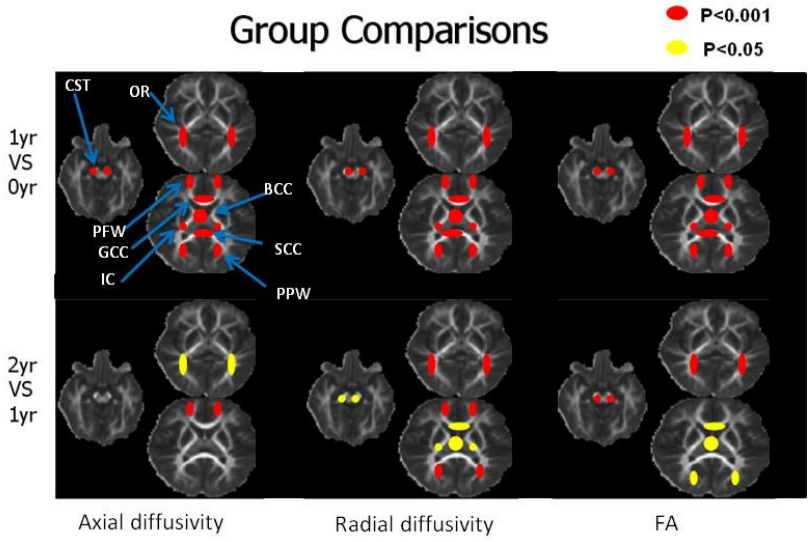

Figure 5.3: Statistical comparison results overlaid on FA maps are shown. Please note that the body of corpus collosum should be located in different slices but it was shown on the same slice for visualization. GCC: genu of corpus callosum; SCC: splenium of corpus callosum; BCC: body of corpus callosum; IC: posterior limb of internal capsule; CST: cortical-spinal tract; OR: optic radiation; FPW: frontal peripheral white matter; and PPW: posterior peripheral white matter.

Finally, the comparisons of the three diffusion measures at the same age but different anatomical areas reveal the spatial behaviors of white matter maturation (Fig. 5.5). This figure is shown in such a way that the values of axial diffusivity and FA are sorted in a descending order while the radial diffusivity is sorted in an ascending order based on the values of the 2yrs old group. Generally speaking, the results from 1 yr group (pink line) and 2 yr group (green line) show a consistent trend while the neonate group (blue line) is more variable and does not follow the same patterns as those shown in 1 and 2 yrs old groups. The general trend indicates that the corpus callosum (GCC, SCC, BCC) has the highest axial diffusivity and FA, followed by CST, OR, IC, and the lowest in the peripheral WM area (PPW, FPW). The radial diffusivity increases follow a similar pattern to that of the axial diffusivity with the exception that the development of IC appears more advanced when compared to that of the GCC and BCC.

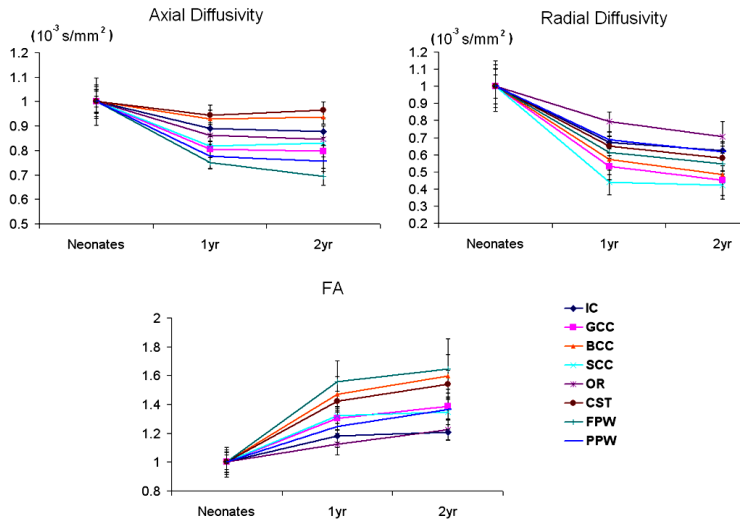

Figure 5.4: Comparisons of axial diffusivity (a), radial diffusivity (b) and FA (c) across age. The experimentally measured values of 1yr and 2yrs groups are normalized to that of the neonates. GCC: genu of corpus callosum; SCC: splenium of corpus callosum;

BCC: body of corpus callosum; IC: posterior limb of internal capsule; CST: cortical-spinal tract; OR: optic radiation; FPW: frontal peripheral white matter; and PPW: posterior peripheral white matter. Error bars indicate standard deviation.

5.4 Discussion

Diffusion tensor imaging has been widely employed to assess white matter maturation in pediatric subjects (41, 111, 113, 114, 128-137). However, few studies thus far have specifically focused on the age range investigated in our study, particularly with a large sample size. In addition, most of the studies to date have mainly employed FA to delineate white matter maturation which may not provide the information about underlying microstructural changes with age. In this study, both axial and radial diffusivities along with FA were employed to gain more insight into the underlying biological development associated with white matter maturation, namely axonal growth and myelination. Consistent with the results reported in the literature(129, 130), a marked increased in FA from neonates to 1yr olds is observed, followed by a more subtle increase from 1yr to 2yr olds. The ROI analysis offers additional details regarding the spatial pattern of white matter maturation. Specifically, all 8 ROIs exhibit highly significant ($p<0.0001$) elevation of FA from neonates to 1yr olds (Fig. 5.3), indicating a rapid development of white matter during the first year of life. However, with the exception of CST and OR which exhibit highly significant elevation of FA from 1yr to 2 yrs olds ($p<0.001$), the level of statistical significance is reduced ($p<0.05$) in GCC, BCC, and PPW. In addition, the FA values in the SCC, IC, and FPW are comparable between the 1 yr and 2yr groups although the physiological underpinnings for the lack of FA changes in SCC, IC, and FPW may differ. It is plausible that both SCC and IC are well

developed by the age of 1 yr old and thus exhibit subtle changes in FA. In contrast, the FA values are about 0.3 at the FPW at 1yr and 2yrs old and thus most likely reflect the slow pace of white matter development in the frontal lobe from 1 to 2yr olds. However, caution should be taken in interpreting these results based on FA findings alone and consideration should be given in the context of both axial and radial diffusivities.

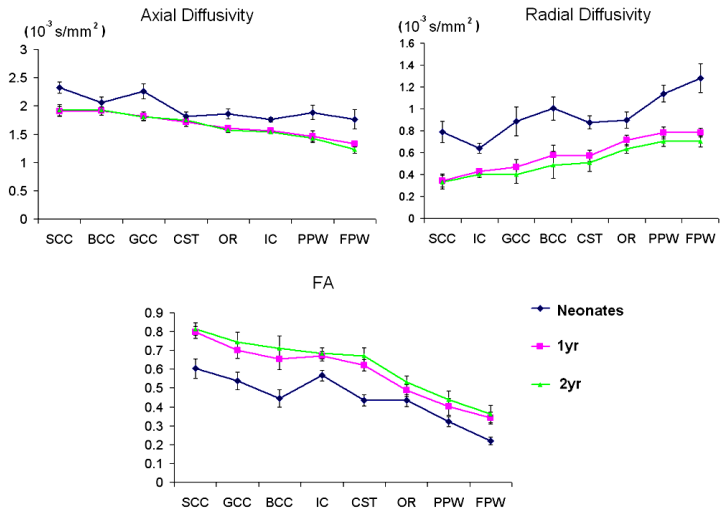

Figure 5.5: Comparisons of the axial diffusivity (a), radial diffusivity (b) and FA (c) across ROI but at the same age are shown. GCC: genu of corpus callosum; SCC: splenium of corpus callosum; BCC: body of corpus callosum; IC: posterior limb of internal capsule; CST: cortical-spinal tract; OR: optic radiation; FPW: frontal peripheral white matter; and PPW: posterior peripheral white matter.

In addition to FA measurements, both axial and radial diffusivities, reflecting axonal growth and formation of new barriers - myelination(112, 142, 143), respectively, were employed in our studies to potentially provide additional insights into white matter development from the ages of 3wks to 2yrs old. Haynes et al (111) utilized GAP-43, a marker of axonal growth and elongation to analyze parietal central white matter tissues.

They showed a high level of GAP-43 staining from 24-64 post-conceptional (PC) weeks which spans through pre- and post-natal periods, implying rapid axonal development which progressed to a slower adult-like level of axonal development beyond 17 postnatal months (~1.5 postnatal year). In contrast, myelination begins from 54 PC weeks (~ 2.5 postnatal months) to 72-92 PC weeks (~6.5 postnatal months to 11.5 postnatal months), spanning approximately the entire first year after birth. Together, these results suggest that the onset of axonal growth is earlier (pre-natal) and most rapid during the first five postnatal months while myelin maturation begins about 2.5months postnatally and continues throughout the first year of life. Therefore, with regard to measurements of axial and radial diffusivities, one would expect smaller changes of axial diffusivity during the first year of life than the changes of radial diffusivity (myelination) since maturation of myelin is the dominant process during this period of life. Indeed, Partridge et al(41) reported a smaller changes of λ_1 (axial diffusivity) whereas both λ_2 and λ_3 (radial diffusivity) exhibited a marked changes in 14 preterm newborns imaged at gestational ages between 28 and 43 wks. Similarly, our study (Fig. 13) demonstrates that the extent to which radial and axial diffusivity reduction differs during the first year of life; the axial diffusivity decreases to about 0.75~0.95 while radial diffusivity reduces to 0.44~0.69 of that in the neonate group, suggesting more rapid myelination than axonal growth from 3wks to 1yr of age. Our findings are thus highly consistent with that reported by Haynes et al. (111)

While all of the 8 ROIs exhibit significant changes of axial and radial diffusivities from neonates to 1 yr olds, these same regions begin to differ with regard to how the axial and radial diffusivities change from 1 yr to 2 yrs of age (Fig. 5.3). The OR and FPW

reveal significant changes in axial diffusivity consistent with continued axonal development, whereas with the exception of the SCC, the remaining 7 ROIs exhibit significant changes in radial diffusivity, suggesting that the myelination is the dominant process during the second year of life in these areas. In addition, as mentioned previously, no changes in FA were observed in SCC, IC and FPW from 1 to 2 yrs old. Based on the FA findings, our initial interpretations, as discussed above, were that the SCC and IC are well developed whereas the developmental pace in FPW is slow. Consistent with the finding of FA, no changes in both axial and radial diffusivities were observed in SCC. However, some discrepancies are observed in both IC and FPW. Both axial and radial diffusivities exhibit significant changes in FPW, indicating continuing rapid myelination and axonal growth during this period in contradistinction to our original interpretation based on FA. In addition, a significant reduction of radial diffusivity in IC is observed, suggesting continuing myelination. Furthermore, although a significant elevation in FA is observed at the CST, GCC, BCC and PPW between 1 and 2yrs olds, these regions only exhibit significant changes in radial but not axial diffusivity, suggesting that these regions are going through extensive myelination but not axonal growth during this period of life. Together, these results underscore the importance of utilizing axial and radial diffusivities and reveal the limited specificity of solely using FA to characterize the development of white matter. Nevertheless, one must note that the radial diffusivity measurements assume that the axons exhibit a perfect cylindrical shape and no contributions to the diffusivity perpendicular to the axons. As a result, effects of astrocytes, microglia and cell surface molecules extended into the intersitium are ignored.

Our comparison of diffusion parameters using ROIs in each age group reveals the spatial maturation pattern of white matter. Despite the neonatal group variability, the general maturation pattern begins centrally (SCC, GCC, and BCC), followed by GST, IC, OR and peripheral white matter (PPW and FPW) development as well as from the occipital (PPW) to the frontal (FPW) lobes. These findings are consistent with the results reported by Volpe.(145) Interestingly, although discrepancies regarding the rates and anatomical locations among the three diffusion parameters are observed, the general spatial pattern was consistently depicted using the three diffusion parameters.

It must be noted that Song et al(112, 142) hypothesized and subsequently demonstrated in animal models that a reduction of axial diffusivity was associated with axonal injury in mouse models. Contrary to their conclusion, we demonstrate axial diffusivity decreases from the neonatal period to 2 yrs of age which clearly cannot be explained by axonal injury. In addition, it has also been reported by Ashtari et al(146) that axial diffusivities increase and there are no changes in radial diffusivity with age. These authors speculated that the reduction of fiber tortuousity yields more straightened fibers, improving axonal fiber organization and potentially leading to an increase of axial diffusivity.(146) The discrepancies between our findings and these studies can potentially be explained by the following factors. First, subjects with a mean age of 16.6 yrs old were studied by Ashtari et al which is clearly much older than our studies. Second, it has been documented that axonal pruning occurs resulting in refinement of the embryonic nervous system during early development(147). Thus, the intermingling of axonal branches, the elimination of overabundant axons, and the reduction of the length of axons during the refinement process may potentially account for the observed

reduction in axial diffusivity. (148, 149) Finally, postnatal development of the fiber cytoskeleton, i.e. the formation of microtubules and neurofilaments (150) may also contribute to the decreased axial diffusivity as new barriers form. Therefore, it is plausible that the relationship between axial diffusivity and age is biphasic where a reduction of axial diffusivity is present during the first years of life, and followed by an elevation of axial diffusivity at a later age. Specifically, axonal pruning and formation of new barriers may be the dominant factor resulting in the observed reduction of axial diffusivity. However, once axonal pruning and cytoskeleton development reaches a plateau, fiber straightening may then become the dominant factor, leading to increased axial diffusivity at a later age. These physiological alterations may also explain the gradual decreasing pattern of axial diffusivity from the central WM (i.e. different parts of CC) to the peripheral WM (Fig. 14a) since the central WM is more likely to have well organized straight fibers while axonal fibers become less organized in the more peripheral areas. Nevertheless, more studies with a wider age range is needed to further determine at what age the axial diffusivity starts to increase after birth.

Two potential limitations associated with our study need further discussion. First, six diffusion gradient directions were employed in our study. The choice of the number of diffusion gradient directions reflects a compromise balance the data acquisition time and signal-to-noise ratio of DTI for imaging non-sedated pediatric subjects. While the utilization of six diffusion gradient directions may lead to inaccuracy of the measurements of diffusion tensors, since an ROI approach was employed with a large sample size, the potential inaccuracy in tensor measurements should not affect the overall conclusions of our study. Second, despite the histological correlatives reported by Song

et al indicating that axial and radial diffusivities may reflect axonal integrity and myelination, definitive physiological underpinnings of axial and radial diffusivities remain to be enlightened. Therefore, although our results appear to be consistent with the general understanding of the white matter maturation in pediatric subjects, the interpretation of our results should be in the context of these limitations.

5.5 Conclusion

Utilizing both FA and directional diffusivities, namely axial and radial diffusivities, this study aimed to determine the spatial and temporal characteristics of white matter development in normal and healthy children from 3wks to 2 yrs of age, an age range that currently lacks sufficient data. Our results demonstrate that the major changes of FA, and radial and axial diffusivities occur from 3 weeks to 1yr for all regions investigated – with elevations of FA and reductions of both axial and radial diffusivities. In addition, much larger reductions in radial diffusivity are observed when compared with those demonstrated in axial diffusivity, suggesting that myelination is the dominant process during the first year of life. In contrast, the changes between 1 yr and 2 yrs olds are more subtle although statistical differences are observed in radial diffusivity suggesting a pruning process. In addition, our results indicate that FA alone cannot differentiate the components of white matter maturation. Our study reveals more insight into the underlying biological changes of white matter which are only obtained when all three diffusion parameters are interpreted together. Finally, comparing diffusion parameters across different ROIs in each age group reveal that the development of white matter begins from center to peripheral white matter and from occipital to frontal lobes.

Chapter 6

Emergence of the brain's default network: Evidence from two-week-old to 2-year-old healthy pediatric subjects

Brain is a complex, structured and dynamic system facilitating various functions. Rather than investigating brain function in forms of isolated brain regions, studies have shown the indispensability of viewing the brain as an integrated system consisting of spatially segregated yet actively interacted regions, which essentially form "functional networks" (151, 152). Recent studies further show that such a network organization of brain persists even when subjects are lying in the scanner doing no explicit cognitive task other than "resting" (20, 22). For our interest of characterizing brain development in pediatric subjects, resting state fMRI is particularly suitable and provides us unique opportunity to explore the underlying functional development trajectory for the first time.

Brain has various specific functional networks such as motor-sensory, visual, language, attention, etc. However, one of the major findings in recent fMRI studies is that a distinct brain network – referred to as the default network (26)– is engaged during passive or undirected "resting" mental states. For this reason, in this chapter we first tackled the development of this particular network using functional connectivity MRI (fcMRI) to depict its developing trajectory in the first 2 years based on our published paper titled "Emergence of the brain's default network: Evidence from two-week-old to 2-year-old healthy pediatric subjects" (153). The developing process of other networks and the whole brain as a comprehensive network will be discussed in following chapters.

6.1 Introduction

A growing body of evidence suggests that a distinct brain network – referred to as the default network – is engaged during passive or undirected mental states (26). Broad awareness of the default network emerged when Shulman et al (154) conducted a meta-analysis, pooling resting positron emission tomography (PET) images from 132 normal subjects who underwent a variety of goal-directed cognitive tasks (e.g., word reading, category classification, etc.). Remarkably, despite the differences in activation paradigms among the subjects, several brain regions consistently exhibited a higher cerebral blood flow (CBF) during undirected (passive) states than during cognitive task conditions. It was suggested that the increased brain activity (CBF) during the passive condition reflected ongoing thoughts and monitoring of the external environment. Subsequently, a series of seminal studies were conducted and reported by Gusnard, Raichle and colleagues which focused on the functional significance of such increased brain activity during resting/passive conditions (26, 155). The term "default mode of brain function" was thus coined by Raichle et al (26), describing the baseline state in the human brain. Since then, substantial efforts have been devoted to further determining the anatomical and functional implications of the brain's default network using both PET and MRI techniques (154, 156-158).

Remarkably, despite the utilization of different neuroimaging methods including PET (154, 156) and resting functional magnetic resonance imaging (rfcMRI) (157, 158), a consistent pattern of the main architecture of the default network has been reported across different studies and modalities. Specifically, these reports suggest that the default network consists mainly of the ventral/dorsal medial prefrontal cortex (v/d MPFC),

posterior cingulated cortex/retrosplenial (PCC/Rsp), inferior parietal lobule (IPL), lateral temporal cortex (LTC) and hippocampus regions (HF) (28). This convergence in anatomical representations of the brain among different neuroimaging approaches suggests that the default network is likely to be a distinct brain system with its own function, and for which dysfunction may have great impact on various brain diseases (159).

While the anatomical representations of the default network are highly consistent in the literature, the specific functions of the default network remain controversial (21, 26, 27, 160). In adult studies, the default network is typically reported as an intact network indicating a temporally synchronized functional composition (48). However, evidence also suggests that the default network has specialized subsystems that converge on two main "hubs" – PCC/Rsp and MPFC (161). Uidden et al (161) investigated the two hubs of the default network and found that the interaction patterns with other networks are significantly different for these two hubs, suggesting functional differentiation within the default network. Nevertheless, to date most of the existing literature on default network focuses largely on adult subjects. As a result, it is difficult to determine how and when the default network is formed. The delineation of its developmental process not only offers profound scientific implications on its functional evolution during a critical time period when the brain undergoes tremendous development (129) but also potentially provides great insights into the etiology and pathophysiology of neurodevelopmental disorders. Fair et al (101) investigated default network in school-age children (i.e. 7-9 years old) and found that the network is only sparsely connected in children when compared with adults. Fransson et al scanned pre-term infants at a gestational age of 41

weeks and failed to discern the default network (162). Based on these two studies, one would hypothesize that the default network cannot be completely discerned up to 7-9yrs old, assuming a monotonic developing trend. However, subjects in Fransson et al's studies were born prematurely, which made it unclear whether or not their findings are applicable to healthy infants. Moreover, whether the development of this particular network follows a monotonic pattern remains elusive without data actually covering the age gap. To this end, our studies aimed to reveal the temporal development of the default network by partially filling the age gap between Fair et al's (101) and Fransson et al's studies (162), determining the emergence of the default network as a whole as well as potentially discerning the presence or absence of the specialized subsystems (hubs) within the default network in a critical time period of brain development.

6.2 Methods

6.2.1 Subjects

The study subjects were part of a large study on characterizing brain development in normal and high risk children (163). Informed consent was obtained from the parents and the experimental protocols were approved by the institutional review board. None of the subjects was sedated for MR imaging. Before the subjects were imaged, they were fed, swaddled, and fitted with ear protection. All subjects slept during the imaging examination. We retrospectively identified 71 normal subjects including 20 neonates (9M, 24±12days (SD)); 24 1-year-olds (16M, 13±1mon) and 27 2-year-olds (17M, 25 ±1mon) who met the inclusion and exclusion criteria. In addition, 15 (11M, 30±1.7yrs) healthy adult subjects were also recruited for comparisons with pediatric subjects. A

board-certified neuroradiologist (JKS) reviewed all images to verify that there were no apparent abnormalities in the acquired MR images.

6.2.2 MR acquisition

A 3D MP-RAGE sequence was used to provide anatomical images to co-register among subjects. The imaging parameters were as follows: repetition time (TR)=1820ms; echo time (TE)=4.38 ms; inversion time=1100ms; 144 slices; and voxel size = 1x1x1mm^3. For the rfcMRI studies, a T2*-weighted EPI sequence was used to acquire images. The imaging parameters were as follows: TR=2sec, TE=32 ms; 33 slices; and voxel size =4x4x4 mm^3. This sequence was repeated 150 times so as to provide time series images.

6.2.3 Post-processing

The brain extraction tool of the FSL (FMRIB, Oxford University, U.K.) was first applied to exclude all voxels outside of the brain. Subsequently, rfcMRI data preprocessing included compensation of slice-dependent time shifts, rigid body correction for inter-volume head movement within runs, and spatial smoothing (6-mm full width at half maximum Gaussian kernel). The first time point rfcMRI was co-registered to the corresponding T1-weighted MP-RAGE structural images using affine rigid body alignment. Image normalization for each age group was then achieved by choosing one subject of each age group as template and then performing intensity-based hammer nonlinear registration (164) on T1-weighted structural images. Finally, the transformation fields from affine alignment and hammer registration steps were employed to bring all fMRI volume data to the template space, allowing group analysis.

Principal component analysis (PCA) was employed for data dimension reduction while the infomax algorithm (165) was applied for ICA analysis on dimension reduced

data set to obtain a set of aggregate independent components for each age group. The number of components for each age group was determined using the minimum description length criteria (166), which was 28, 31, 27 for neonate, 1yr and 2yr groups, respectively. This group ICA was carried out using GIFT software (http://icatb.sourceforge.net/) proposed by Calhoun et al (167).

6.2.4 Group Default Network Definition

After group ICA, ICA components associated with vessels, cerebral spinal fluid (CSF) and possible motion artifacts were first removed. Subsequently, template MP-RAGE images were normalized to the Montreal Neurological Institute (MNI) EPI template using intensity-based HAMMER nonlinear registration (164) and the corresponding transformation field was then used to bring the remaining IC maps in each group to the MNI template space. Regional parcellation was then achieved using the anatomically labeled template reported by Tzourio-Mazoyer et al (168). An automated approach (169) was employed to select the component(s) comprising brain regions that best matched with the commonly observed brain regions in the default network, including bilateral medial superior frontal and bilateral posterior cingulate gyrus (26, 28). This approach was first applied in the adult group where the ICA component 10 (Fig. 15) exhibited a much higher matching score when compared with the remaining components, suggesting that component 10 was associated with the default network. Indeed, the anatomical regions observed in 10^{th} ICA component (Fig. 6.2 and Table 2) are highly consistent with that reported in the literature (28). Subsequently, the brain regions of the 10^{th} component of the adult group were then used as the template to identify components of the default network for all three pediatric groups. In contrast to adults, there was not a

clear choice of the component(s) to best discern the default network in pediatric subjects (Fig. 6.1). To circumvent this difficulty, we have arbitrarily chosen a matching score threshold based on the adult studies; the component exhibited a matching score greater than 1 was considered as the component reflecting the default network. As a result, two components were chosen as the default network for the 1yr and 2yr old groups, respectively, while three components were identified for the neonates group (circles, Fig.6.1).

6.2.5 Correlation/statistical Analysis

Although PCA/ICA was done with all subjects in each age group, the mean time course of each ROI was separately extracted from each individual subject to construct a correlation matrix. Prior to computing correlations, the mean time course was low pass filtered at 0.08 Hz. Subsequently, in order to combine correlation coefficients (r) across subjects in each age group, Fisher's Z-transform was applied for each subject and averaged across subjects so as to compute the mean correlation matrix for each group (transformed back to correlation values for analysis). One-sample t-test (two-tailed) on the Fisher's Z-transformed group mean value for each connection was performed to determine whether it was significantly different from zero. The false discovery rate (FDR) approach (170) was applied to correct for multiple comparisons, achieving the expected proportion of type I error to $\alpha<0.05$. In order to also investigate the connection pattern of each specific region with all other regions within the network, the mean connection strength (average of the connection values of each region with all other regions) was also calculated using the Fisher's Z-transformed value and transformed back to correlation values for presentation.

6.2.6 Graphs

To visualize the connection pattern of different regions within the default network, the spring embedding algorithm was applied to calculate the position of each node (ROI) based on the group mean correlation matrices. In these graphs, the most strongly connected regions were clustered near each other while weakly correlated regions would be placed further away from each other. In addition, the width of the line between two nodes was proportional to the corresponding connection strength. Only significant correlations ($P<0.05$ after correcting for multiple comparisons) were plotted.

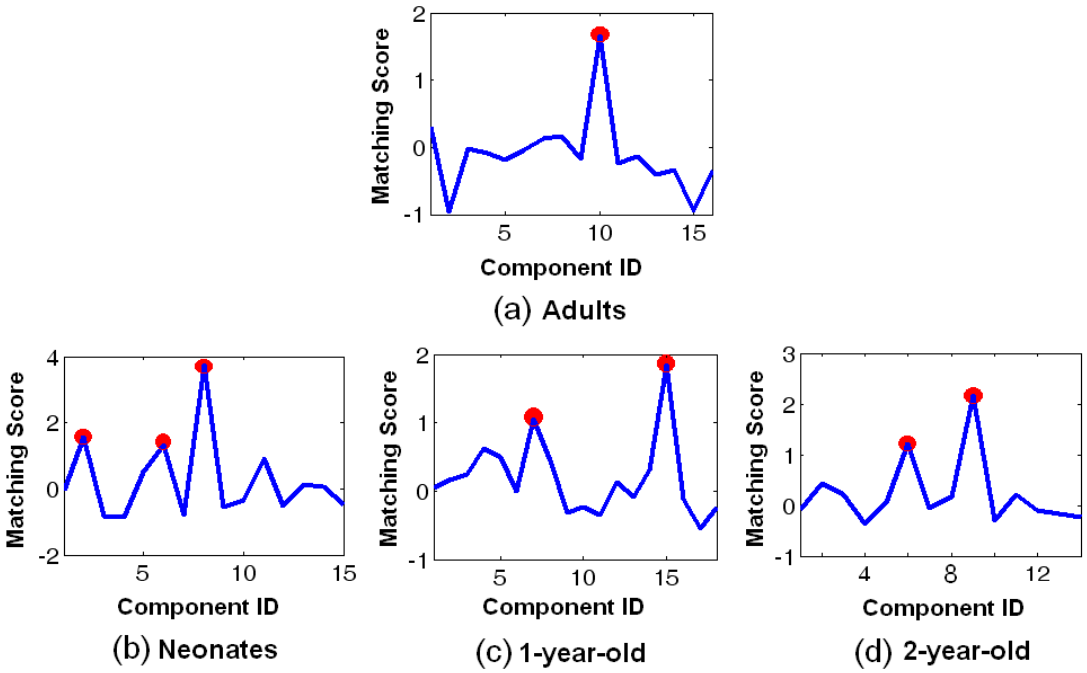

Figure 6.1 Template matching score plots for all four age groups: (a) neonates; (b) 1yr olds; (c) 2yr olds; and (d) adults. X-axis is the component index and Y-axis represents the matching scores. Circles indicate the components selected comprising the default network.

6.3 Results

Using a group independent component analysis (ICA) approach (167), an automated procedure (169) was employed to select the component(s) comprising brain regions that best matched with the commonly observed brain regions in the default network (28). The anatomical representations of the default networks for all groups are shown in Fig. 6.2; the volume ratios and mean Z scores of these anatomical regions are offered in Table 6.1. The corresponding surface rendering is provided in Fig.6.3. It is evident that the anatomical representations of the default network in adults are highly consistent with that reported in the literature (28). In contrast to the adult's default network, the temporal and spatial evolution of the default network in pediatric subjects is summarized below.

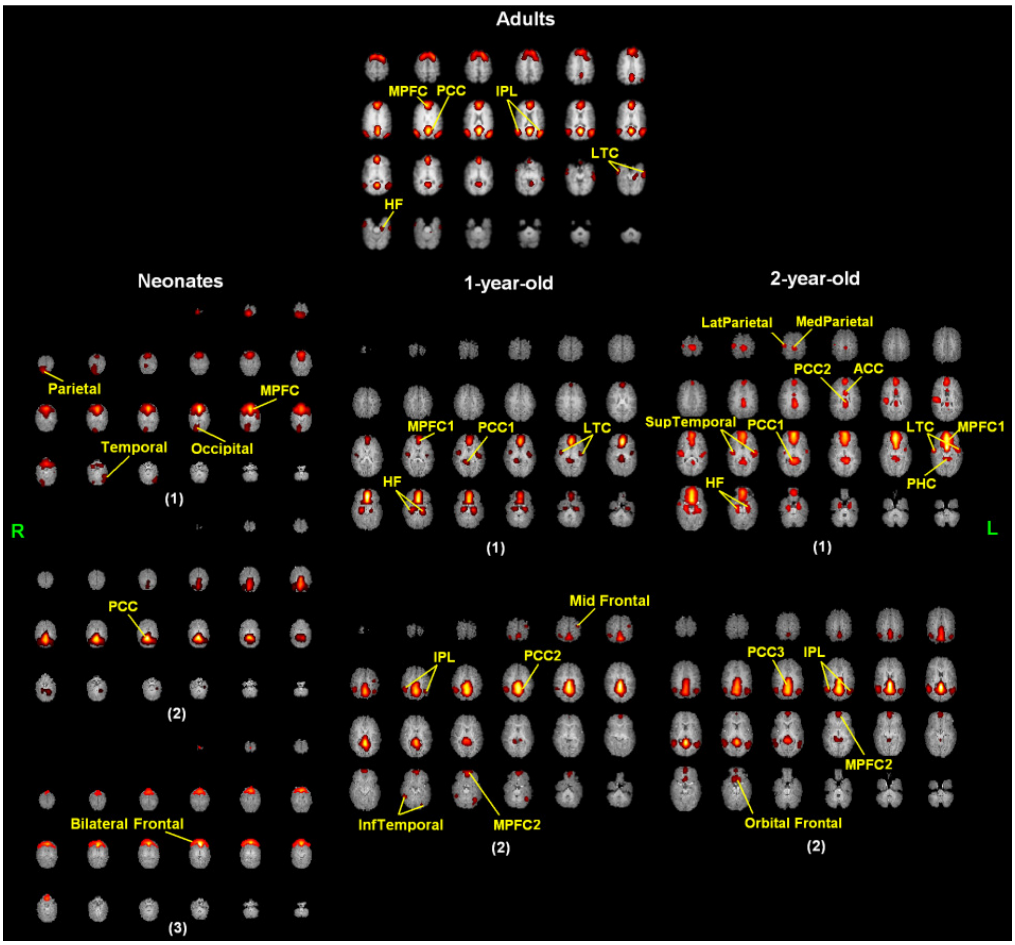

Figure 6.2 Spatial ICA identified default network components in each age group are shown. The anatomical locations of each group are labeled in the figure. Abbreviations: MPFC: ventral/dorsal medial prefrontal cortex; PCC: posterior cingulated cortex/retrosplenial; LTC: the lateral temporal lobe, HF: the hippocampus formation; IPL: inferior parietal lobe; PHC: parahippocampal cortex; ACC: anterior cingulate cortex; InfTemporal: inferior temporal cortex; SupTemproal: superior temporal cortex; MedParitetal: medial parietal cortex; LatParietal: lateral parietal cortex; MidFrontal: middle frontal cortex.

A rather primitive/incomplete default network consisting of 6 brain regions is observed in neonates. At 1yr old, a total of 13 regions are observed with 10 of them covering regions consistent with that observed in adults, including v/d MPFC, PCC/Rsp, bilateral LTC, bilateral IPL, and HF (28). However, the remaining 3 regions have not been reported in adult studies, including the parietal and bilateral inferior temporal regions. Similar to that observed in 1yr olds, the default network of the 2yr olds consists of 13 regions covering anatomical locations consistent with adults plus additional 6 regions, including the orbital frontal, anterior cingulate cortex (ACC), right parietal, medial parietal, and bilateral superior temporal regions. It is worth pointing out, despite the temporal and spatial evolution of the default network from neonates to 2yr olds, both the v/d MPFC and PCC/Rsp are consistently observed across the three pediatric groups. In addition, the volume ratios (volume in a specific region/total intracranial volume) of the MPFC and PCC/Rsp are the highest in each age group but are inversely proportional with age (Fig. 6.2 and Table 6.1): it starts from 12.9%/11.8% (MPFC / PCC/Rsp) in

neonates, reduces to 4.3%/5.9% in 1yr olds, 5.6%/5.6% in 2yr olds, and 4.02%/1.8% in adults. The latter finding is of interest. Although not specifically focused on the default network, Johnson suggested that the infant brain often employs a larger area of cortex than those used in adults (108), consistent with our findings.

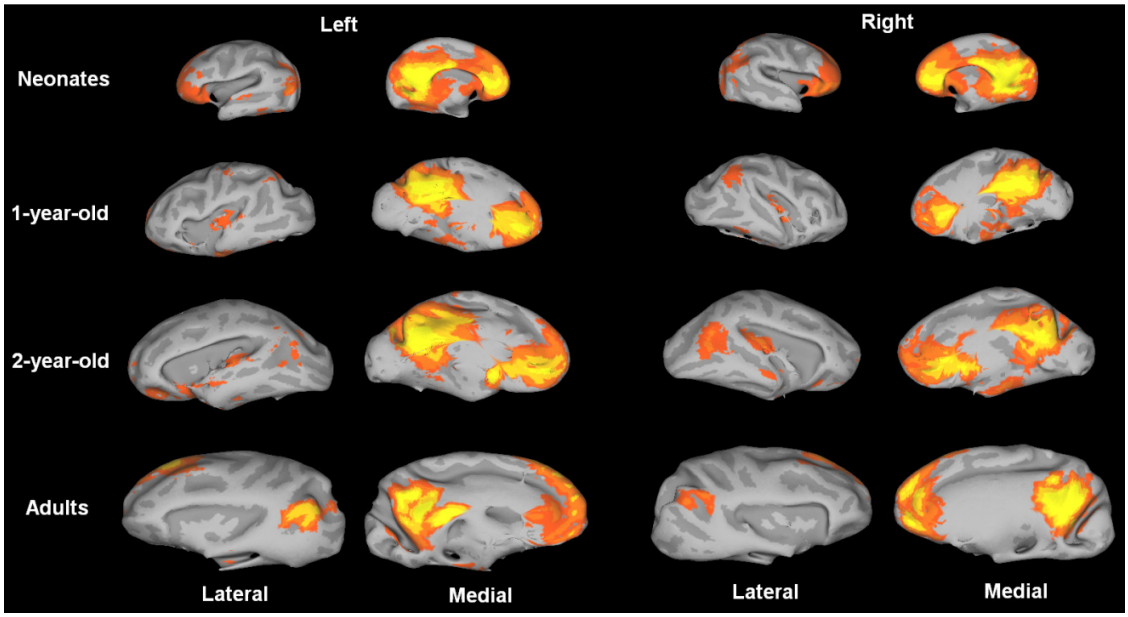

Figure 6.3 The brain's default networks in all four age groups. Z score maps (Z>1) are mapped on to the template brain surface for each individual group. For the pediatric groups, although more than one components were chosen, they were pooled together to show on the same brain surface (Z scores showed here is taken as the maximum from different components).

In order to discern the interactions among the identified brain regions of the default network, the averaged group correlation matrices were used for graph analysis after test of significance of specific connections (170). The spring embedding method (171) was used to depict the connection pattern of each group (Fig. 6.4a). These graphs

were arranged such that the most strongly connected regions were drawn close to each other and placed in the center of the graph and vice versa. In addition, the width of the connecting lines indicated the connection strengths. A summary of the mean connection strengths for all regions is provided in Fig.6.5a.

Several main features regarding the temporal evolution of the default networks can be derived from Figs. 6.3 and 6.4. First, the connection percentage starts from 66.7% (10/15: 10 significant connections out of 15 possible ones) in neonates, increases to 91.03% (71/78) in 1yr olds, levels off to 78.4% (134/171) in 2yr olds and increases to 100% in adults, suggesting a non-linear evolution pattern of the connectivity of the default network. Second, as mentioned previously, the pediatric default networks include regions that are consistent with the adult group as well as additional regions not observed in adults. Interestingly, with the exception of LTC, the former regions are typically located near the center of the graph while the latter regions are located a distance away from the center in all pediatric groups. This finding implies that the regions consistent with those observed in adults are more strongly connected when compared with those not observed in adults. The only exception of the observed weak connection, LTC, appears consistent with that reported by Buckner et al (28). Third, for pediatric groups, both PCC/Rsp and MPFC are consistently located at the center of each graph with the exception of the neonate group (only PCC/Rsp), implying that these two regions are most strongly connected with other regions. This finding is consistent with the degree of connection plots (Fig. 6.4b) – the ratio of the number of connections a specific region possesses to the total possible connections. Fourth, regarding the mean connection strength – a measure previously suggested to be positively correlated with functional performance

(172), the PCC/Rsp and MPFC reliably exhibit the highest mean connection strengths across all ages while the brain regions located at a distance away from the center regions are unexceptionally ranked with lower values (Fig. 6.5). Finally, a regression analysis reveals that the connection strength between these two regions is linearly (P=0.0059) increased as a function of age (Fig. 6.5b), although one must be cautious that there is a large age gap from 2yr olds to adults.

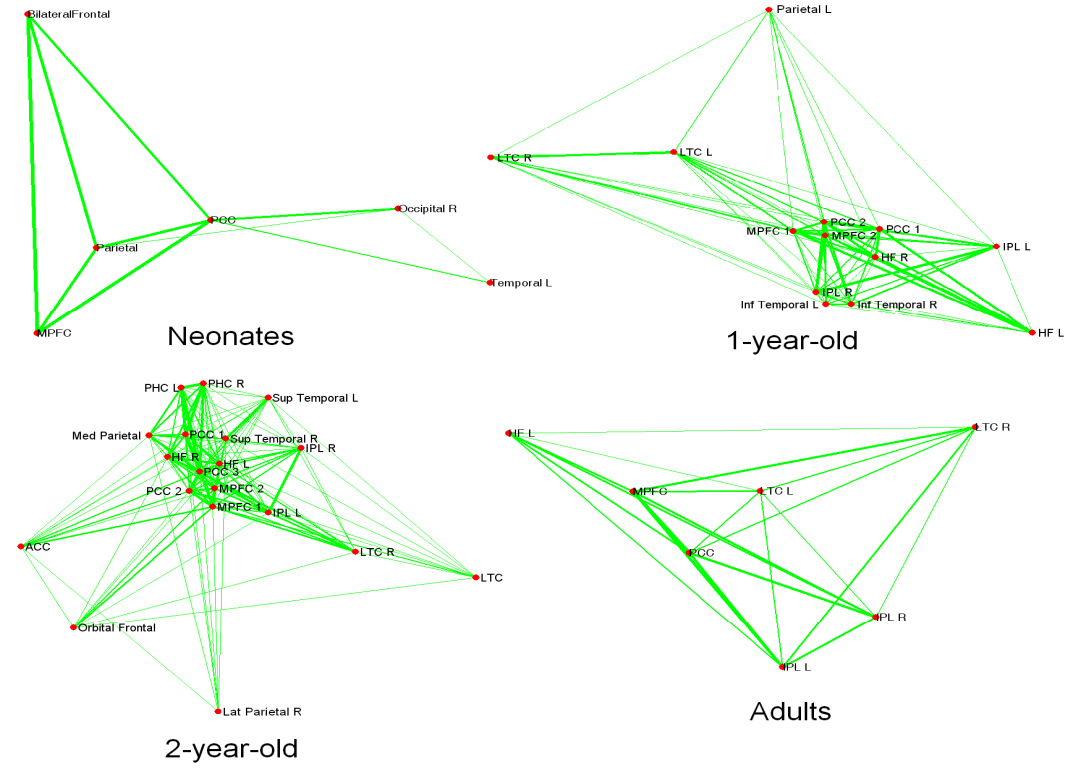

(a) Functional connectivity graph

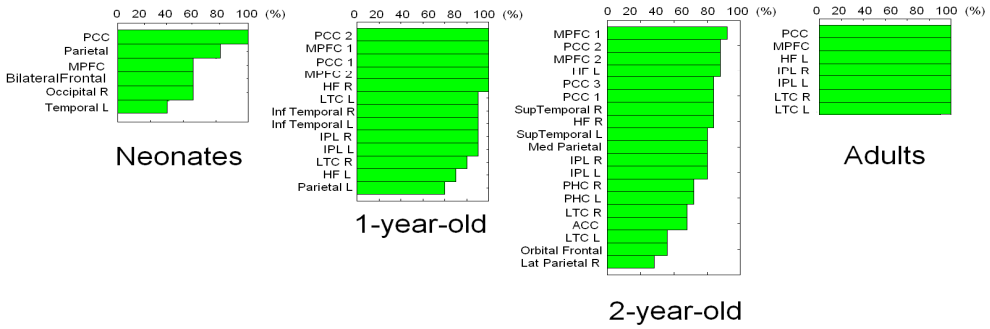

(b) Degree plot

Figure 6.4 (a) Functional connectivity graphs for all four age groups. The most strongly connected regions are clustered near each other while weakly correlated regions are placed further away from each other. The width of the line between two nodes is proportional to the corresponding connection strength. Only significant correlations ($P<0.05$) were plotted. (b) Bar plots of the degree of connection for each node in a descending order (the ratio of the number of connections a specific region possesses to the total possible connections). See Fig.6.3 for abbreviations.

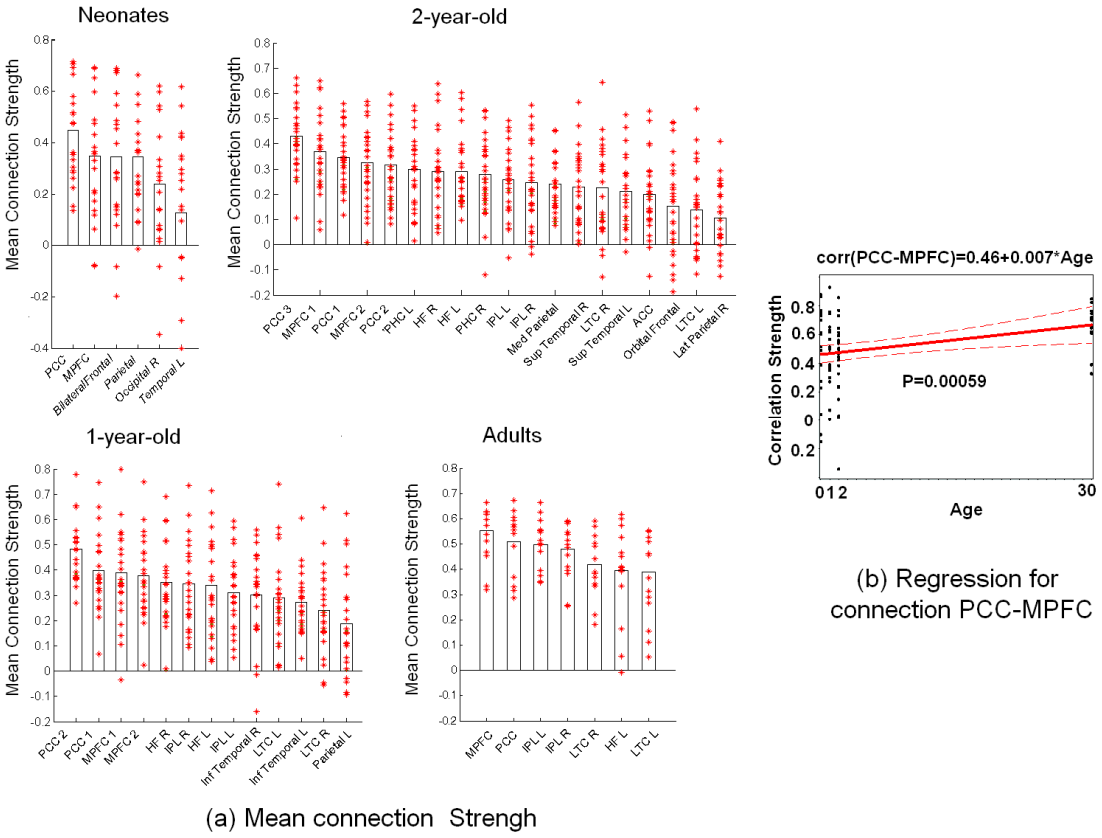

Figure 6.5 (a) Mean connection strength of each node for all age groups. The bars indicate the mean connection strength averaged over the corresponding group and red

asterisks represent the values of individual subjects. (b) Regression results for the connection between MPFC and PCC. See Fig.16 for abbreviations.

Thus far, our findings consistently indicate that the PCC/Rsp and MPFC may play a critical role in the default network. The notion of the presence of hub regions in the brain has been proposed (42). Therefore, to further determine whether or not the PCC/Rsp and MPFC are the two potential hubs in the pediatric default networks, the betweenness centrality (BC) (173) – a measure of node importance in graph theory, was calculated for each region based on the individual network within each age group (Fig. 6.6). As evident in Fig. 6.6, the most elevated centrality measure for all age groups is the PCC/Rsp. In addition, although smaller than the PCC/Rsp, the MPFC in 1yr and 2yr olds also exhibit elevated centrality measures when compared with the remaining regions. These results suggest that the PCC/Rsp may be the major hub of the default network whereas the MPFC subsequently emerges, potentially, as the secondary hub starting at 1yr of age.

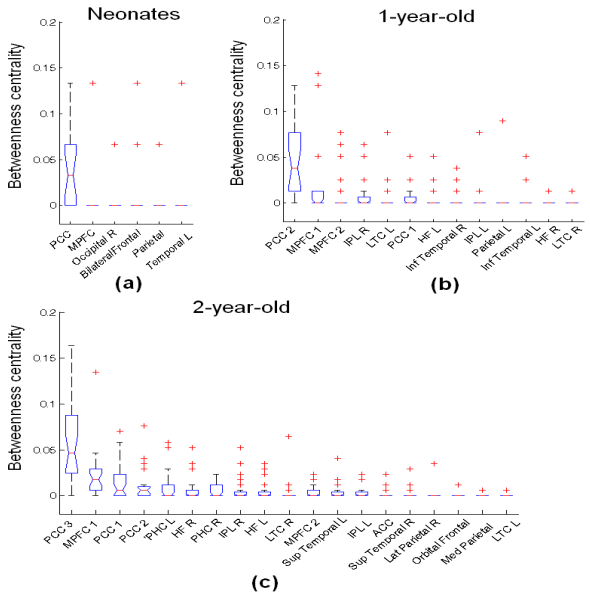

Figure 6.6 Betweenness centrality measures for individual ROIs of the three pediatric groups. (a) neonates; (b) 1-year-old; and (c) 2-year-old. See Fig.16 for abbreviations.

6.4 Discussion

The temporal evolution of the default network during a critical time period when brain dynamically establishes axonal connections to form different networks and also undergoes extensive axonal pruning was investigated in this study. With the rfcMRI approach (20) and full-term healthy normal pediatric subjects ranging from 2wks to 2yrs of age, group ICA revealed the anatomical representations of the default network. Specifically, a primitive and incomplete default network was observed in neonates (Table 6.1). This observation is consistent with that reported by Fransson et al where they also failed to detect "a direct equivalent of a default-mode network in infant brain" (162). The default network at 1yr-old became more complex and was intensively connected among different brain regions (91.03%), indicating the formation of a well synchronized default network at this age. In contrast, the changes of the default network from 1yr- to 2yr-olds were more subtle, particularly considering those regions that are commonly observed in the adult's default network. All of the regions presented in 1yr olds persist in 2yr olds with the addition of PHC, making the architecture of the whole network more complete (26, 28). To the best of our knowledge, these are the first reported results, demonstrating the temporal and spatial development of the default network in such a critical age period of normal brain development.

One of the major findings of our study is the notion that both PCC/Rsp and MFPC may play a critical role in the default network. Both PCC/Rsp and MPFC are consistently observed in all ages (Fig. 6.2 and 6.3), exhibit the largest volume ratios (Table 6.1), are

located at the center of each network (Fig. 6.4), and have the largest mean connection strengths (Fig. 6.5). Indeed, the centrality measures revealed that the PCC/Rsp may serve as the main hub while the MPFC is the secondary hub which starts to emerge at 1yr of age (Fig. 6.6). This finding is intriguing and appears consistent with that reported in adult studies: it has been suggested that the MPFC and PCC/Rsp are the two hubs involved in different aspects of cognitive function in adults (161). Specifically, MPFC has been implicated to be more involved in self-referential activity, mentalizing process, self-projection or theory of mind (155, 174-176) whereas the PCC/Rsp is more associated with episodic memory retrieval (177). However, translating these functions of MPFC and PCC/Rsp in adults to pediatric subjects is elusive. In addition, since independent behavioral measures were not available in our study, the observed temporal and spatial development of the default network cannot directly translate to functional development. Nevertheless, some similarities are observed between our findings and the reported functional development in the literature. Amsterdam (120) found that infants from 6 through 12 months of age demonstrate prolonged and repeated reaction to their mirror images as a sociable playmate. Wariness, withdrawal, self-admiring and embarrassed behaviors start at 14 months and have been observed in 75% of the children after 20 months of age. From 20 to 24 months of age, the majority of subjects demonstrate recognition of their mirror images. These temporal behaviors demonstrate an evolving trajectory of self-consciousness before the age of two, which is essential for self-projection/self-referential activity. Studies on toddlers also revealed that 18- to 24-month-olds are able to use speaker's gaze direction (121) and affective expression (122) as cues leading to speaker's communicative purposes. Akhtar and Tomasello (124) further

proposed that children are able to infer the meaning of words through an understanding of people's minds (125). These primitive mental functions may actually act as a promising source where more sophisticated function such as mentalizing about others and "theory of mind" can be originated and developed. Together, these findings suggest that the functions associated with MPFC regions undergo gradual development during the first years of life, which is in line with our findings: MPFC emerges as one of the hubs of the default network from 1yr olds.

In contrast to MPFC, the PCC/Rsp is associated with episodic memory retrieval in adult studies. Therefore, the question is whether or not the observed PCC/Rsp in our study reflects the primitive version of memory in very young children. The appearance of the right occipital region and the bilateral posterior parietal/occipital area encompassing the PCC (termed simply as PCC in the text) in neonates may suggest the formation of some forms of memory (i.e., implicit memory). Consistent with these findings, Davidson (115) suggested that implicit memory is robustly presented in neonates and toddlers. Additional studies further demonstrated that the sensorimotor experiences of the fetus (116) and the voice of mother (117) can be memorized. In contrast, the emergence of bilateral HF, bilateral IPL and PCC/Rsp starting from 1yr olds to 2yr olds forms a hippocampal-parietal memory network much like that defined by Vincent et al (32) in adults. In line with our findings, Fivush and Hamond (118) showed that 2yr olds can already retrieve much detail about a trip to the zoo. Together, our findings of the PCC/Rsp appear to be consistent with that reported in the literature and demonstrate a memory-related architecture in 1 and 2yr olds.

Despite the possible default-network related functions discussed above and the observed adult-like architecture of the default network in 1 and 2yr old groups, one must be cautious in further interpreting our results since it is highly unlikely that such young pediatric subjects may have the brain circuitry capable of adult-like default network functions. It has been suggested that the "theory of mind" emerges after age of 3 and episodic memory are not formed until the age of 4 (119). Therefore, although we observed a complete architecture of the default network in 1yr olds, its related function remains largely unknown. These apparent discrepancies led us to hypothesize that the formation of the default network may predate its functional specialization. Although not specifically focusing on the default network, Johnson et al also claimed that cognitive functions of infants often employ both larger area of cortex and also a wider range of interactions of brain regions that include and extend beyond those used in adults (108). While to directly prove or disprove this hypothesis for default network is beyond the scope of our study, our results may offer preliminary evidence of support in three different ways. First, the decreasing volume ratios of PCC/Rsp and MPFC with age indicate the ongoing localization of these major regions. Second, in addition to those brain regions that are consistently observed in adults, extra brain regions in pediatric groups' default networks are also observed. Finally, the connection percentage first increases from 67% in neonates to more than 90% in 1yr olds and then decreases to 78% in 2yr olds. The latter two findings suggest a potential specialization process of removing redundant connections. Nevertheless, more results, particularly beyond 2yrs of age will be needed to further determine the temporal relation between the presence of connectivity and functional development. Toward this end, Fair et al (101) recently investigated the

development of default network on school-age children based on an ROI seeding approach. They found an incomplete default network with much sparser and weaker connections in children when compared with adults. Considering our findings of the disappearance of extra regions and reduction of percent connections from 1yr to 2ry olds, it is plausible that this reduction trend continues till the age span in their study. Nevertheless, one should note that this trend of reduction at some point need to be reversed to be consistent with the adults' results reported here and in the literature (28), suggesting a potential bi-phasic instead of monotonic behavior of the development of the default network. Systematic studies covering the whole age span from neonates, school age children to adults are necessary to further investigate the temporal evolution of the default network.

Two different approaches are commonly employed to discern brain functional connectivity, namely ROI and ICA (22, 101). Both approaches have its pros and cons. The ROI approach requires a priori information to place the ROIs, typically employing activated regions in task related studies. It allows direct comparisons between groups if the ROIs are identical among groups. It also offers a higher sensitivity if a ROI instead of a seed voxel was chosen for temporal correlation analysis. However, this approach is somewhat biased and may not be able to identify new connections. In our study, using regions of the adult's default network as a priori could limit our ability to determine the temporal and spatial evolution of this network in pediatric subjects. Therefore, the ICA approach is adopted in our study. However, one of the difficulties associated with ICA is how to objectively determine which component(s) links to the default network. To partially circumvent this difficulty, an automated template matching approach (169) was

employed here to identify components comprising the default network. Although not completely eliminating the subjective nature of selecting components, this approach allows a more consistent means to determine ICA components and offers the ability to explore temporal and spatial evolution of the default networks in the developing brain. With the template matching procedure (169), we have identified 3, 2, and 2 "best fitted" components for neonates, 1yr olds and 2yr olds, respectively. As is always the case with the ICA approach, those components not selected for visualization/analysis may correspond to other functional networks. However, we feel this exclusion is justified since the main focus of our study is the development of the default network.

Finally, two additional technical issues warrant further discussion. First, since all of the subjects were sleeping during imaging acquisition, it is plausible that different depths of sleep from subject to subject may result in experimental variability. Nevertheless, it has been reported that resting functional connectivity appears to be independent of whether or not the subjects were at sleep, awake or even under anesthesia (91). Therefore, we do not foresee that different depths of sleep would affect the outcomes of our studies. Second, the rather low spatial resolution has limited our ability to discern small cortical structures for the default network. Specifically, Buckner et al (28) have separately evaluated the dorsal and ventral MPFC of the default network. This is not done in our study owing to the limited spatial resolution, which reflects a compromise between the quality of rfcMRI and the data acquisition time for imaging non-sedated subjects.

6.5 Conclusions

With rfcMRI, we report the temporal and spatial evaluation of the default network in healthy normal pediatric subjects between 2wks and 2-yrs of age. A primitive and incomplete default network is observed in 2wk olds, followed by a marked increase in the number of brain regions exhibiting functional connectivity and the percent of functional connection at 1yr olds, and finally becoming a similar network as that reported in adults at 2yr olds. In addition, although the default network changes substantially among different age groups, PCC/Rsp is consistently observed in all age groups, among the most and strongest connections, and the highest centrality measure of the pediatric default networks, suggesting that PCC/Rsp is the main hub of the default network. In addition, although not as remarkable as the PCC/Rsp, the MPFC emerges as a potential secondary hub of the pediatric default networks starting from 1yr of age. To the best of our knowledge, these are the first reported results on the temporal development of the default network in a critical time period of brain development.

Table 6.1: Anatomical regions of the default network in neonates, 1yr olds, 2yr olds, and adults

Adults				**Neonates**			
	Region	**Volume Fraction**	**Mean Z score**		**Region**	**Volume Fraction**	**Mean Z score**
IC 1	MPFC	0.0402	2.32	**IC 1**	MPFC	0.1287	3.65
	PCC	0.0183	3.21		Occipital R	0.0167	1.50
	HF L	0.0015	1.36		Parietal	0.0248	2.37
	LTC R	0.0016	1.43		Temporal L	0.0066	1.45
	LTC L	0.0021	1.58	**IC 2**	PCC	0.1183	4.39

	IPL R	0.0067	2.07	**IC 3**	Bilateral Frontal	0.1271	3.57
	IPL L	0.0097	2.38				
	1-year-old				**2-year-old**		
IC 1	MPFC 1	0.0428	2.87		MPFC 1	0.0562	2.58
	HF R	0.0059	1.91		HF R	0.0041	1.56
	HF L	0.0076	1.85		HF L	0.0043	1.39
	LTC R	0.0032	1.52		LTC R	0.0012	1.23
	LTC L	0.0034	1.42		LTC L	0.0023	1.25
	PCC 1	0.0048	1.57		PHC R	0.0007	1.48
IC 2	MPFC 2	0.0063	1.61		PHC L	0.0011	1.24
	Inf Temporal R	0.0013	1.46		PCC 1	0.0084	1.68
	Inf Temporal L	0.0022	1.38		SupTemporal R	0.0045	1.63
	PCC 2	0.0588	3.03		SupTemporal L	0.0027	1.44
	IPL R	0.0057	1.27		ACC	0.0016	1.48
	IPL L	0.0009	1.08		PCC 2	0.0056	1.59
	Mid Front L	0.0013	1.18		Med Parietal	0.0037	1.43
				IC 1	Lat Parietal R	0.0012	1.25
				IC 2	PCC 3	0.0550	3.07

					IPL R	0.0105	1.48
					IPL L	0.0096	1.36
					MPFC 2	0.0050	1.49
					Orbital Frontal	0.0037	1.40

Chapter 7

Evidence on the Mediating Role of Frontal Parietal System on the Anti-correlated Default and Dorsal Attention System

The previously discussed default network has been considered as a task negative network since it appears to be highly active during a resting condition (26). This is in an obvious contrast with more well known networks which are active during the performance of cognitive tasks, task positive networks (178). It has been demonstrated by several studies that anti-correlation between these two systems exists which may indicate one of the brain's intrinsic organization principles (23). In this Chapter, this anti-correlated phenomenon will be specifically tackled and the hypothesis of the potential mediating role of the frontal-parietal control system on this anti-correlation will be directly tested, aiming to answer the important question regarding the relationship between these three most salient networks during resting state as well as task sates (23, 88). Moreover, as the network organization is increasingly accepted in the neuroscience field, there is also increasing need to design a network-level approach to specifically quantify the interaction strength between different brain systems. One such newly developed method as well as the findings regarding the proposed hypothesis using this approach will also be described in the final section of this chapter.

Given that this mediating relationship is an unvalidated hypothesis, we started to first prove its validity in adult subjects based on matured brain functional structure to lay down the basis for following developmental studies. The question of when this mediating role emerges and how it develops during the first few years of life will be specifically tackled in future work.

7.1 Introduction

Normal brain functioning relies on coordinated activity among sets of distributed yet interacting brain regions, essentially forming networks responsible for distinct functions. Among them, two "competing" systems, either increasing or decreasing activity depending on the presence or absence of attention-demanding tasks were extensively studied (26, 154, 178). The first is the dorsal attention system (DAS) covering regions in the frontal eye fields (FEF), intraparietal sulcus (IPS) and middle temporal area (MT+), which are routinely activated during performance of goal-directed tasks (178). The roles of DAS have been well documented and are associated with externally directed cognition including spatial attention, motion tracking, initiating and maintaining activity while awaiting a target, etc (178). The second system comprises the so called "default-mode" network, including posterior cingulate cortex (PCC), inferior parietal lobule (IPL), medial prefrontal cortex (MPFC) and medial temporal regions encompassing bilateral hippocampus formation (HF). As mentioned previously, the default network commonly exhibits a decreased activity during attention-demanding tasks (26, 154). Although there is a general consensus that this system is related to internally directed cognition, its exact functions are poorly defined largely due to the "unconstrained" nature of "resting" state from which this network is defined. However,

given that numerous studies have reported activation of PCC and IPL (179-182) during memory-retrieval tasks and the involvement of HF regions in this system, it is highly likely that memory-related function is one of its key responsibilities (28, 32). Recent identification of a "hippocampal-parietal" memory network exhibiting almost identical anatomical regions with this network further reinforces this notion (32). In addition, the potential self-referential, mentalizing, and planning functions of the MPF regions further make this system suitable for recollecting the past and thinking about the future (21, 28, 155).

Recent functional connectivity magnetic resonance imaging (fcMRI) studies reveal that the regions within each of the two systems are highly positively correlated during resting state (23, 88, 91), reinforcing the notion that regions similarly modulated during tasks tend to exhibit synchronized activity even in the absence of tasks, consistent with Biswal et al's (20) first observation of this phenomena. On the other hand, given the clear functional disassociation between these two "competing" systems as previously described, the activity between them should be disassociated. Indeed, studies did find "anti-correlated" activity between these two systems during the resting state (23). Moreover, Kelly et al (97) demonstrated that the strength of this "anti-correlation" is modulated by exogenous demands under continuous task performance and its strength is positively related with task performance, underscoring the behavioral significance of this anti-correlation.

Do these two systems exhibit such opposing activity on their own or is there another system(s) that potentially "mediates" between these two systems or even regulates their activity? During sustained brain states that primarily involve one of the

systems, e.g, the “work on their own” hypothesis seems to work simply indicating that during at a certain state the system supporting “task (unconstrained thinking as a “default task” during resting)” performance will increase activity while the other system supporting irrelevant processes will decrease activity. However, our own experience suggest that the brain can readily alternate between such anti-posed states, i.e., the “activated” system can immediately become “suppressed” and vice versa when external stimuli or internal decisions required to do so seem to argue against the “on their own” hypothesis and strongly support that the brain has another resort to take into consideration of either the external stimuli or internal decision and in turn reconcile/regulate the activity of these two opposing systems to fulfill the need. Indeed, Vincent and colleagues (88) have looked into this issue and revealed that a “frontal parietal control system (FPC)” encompassing anterior prefrontal cortex (aPFC), dorsal lateral prefrontal cortex (dlPFC), anterior cingulate cortex (ACC), insula (INS) and anterior inferior parietal lobule (aIPL) is “anatomically positioned to integrate information from these two opposing brain systems”. In support of this, Sridharan et al (183) have shown that several major nodes within this system including rINS and ACC, exert significant causal influence to several key nodes within both the default network and another “central-excutive (CEN)” network, strongly supporting the potential mediating role of FPC.

However, although the default network is involved in Sridharan et al’s study (183), their CEN network, which includes dlPFC and posterior parietal cortex (PPC), is largely different from the dorsal attention network. Thus, the primary goal of this study is to test the hypothesis that regions within FPC mediate the anti-correlated activity of the

dorsal attention and default systems. Two lines of evidence will support this hypothesis. First, for mediation/regulation to be true across different brain states, FPC should selectively increase/suppress the activity of either network to facilitate task performance depending on whether the task is external-attention directed (more related with DAS) or internal cognitive function oriented (more related with DS). Secondly, during stable states, for mediation to be true, removing the effect of FPC should result in significantly poorer anti-correlation between these two systems during any sustained state.

We directly tested the above two hypotheses using functional connectivity measures based on BOLD fluctuations. Specifically, two task states, namely continuous finger tapping (FT) and movie watching (MW), were selected to compare with the resting state (RS). The two tasks were designed to engage primarily one of the two opposing systems, respectively, i.e. FT for dorsal attention system and MW for default system (besides the obvious motor and visual involvement). To do this, subjects were specially instructed to tap their thumb against each of the four other fingers in a sequential manner during FT with a frequency of around 1Hz to maintain attentional focus. In contrast, subjects were told to report the contents of the movie segment after the experiment to engage memory-related function during the process. Visual monitoring during FT found good compliance with the instruction and post-experiment questionnaire showed moderate to high level of memory of the movie contents even a year after the experiment (Table.7.1), validating our study design. Hence we hypothesized that if FPC truly exerts mediation between the two competing systems for the performance of the specific tasks, it will increase connectivity with DAS and decrease connectivity with the default during the FT task while the opposite should be true for MW task. Secondly, if this mediation is

sustained during any ongoing brain states, then "removing" its effect (through the concept of partial correlation) should result in significantly reduced anti-correlation between DAS and default network during each of the examined states. In addition, in this project, we also aimed to design a multivariate approach to explore the network-level interactions and the results will be combined with those from traditional regional techniques to test the proposed hypothesis.

7.2 Methods

7.2.1 MR Acquisition

A total of 19 healthy subjects (age 25~33, 7F, all right-handed) were recruited in this study. Informed consent was obtained from all participants and the experimental protocols were approved by the institutional review board. All images were acquired using a Siemens Allegra 3T MR scanner (Siemens Medical Inc., Erlangen, Germany). Anatomical images were acquired using a 3D MP-RAGE sequence and these images were subsequently used for co-registration among subjects. The imaging parameters were as follows: repetition time (TR) = 1820ms (sum of the inversion time and the duration of the entire 3D partition encodings for one phase encoding step); echo time (TE) = 4.38 ms; inversion time = 1100ms; 144 slices; and voxel size = 1x1x1mm3. For the rfcMRI studies, a T2*-weighted echo-planar imaging (EPI) sequence was used with the following imaging parameters: TR = 2sec, TE = 32 ms; 33 slices; and voxel size = 4x4x4 mm3. This sequence was repeated 150 times (~5 min) for each experimental condition, including resting, continuous finger tapping and watching a movie clip. During the resting state, subjects were instructed to relax and remain still but keep eyes closed. During the finger tapping condition, subjects were instructed to lie still with eyes closed

while continuously touching the thumb to each finger in a sequential manner using only the dominant hand. In addition, subjects were also instructed to maintain a consistent pace (~1Hz) of finger tapping throughout the entire scan. Each subject was visually monitored during the scan. For the movie watching task, the movie clip contain shallow sea scenes with a variety of animal activities. Subjects were told to report what they saw in the movie after the experiment and a questionnaire was filled by each subject 1 year after the study and most of them reported moderate to high memory scores suggesting strong memory function involvement during the task (Table 7.1).

Table.7.1 Reported scores indicating the level of memory of the movie contents. 0-10: with 0 indicating no memory at all and 10 perfect memory of every detail. Scores of the 16 subjects involved in analysis are reported.

Sub_1	5	Sub_2	5.5	Sub_3	2.5	Sub_4	6
Sub_5	2.5	Sub_6	5	Sub_7	2	Sub_8	4
Sub_9	3	Sub_10	4	Sub_11	7	Sub_12	5
Sub_13	3	Sub_14	5	Sub_15	6	Sub_16	4
Mean:	**4.34**	**SD:**	**1.45**				

7.2.2 Preprocessing

The brain extraction tool of the FSL (FMRIB, Oxford University, U.K.) was first applied to exclude voxels outside of the brain. Subsequently, rfcMRI data went through several preprocessing steps including compensating slice-dependent time shifts, rigid body correction for inter-volume movement, and spatial smoothing (6-mm full width at half maximum Gaussian kernel). Nuisance sources of variance (white matter, CSF and the mean global signal) were removed using regression technique. Three subjects were excluded from the subsequent analysis because of excessive head motion during the scan.

For the remaining 16 subjects, images of the first ten time points were excluded to allow magnetization reaching a steady state. The first available set of rfcMRI images was co-registered to the corresponding T1-weighted MP-RAGE structural images using affine rigid body alignment. T1-weighted structural images were then spatially normalized with the Montreal Neurological Institute (MNI) EPI template using intensity-based HAMMER nonlinear registration (164). The transformation fields from affine alignment and HAMMER registration were employed to normalize rfcMRI volume data from all subjects to the template space, allowing group analysis of rfcMRI.

7.2.3 Functional network definition

A total of five functional networks were defined in our study, including the default, dorsal attention (DA), frontal parietal control (FPC), motor-sensory and visual networks. All of these networks were constructed based on the published MNI coordinates of the major regions within each network (88) (Table.7.2). For each coordinate, a sphere with a size of ~2cm^3 was defined around the predefined center to define an ROI. Overall, there are 6, 9, 6, 6, and 5 nodes within the DA, default, FPC, V and MS networks (altogether 32 nodes), respectively.

7.2.4 Network analysis

The defined ROIs within each network were used throughout the subsequent analysis and the mean time course was extracted from each ROI to construct a 32*32 correlation matrix for each subject. After fisher-Z transform and averaging across group, mean matrices were obtained for each of the three examined states, which were then used to test the across-state differences. Specifically, for between-network comparison, interactions among region pairs from any two networks (one from each) were

concatenated to form a vector and compared across states (resting vs finger tapping; and resting vs movie watching) using nonparametric krusk-wallis test. FDR (170) method was used to correct for multiple comparisons and significant between-network was defined as $p<0.05$ after correction. The same procedure was also done for all within-network comparisons.

Table.7.2 MNI coordinates of regions of interest within five predefined networks

Dorsal Attention (DA)	lMT+: (-45, -69, -2) rMT+: (50, -69, -3) lIPS: (-27, -52, 57) rIPS: (24, -56, 55) lFEF: (-25, -8, -50) rFEF: (27, -8, -50)	**Visual (V)**	lCal: (-8, -72, 4) rCal: (16, -67, 5) lCS: (-5, -96, 12) rCS: (18, -96, 12) lLO: (-23, -89, 12); rLO: (37, -85, 13);
Frontal Parietal Control (FPC)	laPFC: (-36, 57, 9) raPFC: (34, 52, 10) ACC: (3, 31, 27) laIPL: (-52, -49, 47) raIPL: (52, -46, 46) ldlPFC: (-50, 20, 34) rdlPFC: (46, 14, 43) lINS: (-31, 21, -1) rINS: (31, 22, -2)	**Motor-Sensory (MS)**	lPreC: (-41, -4, 54) rPreC: (42, -13, 53) lPoC: (-45, -26, 54) rPoC: (49, -27, 53) SMA: (6, -5, 54)
Default	lHF: (-21, -15, -14) rHF: (24, -19, -21) vmPFC: (0, 51, -7) PCC: (1, -55, 17) lpIPL: (-47, -71, 29) rpIPL: (50, -64, 27)		

To test the mediation effect of FPC on the two opposing systems: DA and default, partial correlation analysis was performed. Specifically, for each subject, partial correlations between pairs of regions within the two systems (one from each) are calculated by regressing out the effect of all signals within FPC. After fisher-Z transform of both the original correlation values and the partial correlation values, the differences were then taken and averaged across different pairs of regions as an indicator of the mediating effect from FPC for that subject. As a result, for each sustained state, we have a N*1 vector (N: number of subjects) quantifying the mediation effect of FPC on the two opposing systems. This procedure is repeated by using MS and V as regressor networks

to calculate the mediating effects from these two reference networks. Finally, statistical comparison between the mediating effect across different networks as well as the same network across different states was done using the same nonparametric kruskwallis test.

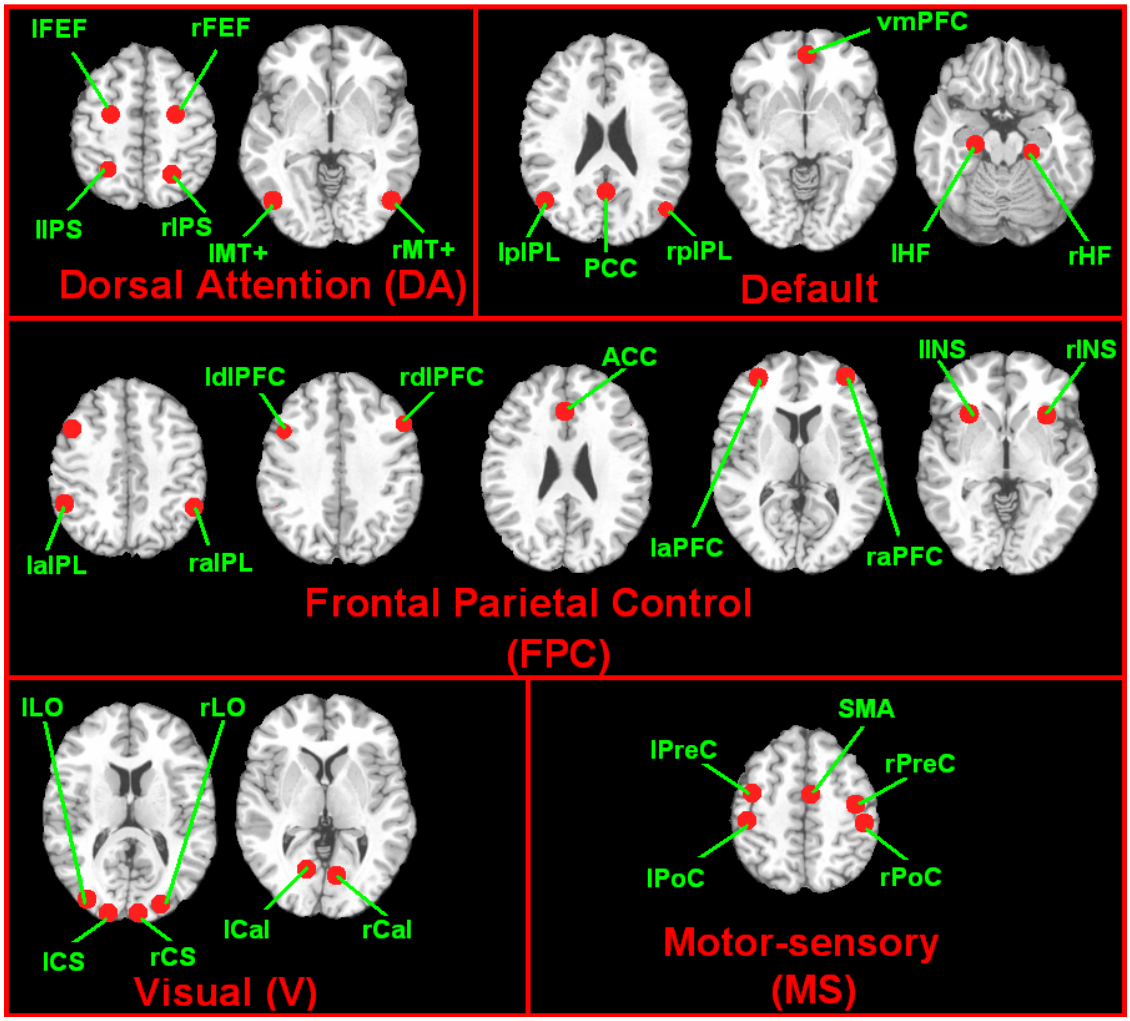

Figure 7.1 ROI selections for five predefined networks.

7.3 Results

To explore the relationship between DAS, default and FPC, corresponding networks were constructed based on published coordinates of ROIs withing each network

(Fig.7.1) (88). Specifically, DAS was constructed to include nodes within bilateral IPS, FEF and MT+; default within PCC, MPFC, bilateral posterior IPL (pIPL) and HF; and FPC within anterior cingualte cortex (ACC), bilateral aPFC, dorsolateral prefrontal cortex (dlPFC), anterior insula (aINS), and anterior inferior parietal lobule (aIPL). In addition, given the apparent involvement of the motor-sensory (MS) and visual system (V) during either of the two tasks, the corresponding networks were defined to include nodes centered on bilateral precentral gyrus (PreC), postcentral gyrus (PoC), supplementary motor-sensory cortex (SMA) and bilateral calcarine (Cal), cuneus (CS), and lateral occipital (LO), respectively.

To test the first hypothesis, regional correlation matrices were constructed for each individual subject respectively using the BOLD fluctuations obtained during each of the three examined states (RS, FT and MW). Individual matrices were then fisher-Z transformed and averaged to get a group mean correlation matrix for each of the three test states. A two-tailed t test was conducted to test the significance of each connection at the level of p=0.05 after correcting for multiple comparisons using FDR (170).

The resulting significant correlation matrix for RS and FT states are presented in Fig.7.2. It is immediately clear that during resting state, regions within every network are highly synchronized (85.7% significant, within black boxes) consistent with most previous findings indicating high interaction between functionally similar regions (22-24, 48, 157), but the connections between networks are much sparser (12.8% significant) implying great functional disassociation between different systems. However, during FT, although the within-network interaction pattern remains qualitatively similar, the between-network interaction pattern dramatically changes (Fig.7.2). To find out the

significant changes at network level between the two states, for each pair of networks, the vector of corresponding mean interaction values obtained during RS and FT was compared using nonparametric one way ANOVA and significant changes were defined at p=0.05 level after FDR correction (170). Six pairs of networks significantly changed their interactions at network level including DA-MS, DA-DF, FPC-DA, FPC-DF, FPC-MS, and V-MS, the results are shown in the bottom row of Fig.7.2. Note the same network-level comparison was done for each within-network connection vector but no significant changes were detected.

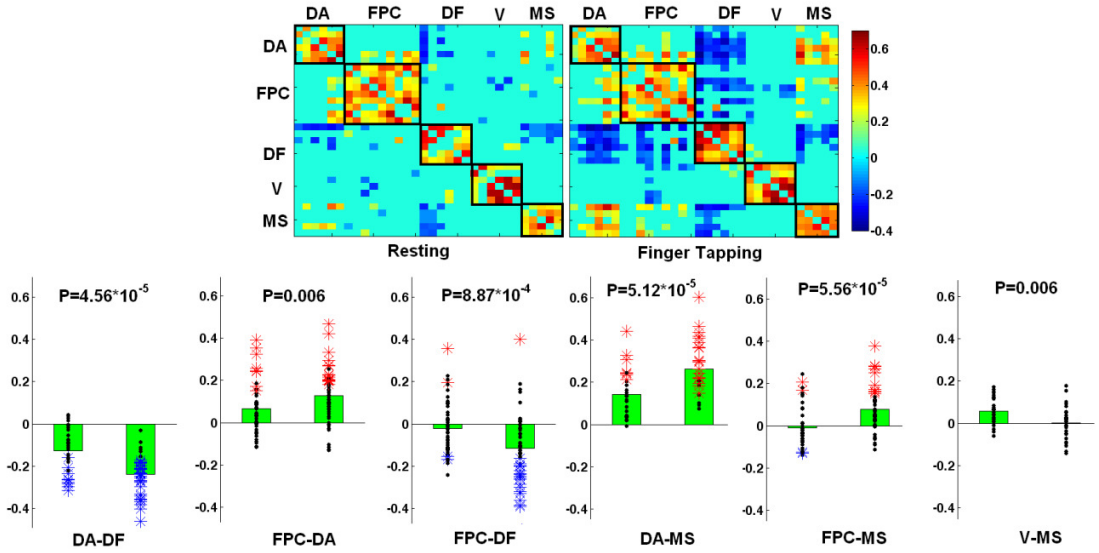

Figure 7.2 The between-network interaction changes during finger tapping (FT). Top row: the significant correlation map during the two states; Bottom row: significant between-network interaction changes. Within each comparasion, the bar to the left is during resting state and the one on the right is during finger tapping.

As shown in Fig.7.2, interaction between DA and the actual "task performer"-the MS significantly increased (p=0.0000512) reflecting the increased attentional control

during the task, which is expected. Moreover, DA and DF becomes significantly more anti-correlated ($p=0.0000456$), which is consistent with previous reporting of increased anti-correlation during attention demanding tasks (97). However, most intriguing results come from the interaction changes associated with FPC and the two opposing systems: it significantly increases connection strength with DA system ($p=0.006$) while significantly decreasing connection strength with DF system ($p=0.00087$), which is exactly as hypothesized, strongly indicating its role in regulating the activity of both DA and DF to achieve the task goal. In support to this role, FPC is also observed to increase direct interaction with MS ($p=0.0000556$, Fig.7.2). Besides, although none of the regional interactions reaches statistical significance during either state, the interaction between MS and V at network level get significantly disrupted during FT ($p=0.006$).

As the FT task validates the hypothesis that FPC will increase DAS activity (more positively correlated) while "suppressing" default activity (more anti-correlated) during attention demanding tasks, we move on to the next task which is assumed to be more related to the default network activity due to apparent memory function involvement. An dentical procedure was implemented to compare between RS and MW states and the results are shown in Fig.7.3. While the pattern of minimal within-network changes but dramatic between-network changes still hold for this state, the significant changes associated with between network interactions is largely different, which include FPC-DA, FPC-DF, and DA-V. From Fig.7.3, it is apparent that FPC largely reverses its positive interaction pattern with DAS and becomes predominantly negatively correlated during MW ($p<0.00001$) while at the same time it enhances its positive correlation with default ($p=0.0034$), which is again highly consistent with our hypothesis. Besides these changes,

the interaction between DA and V significantly increases (p=0.000441), likely reflecting certain level of attentional budget during the task performance. Note also in this state, although DA and DF seem to be more anti-correlated comparing with resting, this change does not reach statistical significance.

To further test the hypothesis that FPC mediates the anti-correlation during each stable brain states, we used the partial correlation technique, which perfectly suits our purpose since it is defined as the correlation between two variables after regressing out the effect of another set of variables. To do this, we calculated the partial correlation between each pair of regions across DAS and default (one from each) by regressing out signals within FPC network and the resulting between network correlation strengths were compared against those from ordinary correlation using nonparametric one way ANOVA to test significant differences. Besides, reference results were obtained by repeating the same procedure but using MS and V network as corresponding repressor.

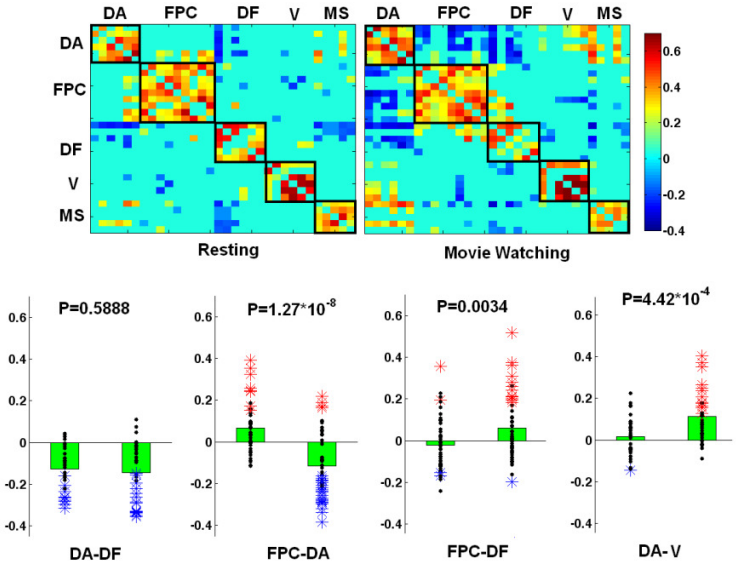

Figure 7.3 The between-network interaction changes during movie watching (MW). Top row: the significant correlation map during the two states; Bottom row: significant

between-network interaction changes. Within each comparasion, the bar to the left is during resting state and the one on the right is during movie watching.

Results from all three states are presented in Fig.7.4 where we can observe that the effect of FPC on the anti-correlation between DAS and default is apparent: the "removal" of FPC effect results in significant reduction of the anti-correlation for all three brain states (RS: $p=0.0005$; FT: $p<10^{-10}$; MW: $p=0.0078$). Moreover, its effect is significantly stronger than that of V for all three states. Actually, V failed to show any significant mediation effect for any states. In addition, during resting state, FPC is the only network that shows significant mediation effect on this anti-correlation. During both finger tapping and movie watching, MS also shows significant mediation effect, but it is significantly weaker than that of FPC during FT while comparable to that of FPC during MW. Finally, comparing FPC's mediation effect across the three states reveals that it is during finger tapping that FPC demonstrates the strongest mediation effect (RS vs FT: $p<10^{-5}$; MV vs FT: $p=0.0000414$).

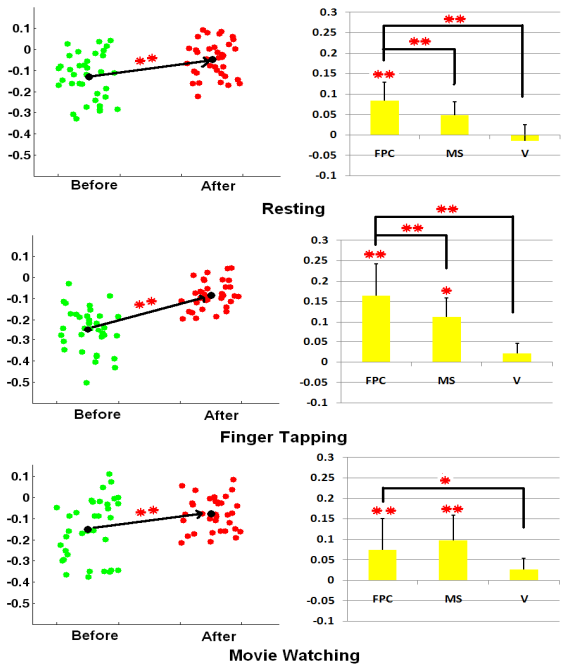

Figure7.4 The mediation effects of FPC on the interaction between DA and DF. Left column: the effect of removing FPC effects on the interaction between DA and DF; Right column: the comparison of mediating effects of FPC, MS and V on the interaction between DA and DF.

7.4 Discussion

Our results show two lines of evidence on the mediating role of the frontal parietal system (FPC) between the anti-correlated default and dorsal attention system (DAS). Across different task states, the two opposing systems are differentially regulated by FPC to facilitate task performance, depending on the "affinity" of the task to either system. During stable states, the anti-correlation is largely mediated by FPC, especially during the resting state, our results show that this anti-correlation is largely and exclusively mediated by FPC.

Although the cognitive control role of almost all regions within the FPC system has been reported in numerous studies (184, 185), the direct relationship between FPC and the other two most salient networks - the DAS and default - has not been systematically studied. Recently, Sridharna et al (183) performed a highly related study reporting that major nodes within the FPC system, particularly the rINS, exert strong causal influence on key nodes of the default and another executive networks during both external attention directed tasks and resting, clearly supporting the mediating role of FPC regions. However, the executive network (including dlPFC and PPC) in their study is largely different from the dorsal attention network. Actually, the dlFPC included in their executive network is included in FPC system in this study, which is consistent with its

primary role in cognitive control and other studies reporting synchronized activity of this region with the other regions in FPC (88, 185).

Besides this difference in network definition, our results extended the previous finding of the mediating role of FPC from three aspects. First, by choosing two functionally different tasks primarily associated with one of the two opposing systems, respectively, our results showed differential regulation of the two opposing systems depending on specific task requirement. During controlled finger tapping where more externally directed attention is needed, FPC increased connectivity with DAS to facilitate task performance (DAS also increases connectivity with MS) while becoming more disassociated with default to suppress its "irrelevant activity." On the other hand, during movie watching where it is more related with default network function (186, 187), FPC becomes significantly more connected with the default while more anti-correlated with the DAS. Secondly, our results indicate that the mediation role of FPC is more a network level function. As shown in Fig.7.5, where all the significant interactions (between regions from paris of networks detected to significantly change interaction across states) were shown across different states, we can see that during finger tapping, except ACC, all other regions (at least unilateral) are involved in "mediating" between DA and default system although bilateral INS seems to be more extensively involved (5 out of 15 with DA and 11 out of 20 with default), which, from this point, is in line with Sridharna et al's (183) finding of the important mediating role of INS during attention demanding tasks. Moreover, during movie watching, essentially all regions are involved in the mediating effort between FPC-DA and FPC-default. Interestingly INS largely disappears except two connections with DA system, lINS-lFEF, and lINS-rFEF. Together with ldlPFC-lFEF and

ldlPFC-rFEF, these are the only 4 (out of 25) positive connections between FPC and DA during this state, likely indicating the attentional budget needed for movie watching given the apparent eye movement control function of FEF. Overall, our results indicate that FPC exerts its mediating role based on coordinated activity of most of its member regions under different task conditions suggesting the network level nature of this mediation. Finally, the partial correlation analysis by regressing out the influence of FPC directly proves FPC's significant mediating effect during each sustained state.

The prefrontal cortex (PFC, including both aPFC and dlPFC) has been widely reported to increase activity in response to increased cognitive load in a variety of goal-directed tasks supporting its critical role in flexible maintenance of different control demanding behaviors and particularly aPFC, the most anterior part of the frontal lobe, has been suggested as the "apex of the executive system underlying decision-making" (184, 185, 188, 189) . Moreover, INS and ACC are commonly observed to be activated by a variety of cognitive control process, particularly those involving conflict monitoring, information integration and response selection (190-192). Finally, the aIPL region has been reported to increase activity during role transition in stimulus-response association task (193) as well as tasks involving control of spatial attention (194). All these functions suggest that regions within FPC are perfectly suited to exert regulation on other functional modules for successful implementation of goal-directed behaviors. The selective "switching on and off" of the two opposing networks observed in this study, however, not only proves that this network is capable of co-activating with dorsal attention system to accomplish attention-demanding tasks, as consistent with the previously mentioned findings, but also shows its flexible role in coping with the default

system while "suppressing" the DAS for primarily internally directed process. This task-selective, differential regulating pattern shows the mediating role of FPC with more liability.

The observation that FPC exerts its mediating role on a network level, together with the other two observations reinforces the increasingly accepted notion that brain is intrinsically organized into distinct networks. First, during resting state, each network is highly synchronized internally (85.8%) while minimal between-network interactions exist (12.8%). Secondly, across different states, no significant with-network difference is detected while the between-network interaction changes (again on network-level) largely account for the transition (Fig.7.2 and 7.3). These salient and stable network organization patterns further support the ongoing effort to look at brain function on large system level during both resting and task performance and calls for specifically designed network-level based techniques to further study brain interaction between large, distributed, systems.

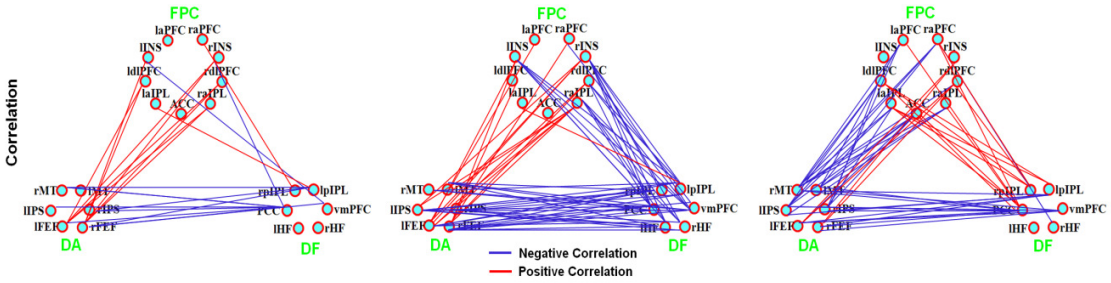

Figure 7.5 Significant connections between pairs of networks that have been detected to significantly change their interaction pattern across different states. Red: significant positive connections; Blue: significant negative connections.

At the system level, the intriguing selective regulation pattern showed in this study seems to suggest that these three systems (FPC, DA and default) form a functional "triad" with FPC at the apex regulating the two branches. This is essentially consistent with the "top-down" control theory (195) during volitional shifts of attention contingent on current task requirements. Another parallel mechanism is "bottom-up" capture of attention, but this is not applicable at the context of this study since there were no salient stimulus and the task was fulfilled largely through purposeful control. On the other branch, however, the default network seems to work alone based on the current observation. However, other networks such as the emotional network may be a potential candidate since previous studies have shown an emotional processing component within major nodes of the default network including MPFC (155) and precuneus (196), A recent study by Pallesen et al (197) further shows that the default network activity decreases to a less extent during processing of negatively charged emotional stimuli when compared to positively charged stimuli, indicating the involvement of the default network in emotional processing (197). Another possibility regarding the emotional network, however, is that it is also directly mediated by the frontal parietal network and if so, this will have important clinical implications for emotional disorders such as depression. There are studies implying this (198, 199) and further studies directly investigating this issue using specifically designed paradigms are needed.

7.5 Extension: A Multivariate Approach for Quantifying Network-level Interactions

As extensively discussed in the previous sections, the brain's interaction and mediation seem to be largely on a network level underscoring the importance of developing a network-level based approach to quantify and compare the interactions

between networks. Although using regional approaches such as described above, important information regarding interactions between networks can be obtained, such regional approaches lack the capability to directly quantify the interaction strength between two networks as a whole. Although this question is not the focus in the previous sections in this chapter, it will be the central topic in this section. Our aim is to develop a multivariate approach to directly quantify the interaction between two sets of regions (networks) as well as possible mediations between them.

Previously Fox et al and Kelly et al (23, 97) investigated the interaction between brain networks, but one of the potential limitations is the means through which brain network interaction was derived. Commonly, an averaged temporal signal of all pre-defined brain regions within each network was obtained first and a correlation between two mean time courses was employed to quantitatively discern the interaction of the two networks (97, 200). That is, these previous studies assume that the mean time course represents the temporal characteristics of all brain regions within the specific network and simplify the multivariate nature of network correlation to a univariate problem. Although facilitating theoretical interpretation and utilizing a straightforward computation, this simplification is prone to information loss and/or even becomes untenable when the homogeneity assumption (i.e., the mean time course can faithfully represent the overall information in a given network) is violated. Furthermore, these approaches cannot be generalized to investigate the interactions of multiple networks, the potential mediation of other brain networks to a pair of networks, and perturbations of network-network interactions beyond the resting state.

To address these limitations, we aimed to develop a framework capable of discerning brain functional network interaction based on the canonical correlation analysis (CCA) (201). In this framework, the network-level correlation and partial correlation will be individually defined and integrated to tackle the problem of network interaction.

7.5.1 Multivariate Network Correlation Using Canonical Correlation Analysis (CCA)

To quantify the network level interaction, a canonical correlation measure between two multivariate vectors was used. Canonical correlation analysis (201) has been widely employed to measure the association between multivariate variables: $X = [x_1, ..., x_m]^T$ and $Y = [y_1, ..., y_n]^T$. Particularly, for two random variables, the canonical correlation is identical to the Pearson's correlation. The key idea of CCA is to maximize the correlation between two linear combinations of X and Y denoted by $U_1 = w_1 x_1 + ... + w_m x_m = w^T x$ and $U_2 = v_1 y_1 + ... + v_n y_n = v^T y$, respectively. The canonical correlation equals the largest eigenvalue of the matrix of $C_{xx}^{-1} C_{xy} C_{yy}^{-1} C_{yx}$ (or $C_{yy}^{-1} C_{yx} C_{xx}^{-1} C_{xy}$). The likelihood ratio test was used to determine the significance of this network-level canonical correlation coefficient (NCC_{xy}). Note the value of NCC_{xy} is between 0 and 1 with 0 indicating no dependence and 1 indicating full dependence between these two sets of variables.

In this study, before CCA, principle component analysis (PCA) was applied to sets of variables within different network. Given the moderate size of human brain functional networks (~10 regions within each network), the primary purpose of this step is not to reduce dimension but rather orthogonalize the information within each network to avoid correlated regressors. Moreover, by selecting a fixed number of principal

components for each network, this step can also eliminate the potential bias of different number of regions in different network in CCA calculation and therefore facilitate the comparison between the network-level interactions.

7.5.2 Network Partial Correlation to Detect Mediation

Partial correlation is a measure of correlation between two random variables, while controlling for a set of other variables. With partial correlation, one could determine what the correlation would be if the influence from the "mediator" has been removed. For univariate statistics, partial correlation $\rho_{xy/z}$ between two random variables x and y controlling for another set of independent covariate $Z=[z_1,...,z_p]^T$ can be computed as the Pearson's correlation between the residuals ε_x and ε_y from two linear regression equations:

$$x = x_0 + \beta_1 Z + \varepsilon_x \quad \textbf{[7.1]}$$

$$y = y_0 + \beta_2 Z + \varepsilon_y \quad \textbf{[7.2]}$$

For the mediation analysis, $\rho_{xy/z}$ denotes the correlation remained between x and y when all mediating effects of Z are removed and the differences between the ordinary correlation ρ_{xy} and $\rho_{xy/z}$, represent the amount of mediation Z exerts on the relation between x and y.

Since the primary focus of this study was to depict correlation between two sets of variables, the above computational procedures need to be generalized to accommodate the multivariate property of this problem. For two sets of multivariate vectors $X=[x_1,..., x_m]^T$ and $Y=[y_1,..., y_n]^T$, and another set of independent covariates

$Z = [z_1,...,z_p]^T$, influences from which will be removed, Eq. 7.1 and Eq. 7.2 can be written as:

$$X = X_0 + \mathrm{B}_1 Z + E_x \quad \textbf{[7.3]}$$

$$Y = Y_0 + \mathrm{B}_2 Z + E_y \quad [7.4]$$

where E_x and E_y are the residual vectors of X and Y, respectively, after regressing on the variable set of Z. Subsequently, the canonical correlation coefficient of E_x and E_y can be calculated, representing the partial correlation $NPC_{XY/Z}$ between the two sets of variables (networks) X and Y. The differences of $NCC_{XY} - NPC_{XY/Z}$ thus represent the mediation effects of Z on the relation between X and Y, similar to the concept of univariate mediation analysis.

Specifically, in this study, network partial correlation was calculated between the DA and default by controlling for FPC to directly test its mediating effect at network level. Similarly, the MS and V network was also used as regressors to calculate the reference mediation effect.

7.5.3 Statistical Analysis

A re-sampling method was developed to test statistical significance of network level interaction for each pair of networks, including the network canonical correlation (NCC_{XY}), and the network partial canonical correlation ($NPC_{XY/Z}$). Specifically, a set of reference regions were selected from whole brain based on the notion of brain's sparse interaction pattern, i.e. depending on different brain states, there will be different subsets of regions demonstrating minimal interactions. As a result this subset of least-interacted regions will be suitable to serve as reference to generate a null distribution of the

network-level interactions. In this study, based on the 90ROI segmentation of the whole brain template (168), we selected a set of 15 reference regions as the subset that demonstrates the minimal average correlation strengths (absolute value). Subsequently, this set of reference regions were randomly distributed to 2 networks with 6 and 9 regions (equal to largest possible combination of number of regions in the five defined networks) and the network-level interactions were calculated 1000 times to generate the null distribution for each interaction. Note this whole process is done for each subject, and the obtained p-value (based on appearance ratio) for each interaction were combined across subjects to give a group p-value using Fisher's method (202, 203). Same procedure was done for each of the three states examined.

To visualize the network-level interaction patterns, the spring-embedding method was employed to reveal the interaction among the five predefined brain networks during each cognitive state (171). Specifically, the spring-embedding approach places strongly interacted networks closer together and vice versa. The width of edges corresponds to the strengths of interactions. Moreover, the statistical grouping of the set of interaction values during each state were also achieved using the Tukey's test at $\alpha = 0.05$ (204) to facilitate the classification of individual values into different categories such as the higher and lower.

7.5.4 Results and Discussion

The significant network-level interaction pattern is shown in Fig.7.6. During the resting state, only three significant connections exist with FPC at the center connecting with DA, DF, and V while MS is left alone. This sparse network-level interaction pattern is consistent with the observation of dominant within-network interactions as shown

using regional techniques (Fig.7.2). Moreover, in line with the mediation role of the FPC between DA and DF, FPC demonstrates a significant connection with both of them.

As we have anticipated, an increase in network-level interaction was observed during finger tapping when compared with resting (Fig.7.2). There are 7 significant inter-network interactions during finger tapping when compared with only 3 during the resting state. The FPC now demonstrates a significant interaction with MS, which is consistent with the observed increasing FPC-MS interaction using regional approaches (Fig.7.2). Actually, the appearance of significant connections between DA and DF as well as DA and MS are all in line with the increased between-network interaction in the previous section (Fig.7.2). In contrast, no significance interactions for FPC-V and DA-V were observed using a regional approach, yet a network-level approach demonstrates significant interactions among them, demonstrating the advantage of using network-level approaches to directly quantify their interaction strength. In addition, using Tukey's test, the interaction between FPC-DA, FPC-DF, DA-MS are statistically stronger ($p<0.05$, red asterisks) than all other interactions during finger tapping,, which reinforces the importance of these three interactions in accomplishing the finger tapping task, which has been extensively discussed above.

The network-level interaction pattern during movie watching seems to be intermediate between resting and finger tapping, which is again expected given the correlation maps in Fig.7.2 and 7.3. Consistently, the FPC-DA and FPC-DF still show significant interaction and statistically higher than others. Other interactions include DA-MS, FPC-MS, and FPC-V, indicate significant interactions between higher order

attention/control systems and both sensory systems during the composite movie watching task.

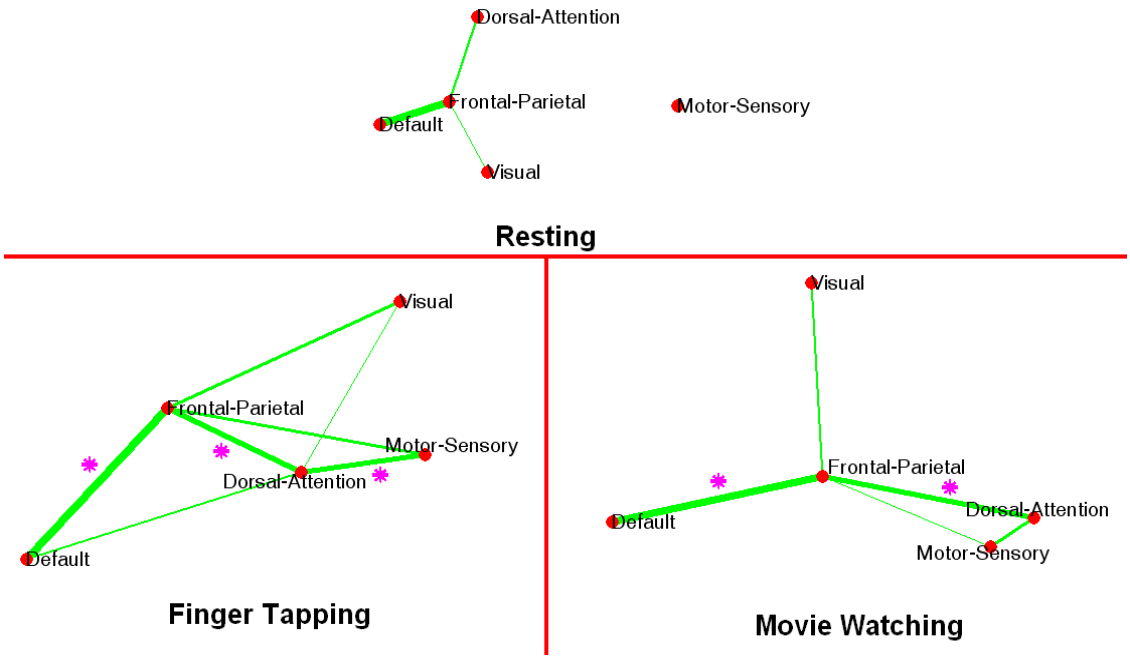

Figure 7.6 Network-level interaction patterns during all three states. Pink asterisks: significantly stronger interaction comparing with others in the same graph. All connections shown here are statistically significant.

Finally, in order to directly test the mediation role of FPC on the two opposing systems- DA and DF, we calculated the network-level partial correlation between DA and DF using FPC as control set of variables (the other two systems-MS and V are also used as controllers for comparison with FPC). The result is shown in Fig.7.7, where the pattern is strikingly similar as those using regional techniques (Fig.7.4): FPC demonstrates significant mediation effects during every single state (RS: p=0.0012; FT: p=.0377; MW: p=0.0105) and is the only network showing such effect during resting. In contrast, V fails to show any significant mediation effect during any state. Although MS

shows significant effects during FT (p=0.0141) and MW (p=0.0430), its effect is significantly weaker that that of FPC (p=0.0442) during MW. Overall, the evidence from both regional technique and network-level approaches strongly support the mediating role of FPC on the two opposing system: DA and DF.

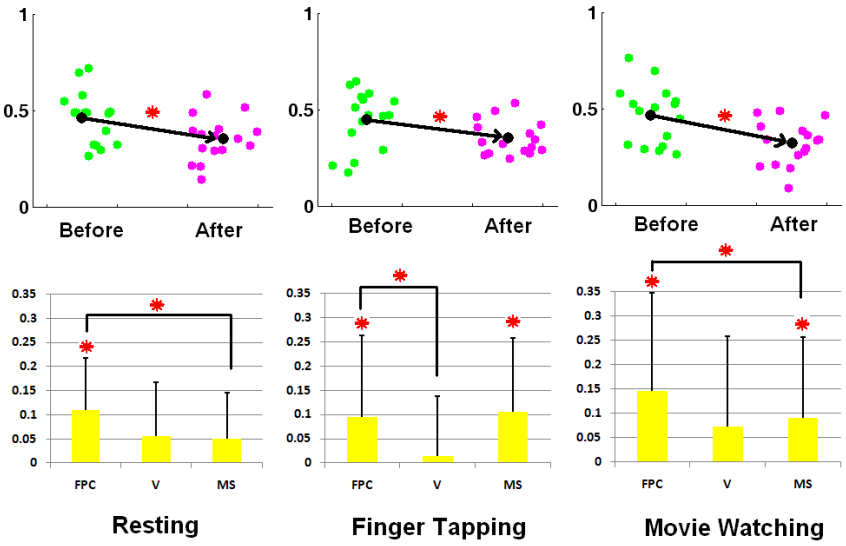

Figure 7.7 Exploring the mediation effects of FPC on the interaction between DA and DF based on the network-level approach. Top row: the effect of removing FPC effects on the interaction between DA and DF; Bottom row: the comparison of mediating effects of FPC, MS and V on the interaction between DA and DF.

In conclusion, the newly developed multivariate approach successfully reveals the network-level interaction pattern during three different states and the converging findings of both approaches strongly indicate the mediating role of FPC between the two opposing systems: DA and DF. Future research will continue to look into the application of this network-level approach on developmental as well as disease studies.

Chapter 8

Development of Whole Brain Functional Organization in the First Two Years of Life

Exploring brain functional development/interaction of specific networks was discussed in the previous Chapters. In this Chapter, we will shift our focus to characterize whole brain networks, aiming to provide a systematic delineation of different aspects of brain development including inter-regional connectivity, modular structure, functional hubs as well as graph theoretical measures such as local/ global efficiency and small-worldness.

8.1 Introduction

Understanding of whole brain functional organization is essential in revealing the underlying mechanisms of how it works. Specifically, characterizing its developmental process can potentially gain insight into its matured architecture. Recent advance of neuroimaing techniques, particularly the resting-state functional connectivity MRI (rfcMRI) (20), greatly facilitates the investigation of brain's functional organization. Instead of focusing on a specific function elicited by certain task as traditional fMRI does, rfcMRI detects the intrinsic temporal synchronization when the brain is not engaged in any explicit task, i.e., "idling", and has been increasingly recognized as a powerful tool to study intrinsic brain organization. The essence of rfcMRI lies on the fact that highly

temporally correlated regions during the resting state resemble the activated regions during task performance. In other words, rfcMRI provides unique information of how the brain is intrinsically and spontaneously organized (20). Ever since its emergence, exciting progress has been made in adult studies, greatly improving our understanding of the whole brain functional architecture. For example, Salvador et al (205) first looked at the whole brain functional network during the resting state and described the system as an anatomically sensible small-world (206) with both high global and local efficiency. Damoiseaux et al (22) detected a consistent set of networks utilizing an independent component analysis approach (ICA), revealing the sub-system organization of the whole brain network. Similarly, other studies have (207, 208) investigated the modularity structure of the whole brain network. There are also studies exploring significant modulations of whole brain organization during aging (100) and under various pathologies including schizophrenia (209), Alzheimer's (210) etc, underscoring the usefulness and importance of rfcMRI in studying the brain's functional organization.

The application of rfcMRI in brain development is also emerging. Both Fair et al (211) and Supekar et al (212) compared school-age children (i.e. 7-9 years old) with adults and reported converging evidence on the increasing of long-range connections and decreasing of short-range connections. Moreover, using the graphic theory approach, they found similar small-world property shared by the children and adults even under dramatic organization changes. While these findings are exciting and greatly improve our understanding of brain's functional development, whether these findings can be generalized to an earlier developmental phase, especially the first few years of life, is yet to be answered. The importance of the first few years of life, especially the first two years

in brain development is unparalleled (33). Most neurophisiological events including neruogensis, synaptic formation, axonal elongation, and myelination have been well documented to undergo the trunk of their development during this time although each of them has a unique time course which may extend well into early adulthood (40, 213-217). As a result, the importance of characterizing brain's functional development during this critical developmental period can not be over emphasized.

Previously, we have separately looked into the development of several specific functional networks, including motor-sensory, visual(29) and the "default" network(102) during this critical first two year period. The general picture of whole brain organization change remains poorly characterized. In this study, based on a large population (n=167) of pediatric subjects with an age spaning from 2 weeks to 2-year-old, we aimed to reveal the large scale brain organization changes during this poorly studied but critical period. Inter-regional connectivity development as well as organization changes revealed by modular structure(218), functional hubs, as well as global graph theoretical metrics including local efficiency, global efficiency and small-worldness (206) will be individually tackled to provide a systematic exploration of whole brain development during this earliest phase of postnatal brain development.

8.2 Methods

8.2.1 Subjects and Image Acquisition

The study subjects were part of a large study on characterizing brain development in normal and high risk children (163). Informed consent was obtained from the parents and the experimental protocols were approved by the institutional review board. None of the subjects was sedated for MR imaging. Before the subjects were imaged, they were fed,

swaddled, and fitted with ear protection. All subjects slept during the imaging examination. We retrospectively identified 167 normal subjects including 61 neonates (33M, 21±11days (SD)); 60 1-year-olds (35M, 13±1mon) and 46 2-year-olds (24M, 24 ±1mon) who met the inclusion and exclusion criteria (supporting materials). In addition, 19 (12M, 25~33yrs) healthy adult subjects were also recruited for comparisons with pediatric subjects. A board-certified neuroradiologist (JKS) reviewed all images to verify that there were no apparent abnormalities in the acquired MR images.

A 3D MP-RAGE sequence was used to provide anatomical images to co-register among subjects. The imaging parameters were as follows: repetition time (TR)=1820ms; echo time (TE)=4.38 ms; inversion time=1100ms; 144 slices; and voxel size = 1x1x1mm3. For the rfcMRI studies, a T2*-weighted EPI sequence was used to acquire images. The imaging parameters were as follows: TR=2sec, TE=32 ms; 33 slices; and voxel size =4x4x4 mm^3. This sequence was repeated 150 times so as to provide time series images.

8.2.2 Preprocessing

The preprocessing includes standard steps including exclusion of voxels outside of the brain using FSL (FMRIB, Oxford University, U.K.), time shift, motion correction, and spatial smoothing (6-mm full width at half maximum Gaussian kernel). Three adult subjects were excluded from the subsequent analysis because of excessive head motion during the scan. Nuisance signals from ventricle, white-matter, and global signal were regressed out using linear regression. The first 10 time points of the rfcMRI data were excluded to allow T1 to reach equilibrium condition. Subsequently, rfcMRI data of the first available time point was co-registered to the corresponding T1-weighted MP-RAGE

structural images using rigid body alignment. For within-group registration, independent T1 Images from a longitudinal data set scanned at neonate, 1yr and 2yr olds were selected as templates for corresponding pediatric groups and intensity-based HAMMER nonlinear registration (164) was performed to warp each individual subject to its template space. After that, the pediatric images were normalized to MNI space using 4D HAMMER registration between the three longitudinal data sets and the MNI template. The reason for using a longitudinal dataset as templates was the higher registration accuracy in registering them with a common template, which is achieved by 4D HAMMER registration which takes into account the longitudinal correlation information. Subsequently, the transformation fields from rigid alignment and two-step HAMMER registration were employed to bring all fMRI volume data to MNI template space, allowing group analysis. Whole brain region of interest (ROI) definition was then achieved using anatomical templates defined by Tzourio-Mazoyer et al (168), which divides the whole brain into 90 cortical and sub-cortical regions.

8.2.3 Inter-regional Correlation Analysis

The mean time course of each ROI was separately extracted from each individual subject to construct a 90*90 correlation matrix which was then fisher-Z transformed and averaged across subjects to compute the mean correlation matrix for each group. To explore the inter-regional connection development with age, the connection strength vector for each inter-regional connection composed of all individual subjects was compared across consecutive age groups using one-way ANOVA. Significant changes were defined using a threshold p=0.05 after FDR multiple comparisons correction(170). In addition, for each connection within each age group, two-way t-test was performed to

calculate a p-value indicating the significance level of the particular connection to be different from zero. This p-value was used as a measure to threshold the correlation matrix to get sparse matrix, which will be described in next section.

In order to test the relationship between connectivity change and anatomical distance, the Euclidian distance between the centers of each ROI was computed to represent the distance between each pair of regions.

8.2.4 Modularity analysis

To detect the modular structure of the whole brain networks, each correlation matrix must be thresholded to create an adjacency matrix, the element of which will either be nonzero, if the corresponding connection exceeds the threshold; or 0, if it does not. In this study, we chose to use the p-value associated with all connections as a threshold measure to create the adjacency matrix. Clearly the choice of threshold will have major effect on the topology of the resulting network: conservative thresholds will produce sparsely connected graphs, which might induce "isolated" nodes and falsely eliminates "true" connections while more lenient thresholds will generate densely connected graphs, which might include "spurious" connections and approache a random graph. As a result, the adoption of any single threshold will inevitably raise the concern of possible bias associated with this unique value. Thus in this study, we thresholded each matrix repeatedly over a range of costs *K* (total number of existing edges within a graph G over the maximum possible number of edges) to avoid such bias. The minimum of this range was chosen to be a fairly stringent value of K=0.1 (100), i.e. 10% of the maximum number of edges, to minimize the number of spurious edges. Another 15 increasingly more lenient cost thresholds were subsequently evaluated at a step-wise

fashion with a step size of 0.01 to achieve a maximum threshold of 0.25 representing a compromise between dense connection and randomness.

For modularity detection, we applied the weighted version of the spectral algorithm proposed by Newman (218, 219), which finds the optimal division of the whole network so that maximum interactions are within modules while minimal interactions are between modules, which collectively define a statistically "surprising" network structure. At each cost, the optimal modular structure was detected and the solutions were compared across different costs and the results are shown in Fig.8.1, where the number of modules, the modularity scores and the difference between consecutive costs (number of regions that were put into different modules) are presented. As shown, for all age groups, the modularity scores decline as the cost increases as the network approaches randomness. However, clearly the modular structure is reasonably consistent between consecutive costs (red line), particularly within the high-lighted costs (yellow), the modular structures are identical. So the modular structure resulting from these "identical" cost thresholds were reported in this study. Specifically, they were [0.19, 0.20] for neonates, [0.18, 0.21] for 1yr olds, [0.15, 0.18] for 2yr olds, and [0.13, 0.20] for adults.

In addition, spring embedding (171), which iteratively reposition each node within the whole graph so that most strongly connected nodes will be put closer to each other and vice versa, was applied using the leading cost within the "identical" zone (0.19 for neonates, 0.18 for 1yr olds, 0.15 for 2yr olds, and 0.13 for adults) to visualize the whole brain network architecture and validates the findings using modular detection. Using other costs within the zone produces similar results.

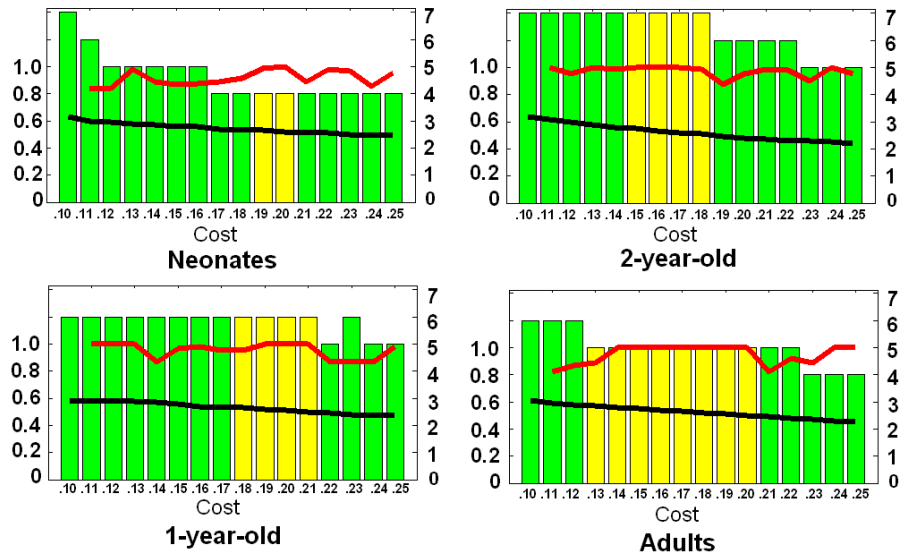

Figure.8.1 Modularity detection comparison at different costs. Bars indicate the number of regions that are assigned to different modules compared with the previous threshold (against the right axis). Red lines show the modularity score (against the left axis). Yellow bars indicate those costs that show identical modularity detections, which are then shown in the result section.

8.2.5 Hubs Detection using Betweenness Centrality

For all graph theoretical analysis including betweeness centrality and small-world metrics as described in the next section, we use a binary adjacency matrix. Betweenness centrality, defined as the fraction of shortest paths between any pair of nodes that travel through the node of interest, characterizes the importance of a particular node in the whole network traffic and nodes with high centrality measures may serve as "relay centers" or hubs of information integration. The betweenness centrality is defined as:

$$BW_i = \frac{1}{N(N-1)} \sum_{s \neq i \neq t}^{N} \frac{P_{st}(i)}{P_{st}} \tag{8.1}$$

where P_{st} is the total number of shortest paths between node s and t within the whole graph and $P_{st}(i)$ is the total number of shortest paths that pass through node i. N: number of nodes within the graph.

In this study, the betweenness centrality for each node is calculated using all cost thresholds within the "identical zone" defined by same modular structures as described previously. The result showed high level of consistency as shown in Fig.8.2, and the results based on the first cost within the "identical zone" (0.19 for neonates, 0.18 for 1yr olds, 0.15 for 2yr olds, and 0.13 for adults) are reported in the result section. The hubs are defined as those nodes demonstrating relatively high centrality measures (BW_i>mean+SD).

8.2.6 Small-worldness metrics

Three graph-theoretical metrics, namely local efficiency (LE), global efficiency (GE), and small-worldness (SW) are calculated to explore the economic properties of the whole brain network.

Specifically, the clustering coefficient introduced by Watts and Strogatz (206) is a measure of local efficiency which quantifies the information transfer efficiency within the immediate neighborhood of node i:

$$\mathrm{E_{local}(i)} = \frac{1}{\mathrm{N_{G_i}(N_{G_i}-1)}} \sum_{\mathrm{j,k \in G_i}} \frac{1}{\mathrm{L_{jk}}} \quad (8.2)$$

where $\mathrm{N_{G_i}}$ is the number of nodes within subgraph Gi constituted by the immediate neighbors of node i. The local efficiency of the whole graph is then obtained by averaging across all nodes.

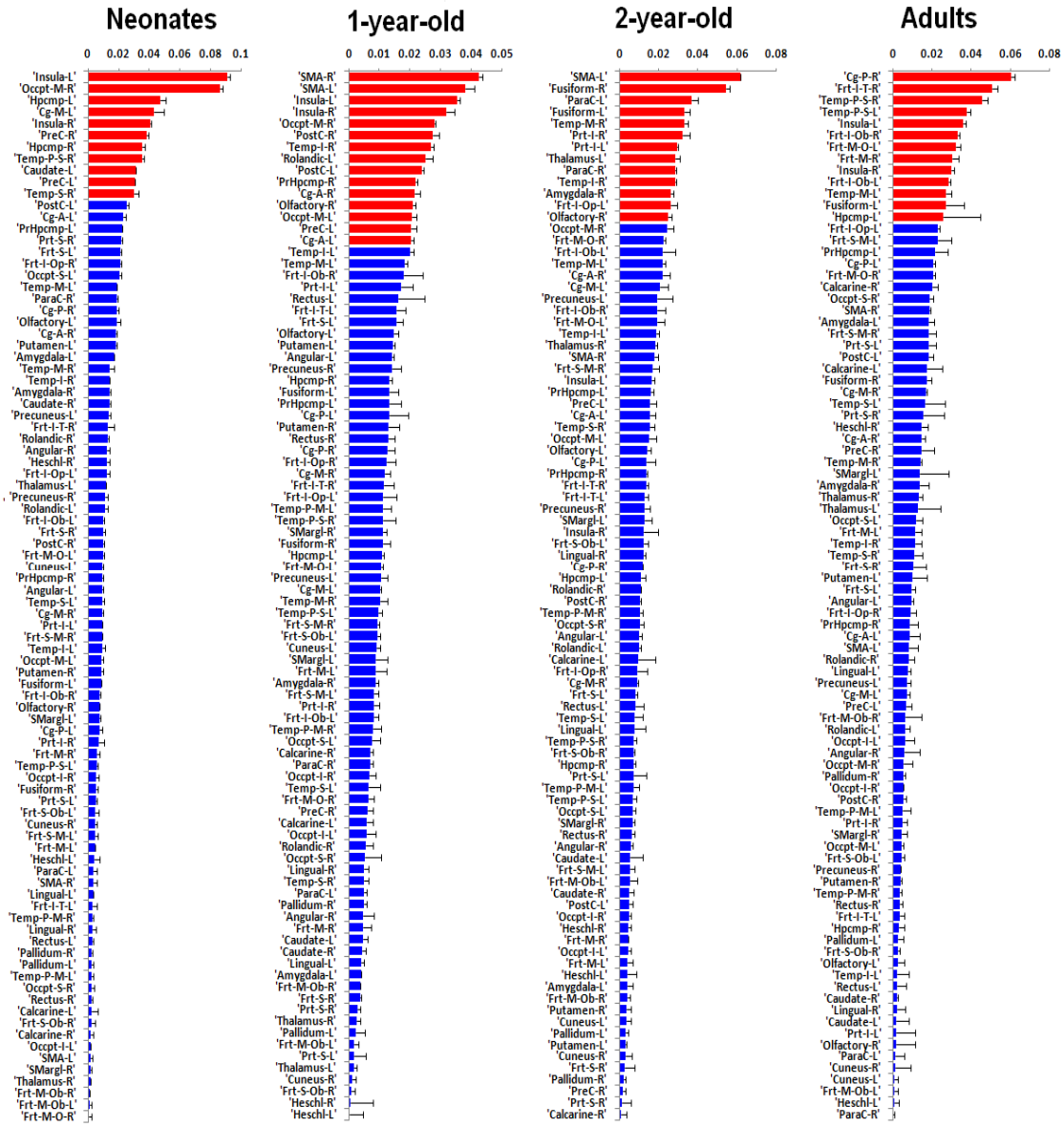

Figure 8.2 Consistency of betweenness centrality measures across the identified costs range.

The harmonic mean of the inverse of the minimum path length between each pair of nodes within the network, Lij, represents the efficiency of parallel information transformation within graph G and is a measure of global efficiency (220):

$$E_{global} = \frac{1}{N(N-1)} \sum_{i \neq j \in G} \frac{1}{L_{ij}} \quad (8.3)$$

where N is the number of nodes within network G. The average minimum path length of the whole graph itself is defined as the "characteristic path length".

A small-world network, according to Watts and Strogatz (206), should have characteristic path length comparable to a regular graph and clustering coefficient greater than a random graph. Hence by calculating the ratio of clustering coefficient Cl/Cl_{random} and characteristic path length Cp/Cp_{random} between the network of interest and a random network (degree reserved), the small-worldness is defined as the ratio of the two ratios with a value above 1 indicating the existence of small-world property.

In this study, correlation matrix from individual subjects of each age group were thresholded (based on correlation strength) to construct networks at costs ranging from 0.01 to 0.50 at a step size of 0.01 and corresponding small-world metrics as described above are calculated at each cost for each subject.

8.3 Results

8.3.1 Inter-regional Functional Connectivity Development

For each individual subject, a whole brain correlation matrix (90*90) was constructed using regionally averaged spontaneous BOLD fluctuations based on anatomical templates defined by Tzouro-Mazoyer et al (168). In order to detect developmental changes within the global functional architecture, connectivity between each pair of region (altogether 4005 pairs) was compared across age groups using the correlation strength vector (fisher-Z transformed) composed of all subjects within each age group. One way ANOVA was applied for testing significance and a threshold of p=0.05 after multiple comparisons correction (FDR) (170) was chosen to define significant changes with age. The significant difference matrix along with the

visualization of the increasing (red) and decreasing (blue) connections in corresponding partial-transparent brain volume are presented in Fig.8.3. Altogether, there are 634 connections (634/4005=15.83%) showing significant increase and 922 connections (922/4005=23.02%) showing significant decrease in connectivity strength during the first year of life, which cover broadly the whole brain demonstrating the most dynamic and wide-spread functional development during the critical first postnatal year. In great contrast to the extensive changes during the first year, the second year witnesses a dramatically slower development: there are 75 connections (1.87%) increasing and 67 connections (1.67%) decreasing during this year. Qualitatively, the increasing/decreasing connections seem to reside mainly in the posterior/frontal part of the brain, respectively, although a significant portion of increasing connections is between frontal and posterior regions (Fig.8.3). Finally, comparing 2yr olds with adults, 457 connections (11.41%) significantly increase strength and 393 connections (9.81%) significantly decrease strength, which again extensively cover the whole brain. Overall, it is clear that brain undergoes the most extensive reshaping during the first year of life while during the second year the rate dramatically slows down. However, tacking together the massive changes between 2yr olds and adults and previous reporting of significant changes between school-aged children and adults (211, 212), this reshaping process, although considerably slower than the first year, is likely to be steadily continued till adulthood.

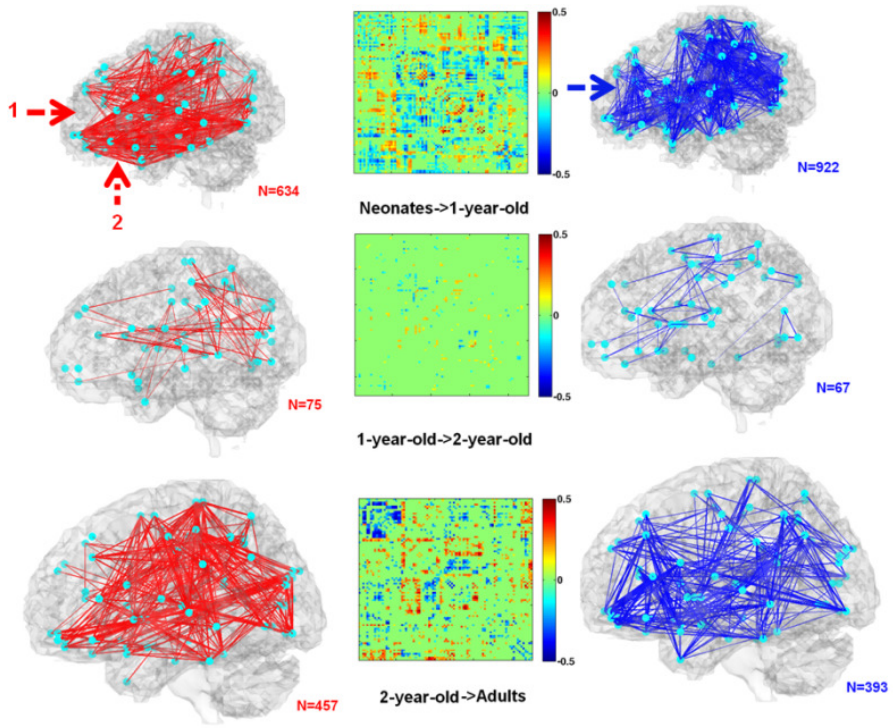

Figure.8.3 Inter-regional connection changes across each age span (red: increasing connections; blue: decreasing connections).

8.3.2 Connectivity Development in Relation to Anatomical Distance

As has long been observed, the developmental process features reduction of strength among short-distance connections and strengthening among long-distance connections (211, 212), which suggests a simultaneous specialization of neighboring regions and integration of remote regions during development. However, most previous fcMRI studies focused on the change between children and adults while in this study, this trend is validated and extended to the first two postnatal years. As shown in Fig.8.4, between each age span, connections decreasing with age (blue dots) consistently demonstrate shorter anatomical distances; on the other hand, connections increasing with

age (red dots) are collectively associated with longer anatomical distances ($p<10^{-10}$ from neonates to 1yr olds, $p<10^{-5}$ for 1yr to 2yr olds and $p<10^{-9}$ for 2yr olds to adults).

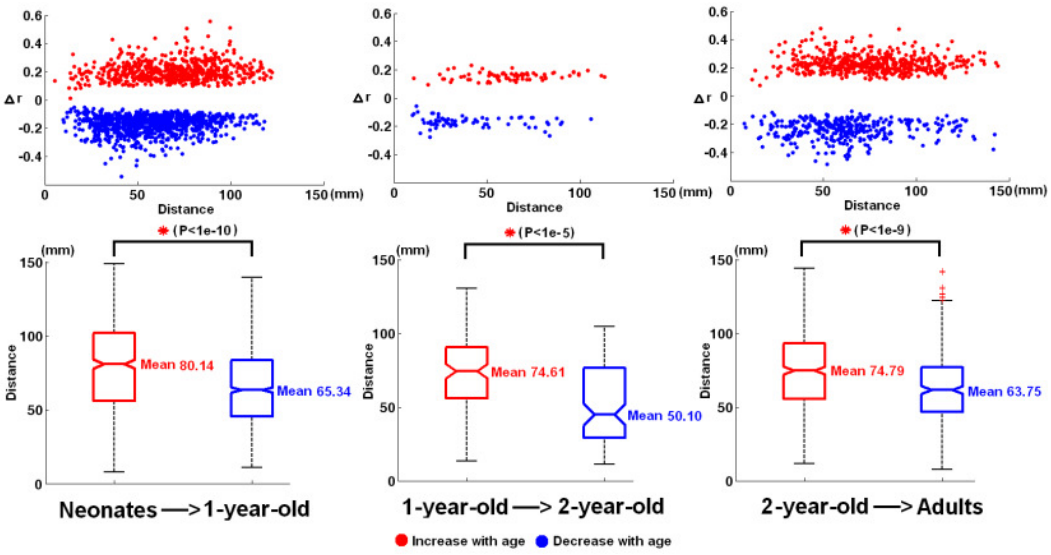

Figure.8.4 Connectivity Development in Relation to Anatomical Distance

8.3.3 Connectivity Development in Relation to Different Anatomical Divisions

In order to explore the differential development pattern within different anatomical divisions, the whole brain regions were classified into frontal (24 regions), parietal (18), temporal (8), occipital (14), limbic (14) and sub-cortical (12) divisions based on that proposed by Tzourio-Mazoyer et al (168). A detailed list of regions in each sub-group can be found in Table.8.1. As shown in Fig.8.5, the frontal (24%), parietal (31%), and sub-cortical (30%) divisions mainly experience specialization during the first year of life while the other divisions including temporal (32%), occipital (31%) and limbic (30%) are dominated by synchronization. With the minimal changes occurred during the second year, the differential increasing/decreasing pattern within each lobe is

not as obvious. Finally, from 2yr olds to adults, the frontal (34%), limbic (20%) and sub-cortical (24%) are dominated by specialization while parietal (13%), temporal (29%), and occipital (15%) are mainly synchronizing. In addition to the differential developmental pattern within each division, there are considerable differences among between-division connections (as shown in Fig.8.6). These connections are of importance and characterize how different anatomical divisions change their interaction pattern to form more functionally sensible modules responsible for the emerging and complex cognitive functions. As a result, these between-division developmental patterns, as well as those within divisions, will be discussed together with the functional modular structure changes in the following section.

8.3.4 Development of the Functional Modular Architecture

The exploration of modular structures at different ages can potentially answer the critical question of how the whole brain is organized at different developmental periods. The modular structure was detected based on a spectral optimization model (218, 219) using the sparse connectivity matrix derived from each age group and the results are presented in Fig.8.7. In this figure, the most significant 405 connections (cost 10%) for each age group were also visualized to aid interpretation. A list of region abbreviations (in the figure) is presented in Table.8.2 and the detailed list of regions in each module for each age group is presented in Table.8.3.

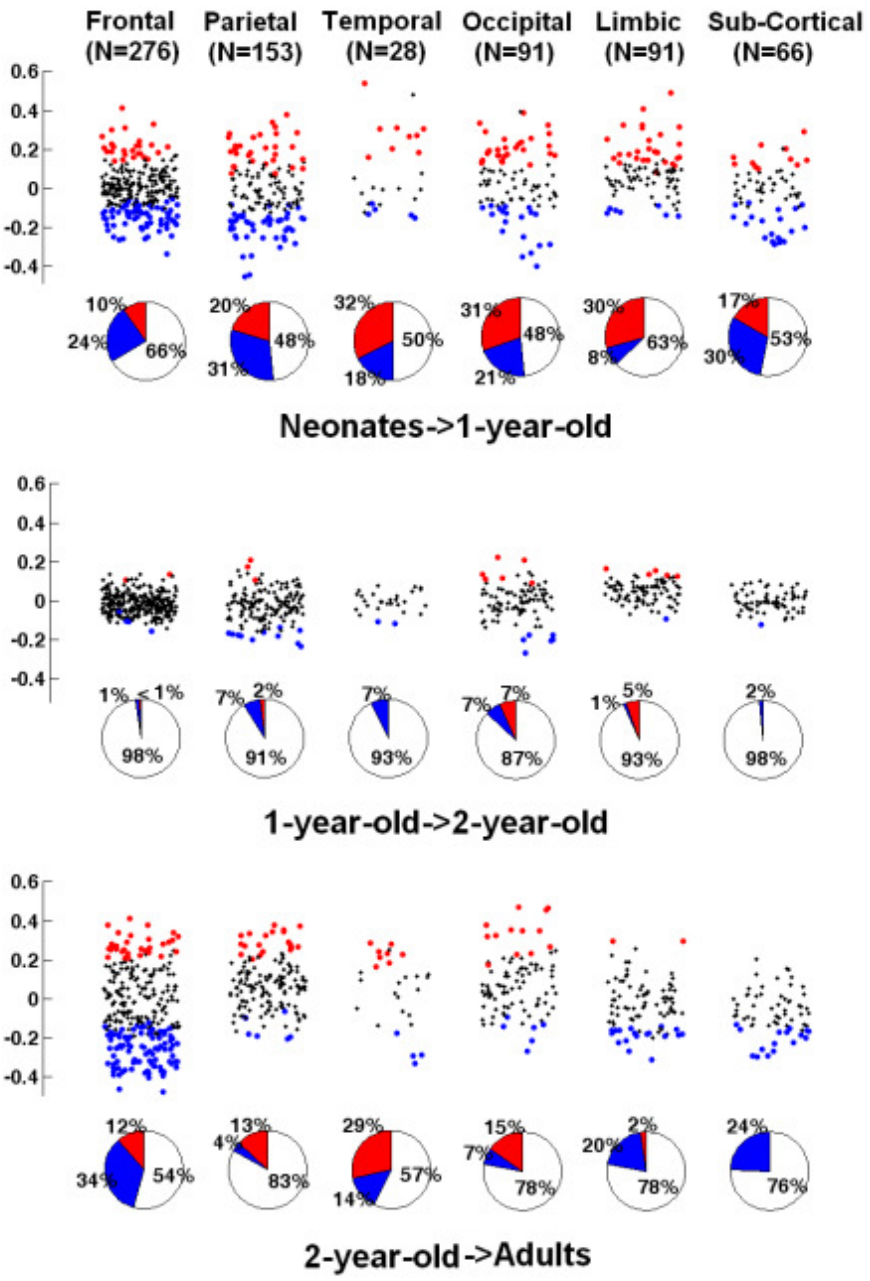

Figure.8.5 Connectivity Development in Relation to Different Anatomical Divisions-within divisions

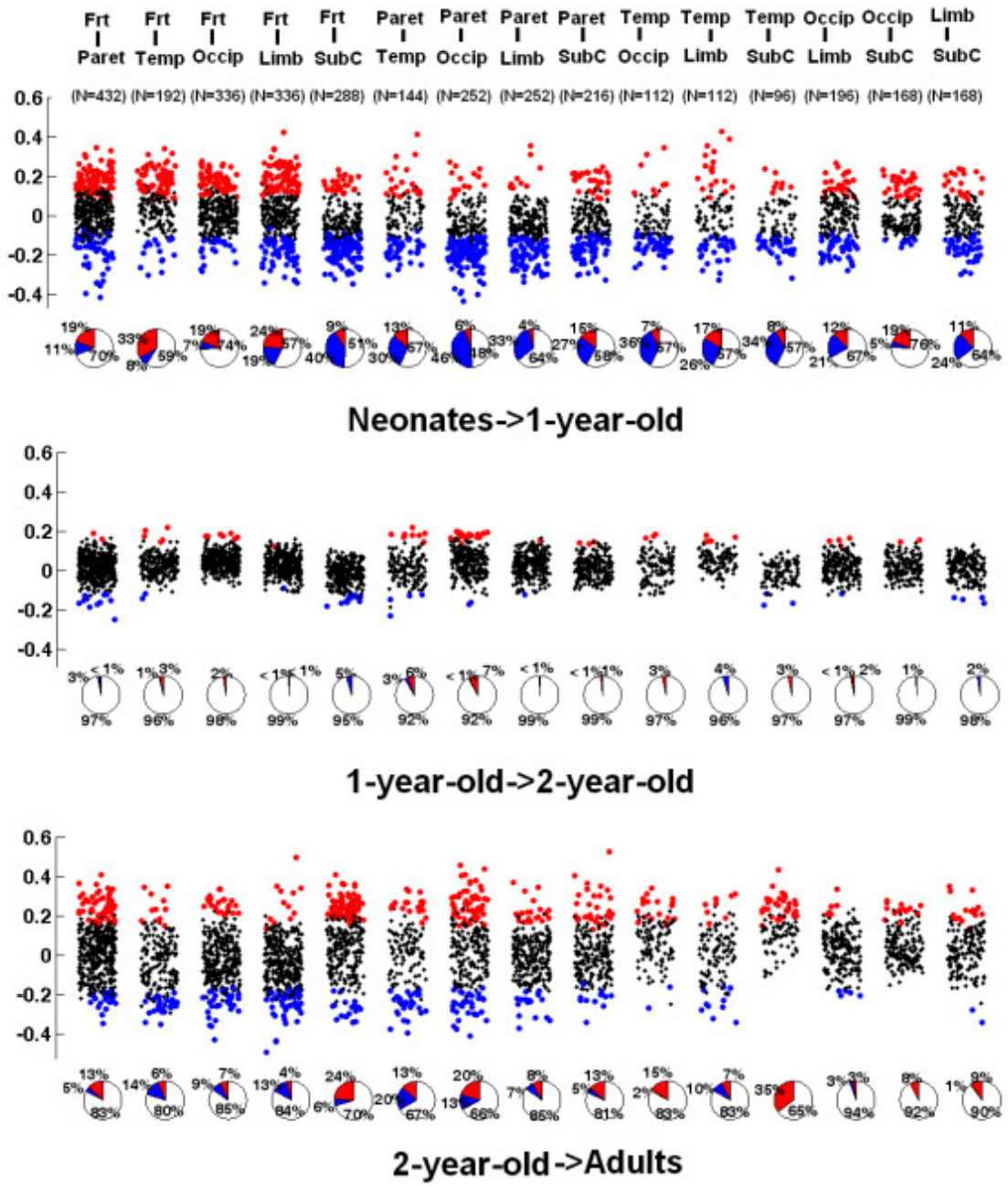

Figure 8.6 Connectivity Development in Relation to Different Anatomical Divisions-between divisions.

The neonatal brain is broadly divided into four major modules which show clear anatomical division constraints. One module (21 regions) covers mainly regions in the frontal division (19 out of 21), and is therefore designated the frontal module. The

module (19 regions) including central regions of bilateral pre- and post central gyri, supplementary motor area, and paracentral lobule, as well as most parietal lobe regions and limbic regions of mid- and post cingulate cortex is designated as the parietal-limbic module. The module (25 regions) covering mainly the occipital lobe (14 regions) and temporal lobe (8 regions) is referred to as the occipital-temporal module. Finally, the module (25 regions) containing all sub-cortical regions (12) as well as other surrounding frontal, parietal and temporal regions (13) is called the sub-cortical-centered module. Overall, neonates demonstrate a more anatomically sensible modular organization characterized by local and neighboring regional clusters constrained by anatomical divisions.

From neonates to 1yr olds, the parietal-limbic module remains almost identical with only the left superior marginal and bilateral angular gyri added, providing a full coverage of the parietal lobe. However, other modules undergo extensive reorganization including both segregation and integration. Firstly, the frontal module now divides into two with the more dorsal part forming a separate module (11 regions) and the orbital part merging together with mostly temporal regions forming a integrated orbital-frontal-temporal module (24 regions). The segregation between the dorsal and orbital parts of the frontal lobe can actually be predicted by the inter-regional connectivity changing patterns shown in Fig.8.3 where there are extensive decreasing connections (blue arrow) while no increasing connections between them (red arrow 1). Moreover, consistent with these decreasing, the frontal division is dominated by specialization (24% decreasing vs 10% increasing) as shown in Fig.8.3. Similarly, the integration between orbital frontal and temporal regions can also be traced back to the synchronizing process between them

as shown in Fig.8.3 (red arrow 2) and in Fig.8.6 where a dominant synchronization trend is observed between the frontal and temporal lobe (33% increasing vs 8% decreasing). Secondly, the occipital-temporal module now also separates with most temporal regions merged with orbital frontal regions, leaving an intact module covering solely occipital regions (14 regions). This segregation is also supported by both the dominant specializing process between temporal and occipital divisions (36% decreasing vs 7% increasing, Fig.8.6) and the self-synchronization process within the occipital division (31% increasing vs 21% decreasing, Fig.5). Finally, eight sub-cortical regions plus bilateral hippocampus are segregated from the surrounding frontal, parietal and temporal regions in the sub-cortical-centered module and forms two separate modules (10 and 9 regions, respectively), which are then termed as sub-cortical module and "mixed" modules, respectively. Overall, the first year witnesses dramatic segregations within the frontal lobe, between the occipital lobe and temporal lobe, between sub-cortical regions and surrounding regions, as well as integration between orbital frontal lobe and temporal lobe regions (among others, e.g. amygdala).

The reorganization occurring during the second year is far less dramatic as consistent with the minimal connectivity changes (Fig.8.3) during this period. However, a closer observation of the actual changes indicates that there are important ongoing fine-tuning processes. There is also intermediate structure emerging during this period which is likely the steping-stone towards more mature modules. First, the right opercular inferior frontal gyrus is separated from the "mixed" module and integrated into the dorsal-frontal module, making both modules totally left-right symmetric. Moreover, the bilateral parahippocampal gyri and amgdala now separate from the orbital-frontal-

temporal module and merge into the sub-cortical module (where all other sub-cortical regions as well as bilateral hippocampus are already there), making both of the modules more functionally sensible. Except the parietal-limbic module (22 regions), these five regions (out of 90-22=68 regions) are the only changes taking place during the second year since the intact occipital module formed in 1yr olds remains identical at this time. Although minimal, these fine tuning processes, actually make the modular structure more functionally sensible. Finally, the comprehensive parietal-limbic module now separates into two modules: one that still covers broadly the central, medial parietal as well as limbic regions (14) while the lateral surface of the parietal lobe including superior/inferior parietal, supramarginal, and angular gyri (8 regions) are separated and form a module of its own. This is intriguing given the fact that these regions, together with the limbic regions (posterior cingulate cortex) and medial parietal regions (precuneus) also separate from the parietal-limbic module and integrate with dorsal frontal regions to form a salient frontal-cingulate-parietal module in adults. This makes the separation of the eight regions during the second year an intermediate structure between pediatric subjects and adults. Together with other possible changes in later life, this might act as steping-stones towards the maturd modular structure observed in adults.

Finally, the modular structure in adults is more consistent with known functional relationships (Fig.8.7). A central module (bilateral pre- and post- central gyri, supplementary motor area, and paracentral lobule) focuses on motor-sensory controls (20, 22, 29). A comprehensive occipital-temporal module possibly deals with multiple sensory modalities including visual, auditory, olfactory and memory (32, 47, 221, 222). A stand-alone orbitofrontal module likely involvses in affective decision making/rewarding

mechanism (223). A comprehensive cortical-subcortical module consistent with the basal gangalia-cortical network mediates motivation and emotion drive and integrates information for goal-guided behavior (224). In addition to these, the most salient module, as mentioned above, is the frontal-cingulate-parietal module that spans across the anterior-posterior brain, which includes regions within superior medial frontal, posterior cingulate, precuneus, inferior parietal lobule as well as angular gyri among other frontal and parietal regions. This module is qualitatively very similar to the recently defined "default-mode" network (21, 26-28), indicating that the matured brain architecture features such higher-order cognitive function directed modules. More importantly, the long-range integration between frontal and posterior regions of the brain revealed by this composite module is only observed in the adult group, indicating the important integration process occurring after 2yr olds and consistent with the notion that brain grows from "local to distributed" (211, 212).

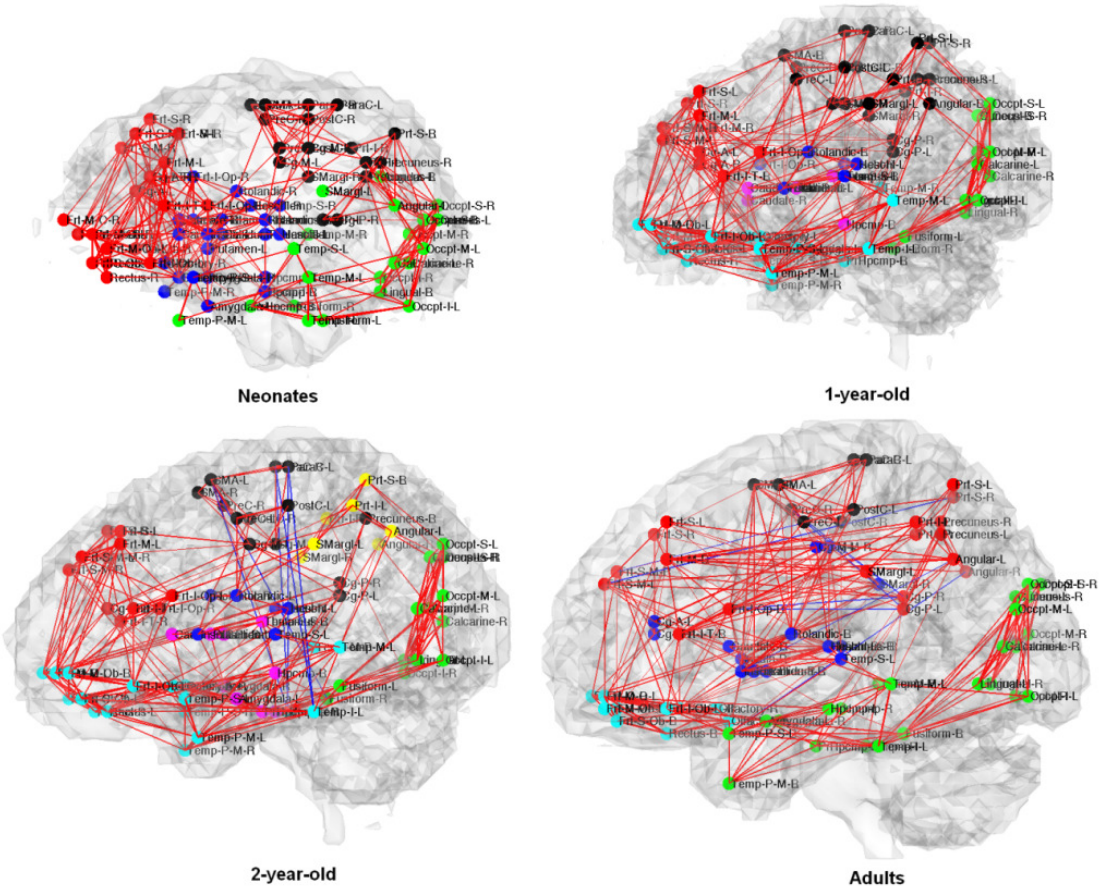

Figure.8.7 Development of the Functional Modular Architecture. Nodes are colored according to different modules and the most significant 405 (10%) connections were also visualized to aid interpretation.

8.3.5 Development of the Functional Modular Architecture Revealed by Spring Embedding

In addition to modular structure detection, we used another visualization technique, namely spring embedding (171), to qualitatively examine and validate the organizational relationship among the 90 whole brain regions. Spring embedding iteratively optimizes the position of each node within the whole graph according to their

connection strengths so that regions with stronger connections will be put closer to each other and vice versa. As a result, we would expect nodes within a functional module to be put together as a "cluster" while nodes within different modules will be scattered. The same sparse correlation matrices used in modular structure detection were used in this analysis and the results are presented in Fig.8.8 where all nodes are labeled in colors consistent with the modular detection results (Fig.8.7) and the most significant 405 connections are also visualized to aid interpretation.

As expected, the spring embedding plots nicely put each individual module as a "closely connected cluster" while different modules are generally well separated. This consistent finding with the modular results reinforces the notion that whole brain system is organized into age-specific modules which experience dramatic reorganization during early brain development before reaching a matured architecture.

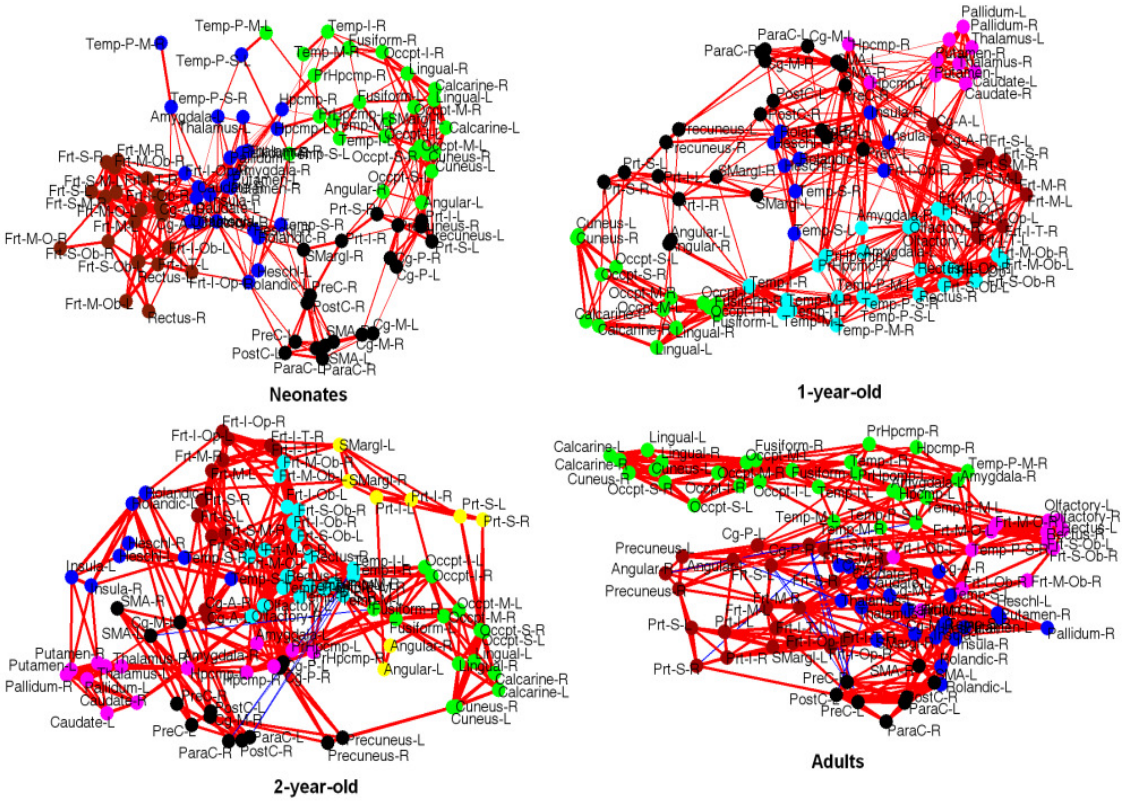

Figure 8.8 Development of the Functional Modular Architecture Revealed by Spring Embedding. Nodes were similarly colored as those in Figure 8.7.

8.3.6 Emergence and Development of Functional Hubs during Development

The notion of hubs in a functional brain system has long been held which may potentially act as relay centers to facilitate efficient information transformation and integration (207). In this study, the role of each node was characterized using betweenness centrality (173, 225), which measures the relative importance of corresponding node in achieving global maximal efficiency. The potential "hubs" were defined as those that demonstrate the highest centrality measures (>mean+SD).

The bar plots of all regional centrality measures are presented in Fig.8.9 (red: hubs) and the visualization of the defined hubs in actual brain space is presented in Fig.8.10. As shown, left insula and right middle occipital regions are the two major hubs in neonates with others covering pre-central, hippocampus, middle cingulate, etc. In 1yr olds, left insula together with bilateral SMA regions show highest centrality measures which then evolves to left SMA and bilateral fusiform in 2yr olds. Together, there is reasonable continuity in the hub evolution; it gradually changes from insula/middle occipital to SMA/insula and SMA/fusiform regions across the first two years of life. Moreover, there is a general trend of middle to posterior region bias for the hub locations among pediatric subjects as obvious in Fig.8 while no frontal regions are classified as hubs for all three pediatric groups except for the left inferior orbitofrontal region in 2yr olds. However, the emergence of one region in 2yr olds does suggest a trend of the emergence of the hub role in frontal lobe. Indeed, with right posterior cingulate as the

strongest hub in adults (Fig.8.9), there are altogether 5 frontal regions also subserving hub roles. This finding is consistent with the role of this lobe in integrating information, decision making and other complex cognitive behaviors in matured brain (226).

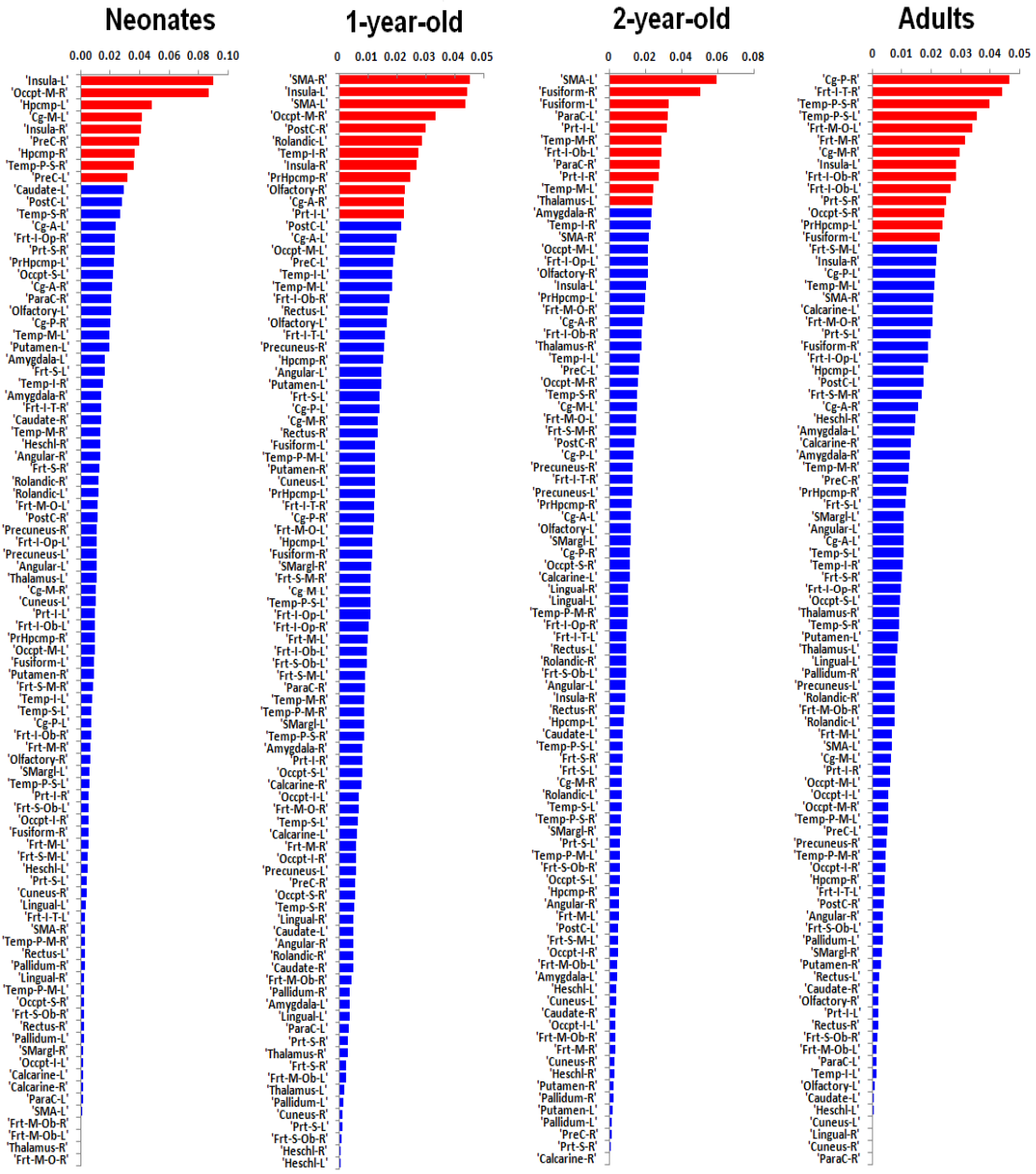

Figure 8.9 The bar plots of all regional centrality measures. Hubs were highlighted in red.

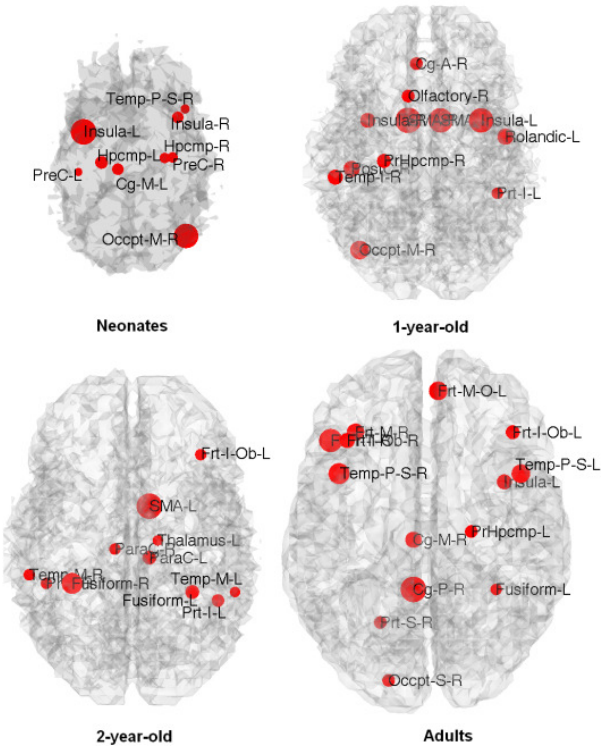

Figure 8.10 Visualization of the defined hubs in brain space.

8.3.7 Development of Small-world Properties

Many studies (100, 227, 228) have reported the small-world characteristic of the matured brain functional system. However, when the small-world property emerges and how it evolves with age, particularly during the first two years of life, are not known. Moreover, as described above, considerable changes occur in inter-regional connections, modular organizations, as well as hub distribution during the first two years of life. The natural next question is whether these changes are expressed in small-world properties, which measures the economic property of the entire brain network as a whole. In this section, we examined three commonly used small-world metrics including local efficiency (LE) and global efficiency (GE), which quantify the information transferring efficiency at a local neighboring subgraph and the whole network level(220), respectively,

and the small-worldness measure (SW) (206). A small-world network is characterized by a higher LE than random network as well as a higher GE than regular (lattice) network. In this case, the small-worldness indicator (SW) will have a value greater than 1.

As shown in Fig.8.11, both the LE and GE curves for all 4 examined age groups are between the corresponding curves of random and regular network for most cost values (except of extremely low/high costs in which case the network is likely either un-connected or full of spurious random connections), indicating the presence of the small-world property for all brain networks. This finding is further supported in Fig.8.11c, where the direct indicator-SW is shown. All networks demonstrate SW values above 1 across the whole cost span. As this observation essentially tells us that the whole brain functional network demonstrates the small-world property immediately after birth and throughout development, we are also interested in the development of this property with age. As shown in Fig.8.11, comparing 1yr olds with neonates, the LE measure is significantly higher at cost ranging from 0.03~0.19; the GE is significantly higher at cost ranging from 0.04~0.47; and the SW measure is significantly higher at cost ranging from 0.08~0.19, suggesting a significant improvement of small-world properties during the first year of life at both local and global level, which is consistent with the observation of extensive inter-regional connection changes during this period as shown in Fig.8.3. Given the minimal inter-regional connection changes, we would expect minimal changes in small-worldness properties during the second year of life. As shown in Fig.8.11, no significant changes are observed for any metric. However, even with similarly extensive inter-regional changes as those in the first year, the time period between 2yr olds and adults still witnesses no significant changes in small-world properties. This finding is

consistent with the previous findings comparing children with adults (211, 212) where results were reported that even though brain undergoes considerable inter-regional connection changes the global small-world property is minimally changed. The findings in this study extend this "plateau" pattern to 1 yr olds.

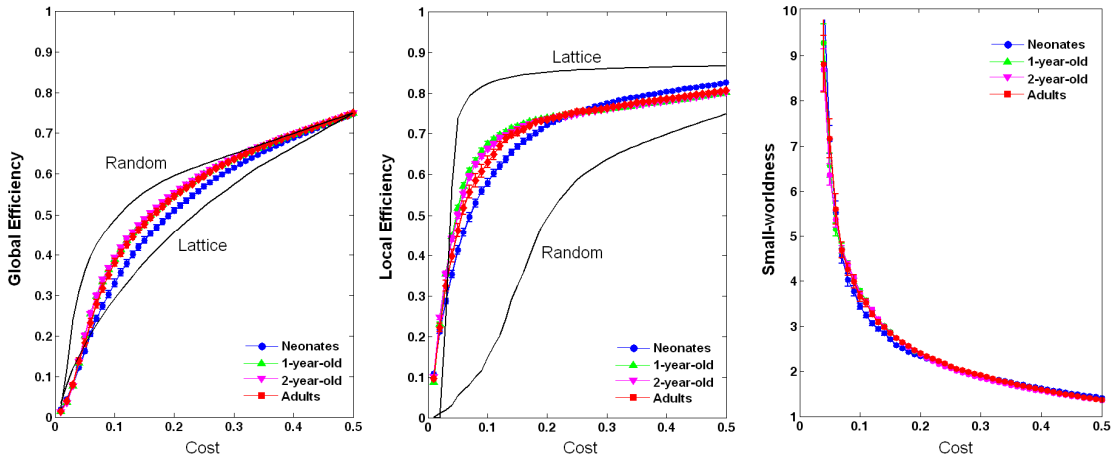

Figure 8.11 Development of global efficiency, local efficiency and small-worldness.

8.4 Discussion

Brain's functional organization is of paramount importance in understanding the underlying mechanisms of how it works. To our knowledge, this is the first study to characterize the evolution of whole brain organization during the first critical two years of life. We systematically investigated the brain functional connectivity development in terms of its inter-regional connections, modular organizations, as well as graph-theoretical metrics to depict the growth patterns of both local and global parameters during this critical period. The main findings of this study are: (1) brain's inter-regional connections undergo the most extensive reshaping (both synchronization and specialization) during the first year of life, followed by dramatically slower changes; (2)

the decreasing of short-range connections and increasing of long-range connections are observed across each age span; (3) neonatal brain demonstrates a largely anatomically constrained modular organization and experiences drastic reorganization during the first year of life which features extensive segregation/integration associated with frontal lobe regions, followed by a "fine-tuning" during the second year and finally achieves a more functionally sensible modular structure in adults; (4) the top functional hubs emerge at insula/middle occipital regions in neonates, shift to insula/SMA in 1yr olds and SMA/fusiform in 2yr olds, and finally move to the posterior cingulate/frontal regions in adults; (5) local efficiency, global efficiency and small-worldness measures exhibit significant improvement during the first year of life while they show minimal changes despite of considerable underlying reorganizations beyond 1yr of age. Taken together, these findings provide new insights into very early postnatal development of whole brain organization.

8.4.1 Development of Inter-regional Connections

The massive inter-regional connection development with both synchronization and specialization during the first year of life has two important implications, including the obviously critical role of first year in the brain's overall functional development and the surprisingly high level of functional connectivity in neonates (the whole brain correlation matrix is provided in Fig.8.12). Taking together with the well-defined modular structure at this age, these results suggest high level prenatal functional development. These findings are not surprising if considering the fact that axons undergo a period of rapid elongation and establish extensive synapses/connectivity to their intra- and subcortical targets from midgestation through infancy (111). On the other hand, if

the temporal synchronization dose comprise of functional information, we would expect some sort of functional capability in the prenatal brain. Indeed, studies have shown that most fetuses begin to respond inconsistently to sound by moving or kicking as early as 25-27 gestation weeks (229). This finding fits nicely with Standley's claim in one of his 1998 papers, "newborn is not a blank state waiting to be filled as previously thought, but is an avid and experienced learner equipped with the beginning discriminations and memory of language, emotional response, and awareness of cause/effect relationships" (229).

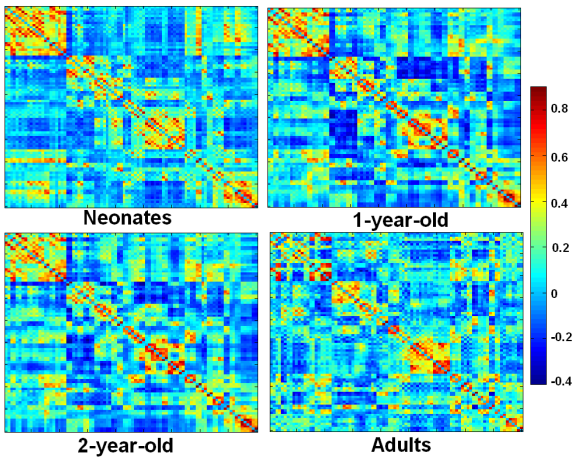

Figure.8.12 Group mean correlation matrix of all 4 age groups

Regarding the critical first postnatal year, numerous studies, mostly from structural aspects, have provided solid evidence on its essential role in the overall brain development (33, 213-217). Actually, most relevant neural development events including synaptic formation, axonal elongation, pruning and myelination demonstrate a consistent developmental trend as characterized by rapid growth during the first postnatal year before continuing at a much slower but steady pace thereafter (40, 213-217), which

fits nicely with the functional connectivity observed this study. These different neural developmental processes are likely the underlying neural substrates for the observed functional connectivity development. More specifically, synaptic formation, establishment of both short and long-range axonal connections, and myelination likely underlie the functional synchronization while the synaptic pruning process explains functional specialization between different regions (108, 230).

As mentioned above, although different processes experience the trunk of their development during the first year of life, they are also well documented to extend further into development. For example, synaptic formation is documented to undergo substantial growth staring from midgestation throughout the first two postnatal years (231, 232) while myelination and synaptic pruning continues to grow to reach the adult level utill young adulthood (232-238). Collectively, these processes determined by genes and influenced by environmental factors, are likely the neural substrates for all of the observed inter-regional functional connectivity changes across each age span. We believe that the observed massive changes during the first year are most likely dominated by the genetically determined maturation of the neural substrates. However, it is generally believed that as age grows, experience will gradually exert more influence on the selective strengthening and weakening of different functional pathways through the interaction with these neural substrates. Therefore, the much slower but steady changes occurred after 1yr old are likely subject to the combined effects of both factors (108, 230). Finally, the observed decreasing of short-range connections and increasing of long-range connections are in line with previous findings by both Fair et al (211) and Supekar et al (212). They showed similar functional segregation between regions close in anatomical

space and integration between regions further away when comparing children with adults. The findings in this study extend their observations to the very early postnatal period.

8.4.2 Development of Whole Brain Modular Structure and Hubs

As the growth pattern of inter-regional functional connectivity validates the previous anatomical findings, the exploration of the brain's modular structure/hubs and their evolution with age will provide us unique perspectives into brain's functional organization and reorganization.

One of the most intriguing findings here is the extensive reorganization process during the first postnatal year, especially the prefrontal cortex (PFC). Human PFC comprises between a quarter to a third of the entire cortex and is anatomically and functionally heterogeneous. The PFC is usually subdivided into dorsal-lateral PFC (DL-PFC), medial PFC (MPFC) and orbitofrontal cortex (OFC) in adult studies (223). As all PFC regions are generally involved in "executive" functions (EF), there is a general consensus that the DL-PFC deals more with the "pure" cognitive aspects of EF in abstract reasoning and problem solving while MPFC and OFC, especially OFC is more involved in affective or emotionally related decision making (223). Historically, PFC is believed to be one of the latest parts of the brain to develop and it is not functional until about 4-7 years of age (239) or even later (240). However, the findings in this study clearly suggest a much earlier development within PFC. It starts from an intact module covering all PFC regions in neonates. Subsequently, there is a clear segregation of OFC from other DL-PFC and MPFC regions. Moreover, the OFC seems to get integrated with other regions (including amgdala and temporal, frontal regions) to form a composite module during the first year of life. The active segregation of two major divisions of PFC likely indicates

functional specialization between the two sub-divisions. Actually, numerous studies have proved the incorrectness of the historical view of very late PFC development. PFC functions start to emerge probably during the second half of the first postnatal year (223, 241), which is consistent with the findings in this study. Specifically, Grossmann et al (242) have recently reported that even at the age of five months, infants actively recruit the DL-PFC regions when engage in a joint attention task with another person, strongly supporting the development of DL-PFC in executive functions during this period. On the other hand, lesion studies in rhesus monkeys conducted by Goursaud and Bachevalier (243) have proved that neonatal lesions (10~15 days postnatal) in OFC resulted in weaker infant-mother attachment when compared with controls assessed at a age of 11 months, clearly supporting the role of OFC in the quality and/or strength of social attachment relationship building. In addition, the integration of OFC with other regions especially amygdala and parahippocampal regions observed in this study supports the behavioral findings of attachment formation in infants with their mother (244). Moreover, in human studies, protracted and increasingly more severe social self-regulation deficits with age have been seen in children with early damage to the PFC, including OFC (243, 245). Collectively, the findings of extensive segregation/integration process within PFC observed in this study are consistent with previous findings of corresponding cognitive functional/behavioral development and strongly support the notion of early PFC development during the first postnatal year.

After the drastic reorganization occurred during the first year, results in this study reveal a “fine-tuning” process during the second year. Except for the segregation of the lateral parietal regions from the parietal-limbic module, only 5 out of 68 regions are

classified into different modules comparing to 1yr olds. Again, this process appears far from random given that the changes make the modules more symmetric as well as more functionally sensible. The appearance of an intermediate structure – the lateral parietal module, as described in the result section, is intriguing since this seems to correspond well with the developmental process by formation of intermediate structures. Actually, looking at the development of the modular structures across the whole age span examined in this study, it reveals several interesting patterns. First, the primary motor-sensory system (including bilateral pre- and post-central and SMA) is within one module ever since neonates and remains so utill adulthood. However, through the age of 1 year old, they are extensively interconnected with other lateral/medial parietal regions as well as limbic regions and are classified into a big composite module. In 2yr olds, the lateral parietal regions separate out demonstrating certain level of specialization. Finally in adults this system becomes much more specialized and forms a "stand-alone" module representing a distinct function underlying it, supporting the importance of specialization for functional maturation. On the other hand, although the DL-PFC and OFC are segregated during the first year of life and remains so during the second year, it is only in adults that frontal lobe establishes extensive connections with posterior cingulate as well as parietal regions and forms the most salient frontal-cingulate-parietal module, simiar to the "default-mode" network (26, 28). Given the higher order cognitive functions subserved by the default network (26-28, 155), this observation is consistent with the notion that these higher order cognitive functions do not mature at the early childhood and continue to develop utill adulthood (226). Actually, the observation here is consistent with one of our previous findings (102) where we specifically evaluated the

development of the default network using independent component analysis (ICA). In that study, the default networks in all three pediatric groups (neonates, 1yr and 2yr olds) are classified into two independent components covering the frontal and parietal part, respectively. It is only in the adult group, do these two components merge together to form an intact "default network". The converging observation from both ICA and modular detection here strongly supports that the integration of frontal lobe and cingulte, parietal regions to form an intact module occurs after the age of two.

In addition to the modular structure, the betweenness centrality measure also reveals potential "hubs" within the whole brain network. The findings in this study suggest that the major hubs evolve from insula/occipital regions in neonates, SMA/insula in 1yr olds to SMA/fusiform areas in 2yr olds, demonstrating an important evolution trend as well as reasonable continuity during the developmental process. The insula cortex, locating between the temporal lobe and frontal lobe, possesses abundant connections with temporal cortex, SMA, primary motor-sensory cortex, cingulated area and amgdala. It specializes in many different functions, including motor control, auditory processing, speech production, as well as autonomic functions (246). Our finding of bilateral insula regions being among the major hubs in neonates is in line with its "miscellaneous" nature. More importantly, it has long been known that this area is the first cortex to differentiate and develop in fetus beginning from 6 weeks after conception (246, 247), providing the structural basis for its hub role immediately after birth as observed here. Subsequently, the hubs gradually transform to the SMA area in 1yr olds, which suggest the central role of motor-related function during this year. This finding is not surprising given the abundant evidence of major improvement in motor skills

occurring during this period. For example, target-directed reaching to grasp marks the development of the third postnatal month (248). Hand-to-hand transfer occurs around 6 months of age (249). This developemtn does not contradict with the significant frontal lobe development as described above since most of the mentioned behaviors represent functional coordination among motor, sensory, and association circuits including those in frontal lobe, especially for those target-directed behaviors such as inhibitory control over reflexive behaviors occurring around the same 3 month of age (248). In 2yr olds, besides SMA, fusiform areas also appear among the top hubs, indicating dramatic development involved in visual function. This finding is again consistent with one of our previous studies suggesting that motor-sensory networks undergo rapid development during the first year of life followed by similar development in the visual network that are more prominent in the second year of life (29). Taken together, the hubs detected during the first two year of life are consistent with the dramatic motor and visual related function development during this period of time (29, 33).

Comparing pediatric subjects with adults, it is apparent that the major hubs among the pediatric groups are more involved with basic motor (SMA), visual (right-occipital, fusiform) and control (insula) functions, while the hubs in adults, the posterior cingulate and inferior frontal, deals more with high-order cognitive functions such as episodic memory, referential activity and decision making (175, 179, 181, 226). This finding suggests a gradual shift of brain's most important regions from sensory processing to cognitive processing, which is in line with the developmental time course of these functions. Regarding the hubs detected in adult group, Hagmann et al (42) conducted an extensive structural connectivity study, where they found that "the spatial distribution of

ROIs with high betweenness centrality shows high centrality for regions of medial cortex such as the precuneus and posterior cingulate cortex, as well as for portions of medial orbitofrontal cortex, inferior and superior parietal cortex, as well as portions of frontal cortex." Their findings are highly consistent with our results (Fig.9), suggesting strong structural basis for the detected "functional hubs" in this study.

8.4.3 Development of Small-world Properties

Finally, our results show that starting from neonates, the brain exhibits a small-world network organization, which reinforces the important role of prenatal functional development (33). Significant improvement of small-world properties is observed during the first year of life, which is consistent with the most extensive inter-regional connectivity changes (Fig.1) as well as modular structure reorganizations (Fig.5). However, after 1-year-old, the small world property shows minimal changes utill adulthood. Surprising as this result seems to be, it is to some extent consistent with the previous findings comparing school age children with adults (211, 212) where they also failed to observe significant small-world property changes. Our results extend this "plateau" period to the end of 1-year-old, suggesting that even though brain undergoes extensive inter-regional connection changes as well as dramatic modular structure changes after the first year, its global small world property gets neither improved nor disturbed but rather remains stable. Given the fact that local clustering is already one of the features in neonates and the establishment of most long-range connections are done before 1-year-old (250-252), this finding seems to reflect the facts that small-worldness is not sensitive to organization changes once these two elements are both met. On the other

hand, this reinforces the important role of the first year in global brain development, both structurally and functionally.

Table 8.1 List of regions in anatomical sub-divisions			
Frontal	Superior frontal gyrus	**Occipital**	Superior occipital gyrus
	Middle frontal gyrus		Middle occipital gyrus
	Inferior opercular frontal gyrus		Inferior occipital gyrus
	Inferior triangular frontal gyrus		Cuneus
	Superior medial frontal gyrus		Calcarine cortex
	Paracentral lobule		Lingual gyrus
	Superior orbital frontal gyrus		Fusiform gyrus
	Superior medial orbital frontal gyrus		
	Middle orbital frontal gyrus		
	Inferior orbital frontal gyrus		
	Rectus gyrus		
	Olfactory gyrus		
Parietal	Superior parietal gyrus	**Limbic**	Temporal pole: superior temporal gyrus
	Inferior parietal gyrus		Temporal pole: middle temporal gyurs
	Angular gyrus		Anterior cingualte cortex
	Supramarginal gyrus		Median cingulate cortex
	precuneus		Posterior cingulated cortex
	Precentral gyrus		Hippocampus
	Postcentral gyrus		Parahippocampal gyrus
	Supplementary motor area		
	Rolandic operculum		
Temporal	Superior temporal gyrus	**Sub-cortical**	Amygdala
	Middle temporal gyurs		Caudate nucleus
	Inferior temporal gyrus		Putamen
	Heschl gyrus		Pallidum
			Thalamus
			Insula

Table 8.2 Abbreviations of regions			
Frt-S	Superior frontal gyrus	**Temp-S**	Superior temporal gyrus
Frt-M	Middle frontal gyrus	**Temp-M**	Middle temporal gyurs
Frt-I-Op	Inferior opercular frontal gyrus	**Temp-I**	Inferior temporal gyrus
Frt-I-T	Inferior triangular frontal gyrus	**Heshl**	Heschl gyrus
Frt-S-M	Superior medial frontal gyrus	**Occpt-S**	Superior occipital gyrus
ParaC	Paracentral lobule	**Occpt-M**	Middle occipital gyrus
Frt-S-Ob	Superior orbital frontal gyrus	**Occpt-I**	Inferior occipital gyrus

Frt-M-O	Superior medial orbital frontal gyrus	**Cuneus**	Cuneus
Frt-M-Ob	Middle orbital frontal gyrus	**Calcarine**	Calcarine cortex
Frt-I-Ob	Inferior orbital frontal gyrus	**Lingual**	Lingual gyrus
Rectus	Rectus gyrus	**Fusiform**	Fusiform gyrus
Olfactory	Olfactory gyrus	**Temp-P-S**	Temporal pole: superior temporal gyrus
Prt-S	Superior parietal gyrus	**Temp-P-M**	Temporal pole: middle temporal gyurs
Prt-I	Inferior parietal gyrus	**Cg-A**	Anterior cingualte cortex
Angular	Angular gyrus	**Cg-M**	Median cingulate cortex
SMargl	Supramarginal gyrus	**Cg-P**	Posterior cingulated cortex
Precuneus	precuneus	**Hpcmp**	Hippocampus
PreC	Precentral gyrus	**ParaHpcmp**	Parahippocampal gyrus
PosC	Postcentral gyrus	**Amygdala**	Amygdala
SMA	Supplementary motor area	**Caudate**	Caudate nucleus
Rolandic	Rolandic operculum	**Putamen**	Putamen
Pallidum	Pallidum	**Thalamus**	Thalamus
		Insula	Insula

Table 8.3.1 Regions in different modules-neonates

Frontal		**Parietal-Limbic**	
Frt-S-R	Frt-I-Ob-R	PreC-R	Prt-S-R
Frt-S-L	Frt-I-Ob-L	PreC-L	Prt-S-L
Frt-S-Ob-R	Frt-S-M-R	SMA-R	Prt-I-R
Frt-S-Ob-L	Frt-S-M-L	SMA-L	Prt-I-L
Frt-M-R	Frt-M-O-R	Cg-M-R	SMargl-R
Frt-M-L	Frt-M-O-L	Cg-M-L	Precuneus-R
Frt-M-Ob-R	Rectus-R	Cg-P-R	Precuneus-L
Frt-M-Ob-L	Rectus-L	Cg-P-L	ParaC-R
Frt-I-Op-L	Cg-A-R	PostC-R	ParaC-L
Frt-I-T-R	Cg-A-L	PostC-L	
Frt-I-T-L			
Occipital-temporal		**Sub-cortical-centered**	
PrHpcmp-R	Occpt-I-L	Frt-I-Op-R	Putamen-R
PrHpcmp-L	Fusiform-R	Rolandic-R	Putamen-L
Calcarine-R	Fusiform-L	Rolandic-L	Pallidum-R
Calcarine-L	SMargl-L	Olfactory-R	Pallidum-L
Cuneus-R	Angular-R	Olfactory-L	Thalamus-R
Cuneus-L	Angular-L	Insula-R	Thalamus-L
Lingual-R	Temp-S-L	Insula-L	Heschl-R
Lingual-L	Temp-M-R	Hpcmp-R	Heschl-L
Occpt-S-R	Temp-M-L	Hpcmp-L	Temp-S-R
Occpt-S-L	Temp-P-M-L	Amygdala-R	Temp-P-S-R
Occpt-M-R	Temp-I-R	Amygdala-L	Temp-P-S-L

Occpt-M-L	Temp-I-L	Caudate-R	Temp-P-M-R
Occpt-I-R		Caudate-L	

Table 8.3.2 Regions in different modules-1-year-old

Dorsal Frontal	**Orbital-frontal-temporal**		**Parietal-Limbic**	
Frt-S-R	Frt-S-Ob-R	PrHpcmp-R	PreC-R	Prt-S-L
Frt-S-L	Frt-S-Ob-L	PrHpcmp-L	PreC-L	Prt-I-R
Frt-M-R	Frt-M-Ob-R	Amygdala-R	SMA-R	Prt-I-L
Frt-M-L	Frt-M-Ob-L	Amygdala-L	SMA-L	SMargl-R
Frt-I-Op-L	Frt-I-Ob-R	Temp-P-S-R	Cg-M-R	SMargl-L
Frt-I-T-R	Frt-I-Ob-L	Temp-P-S-L	Cg-M-L	Angular-R
Frt-I-T-L	Olfactory-R	Temp-M-R	Cg-P-R	Angular-L
Frt-S-M-R	Olfactory-L	Temp-M-L	Cg-P-L	Precuneus-R
Frt-S-M-L	Frt-M-O-R	Temp-P-M-R	PostC-R	Precuneus-L
Cg-A-R	Frt-M-O-L	Temp-P-M-L	PostC-L	ParaC-R
Cg-A-L	Rectus-R	Temp-I-R	Prt-S-R	ParaC-L
	Rectus-L	Temp-I-L		

Occipital		**Sub-cortical**	**Mixed**
Calcarine-R	Occpt-M-R	Hpcmp-R	Frt-I-Op-R
Calcarine-L	Occpt-M-L	Hpcmp-L	Rolandic-R
Cuneus-R	Occpt-I-R	Caudate-R	Rolandic-L
Cuneus-L	Occpt-I-L	Caudate-L	Insula-R
Lingual-R	Fusiform-R	Putamen-R	Insula-L
Lingual-L	Fusiform-L	Putamen-L	Heschl-R
Occpt-S-R		Pallidum-R	Heschl-L
Occpt-S-L		Pallidum-L	Temp-S-R
		Thalamus-R	Temp-S-L
		Thalamus-L	

Table 8.3.3 Regions in different modules-2-year-old

Dorsal Frontal	**Orbital-frontal-temporal**		**Parietal-Limbic**	**Lateral Parietal**
Frt-S-R	Frt-S-Ob-R	Temp-P-S-R	PreC-R	Prt-S-R
Frt-S-L	Frt-S-Ob-L	Temp-P-S-L	PreC-L	Prt-S-L
Frt-M-R	Frt-M-Ob-R	Temp-M-R	SMA-R	Prt-I-R
Frt-M-L	Frt-M-Ob-L	Temp-M-L	SMA-L	Prt-I-L
Frt-I-Op-L	Frt-I-Ob-R	Temp-P-M-R	Cg-M-R	SMargl-R
Frt-I-Op-R	Frt-I-Ob-L	Temp-P-M-L	Cg-M-L	SMargl-L
Frt-I-T-R	Olfactory-R	Temp-I-R	Cg-P-R	Angular-R
Frt-I-T-L	Olfactory-L	Temp-I-L	Cg-P-L	Angular-L
Frt-S-M-R	Frt-M-O-R		PostC-R	
Frt-S-M-L	Frt-M-O-L		PostC-L	
Cg-A-R	Rectus-R		Precuneus-R	
Cg-A-L	Rectus-L		Precuneus-L	

				ParaC-R	
				ParaC-L	
Occipital		**Sub-cortical**		**Mixed**	
Calcarine-R	Occpt-M-R	Hpcmp-R	PrHpcmp-R	Rolandic-R	
Calcarine-L	Occpt-M-L	Hpcmp-L	PrHpcmp-L	Rolandic-L	
Cuneus-R	Occpt-I-R	Caudate-R	Amygdala-R	Insula-R	
Cuneus-L	Occpt-I-L	Caudate-L	Amygdala-L	Insula-L	
Lingual-R	Fusiform-R	Putamen-R		Heschl-R	
Lingual-L	Fusiform-L	Putamen-L		Heschl-L	
Occpt-S-R		Pallidum-R		Temp-S-R	
Occpt-S-L		Pallidum-L		Temp-S-L	
		Thalamus-R			
		Thalamus-L			

Table 8.3.4 Regions in different modules-Adults

Frontal-Cingulate-Parietal		**Occipital-temporal**		**Sub-Cortical-Cortical**	
Frt-S-R	Cg-P-R	Hpcmp-R	Occpt-M-R	Rolandic-R	Putamen-R
Frt-S-L	Cg-P-L	Hpcmp-L	Occpt-M-L	Rolandic-L	Putamen-L
Frt-M-R	Prt-S-R	PrHpcmp-R	Occpt-I-R	Insula-R	Pallidum-R
Frt-M-L	Prt-S-L	PrHpcmp-L	Occpt-I-L	Insula-L	Pallidum-L
Frt-I-Op-R	Prt-I-R	Amygdala-R	Fusiform-R	Cg-A-R	Thalamus-R
Frt-I-Op-L	Prt-I-L	Amygdala-L	Fusiform-L	Cg-A-L	Thalamus-L
Frt-I-T-R	SMargl-L	Calcarine-R	Temp-P-S-L	Cg-M-R	Heschl-R
Frt-I-T-L	Angular-R	Calcarine-L	Temp-M-R	Cg-M-L	Heschl-L
Frt-S-M-R	Angular-L	Cuneus-R	Temp-M-L	SMargl-R	Temp-S-R
Frt-S-M-L	Precuneus-R	Cuneus-L	Temp-P-M-R	Caudate-R	Temp-S-L
	Precuneus-L	Lingual-R	Temp-P-M-L	Caudate-L	
		Lingual-L	Temp-I-R		
		Occpt-S-R	Temp-I-L		
		Occpt-S-L			

Central	**Orbital-Frontal**	
PreC-R	Frt-S-Ob-R	Frt-M-O-R
PreC-L	Frt-S-Ob-L	Frt-M-O-L
SMA-R	Frt-M-Ob-R	Rectus-R
SMA-L	Frt-M-Ob-L	Rectus-L
PostC-R	Frt-I-Ob-R	Temp-P-S-R
PostC-L	Frt-I-Ob-L	
ParaC-R	Olfactory-R	
ParaC-L	Olfactory-L	

Chapter 9

A Unified Optimization Approach for Diffusion Tensor Imaging Technique

Diffusion weighted imaging techniques including DTI and various HARDI methods demand a much higher signal-to-noise ratio (SNR) than that of conventional MR imaging sequences in order to provide accurate diffusion measures for quantitative evaluation of the underlying diffusion property and tractography. Therefore, extensive effort has been devoted to optimizing the experimental design of these techniques (253-258). In this Chapter, we present a unified DTI optimization approach based on our published paper "A Unified Optimization Approach for Diffusion Tensor Imaging Technique" (259), which partly resolve the problem of an overall optimal design of DTI experiment. Further optimization of HARDI techniques for better resolving the crossing fiber orientations are also extremely important and deserve further work.

9.1 Introduction

Diffusion tensor imaging (DTI) has become an invaluable non-invasive imaging tool to provide insights into the microstructural integrity of white matter. While its clinical utility has largely been demonstrated, DTI demands a much higher signal-to-noise ratio (SNR) than that of conventional MR imaging sequences in order to provide accurate and quantitative diffusion measures. Therefore, extensive effort has been

devoted to optimizing DTI (37), in an attempt to improve the accuracy and precision of tensor estimation. These optimizations include the choices of imaging parameters (253-258, 260-263), the approaches through which tensors are estimated (36, 264, 265), and the design of diffusion gradient directions (266-268). While intriguing results have been reported, demonstrating the improved tensor estimations using these optimization approaches, all of the existing approaches thus far have separately optimized different aspects of DTI such as imaging parameters or gradient directions alone. Given the fact that all aspects of a DTI experiment, including image acquisition as well as methods for tensor calculations will affect the accuracy of tensor estimates, it is thus highly desirable to having a unified approach where the essential aspects of DTI are optimized simultaneously. In addition, one of the main assumptions of the existing optimization procedures is that all tensors are uniformly distributed in a sphere. While this assumption is valid for most of the applications, in some cases, i.e. in the pediatric brain, only the major white matter fibers are well myelinated, leading to a non-uniform distribution of these major fibers (Fig.9.1). As a result, a uniformly distributed diffusion gradient scheme may no longer be the most efficient scheme to provide accurate measures of tensors. Recently, Peng and Arfanakis (269) proposed an approach where the prior directional information of selected fiber tracts was incorporated in the design of the diffusion gradient orientations. A significant reduction of the standard deviation of FA was obtained with their approach, underscoring the importance of considering the prior information. Nonetheless, similar to other existing DTI optimization approaches, only the design of the gradient directions was considered.

In this study, we propose a unified optimization approach that simultaneously optimizes most of the essential imaging parameters, including gradient separation/duration, TE, read-out time, and b-values, and gradient orientations either with or without considering the prior information of fiber distributions. In addition, the means through which tensors are calculated is also considered in the optimization procedures. Monte-Carlo simulations were performed to evaluate the performance of the proposed method. Simulation results demonstrate that our approach provides similar results to that reported in the literature when fibers are uniformly distributed while outperforming the existing methods when fibers are not uniformly distributed.

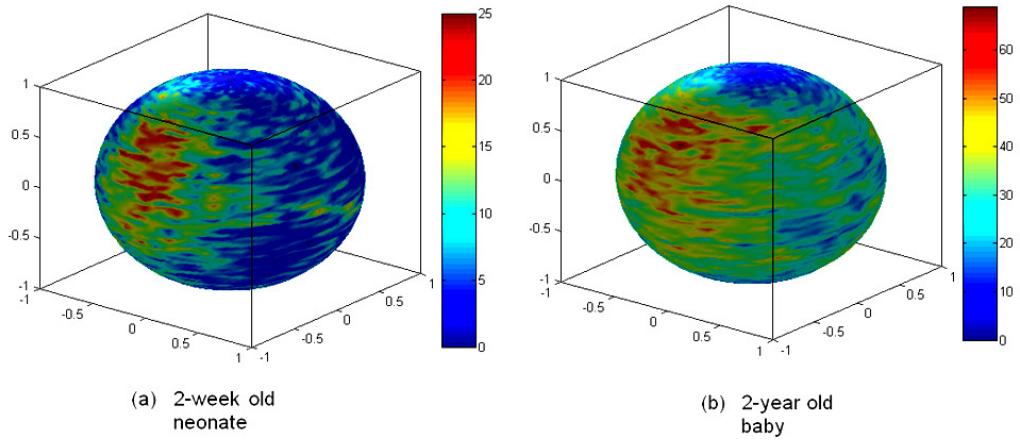

Figure 9.1. Examples of fiber distribution patterns in a neonate (a) and a 2-year old baby (b) are shown. Fiber orientations are obtained using voxels with a FA larger than 0.3 in the 2-week old neonate and 0.4 in the 2-year old baby based on a 6 direction DTI experiment and visualized on a sphere representing the 3D directions. Color codes represent number of fibers in a specific orientation block (4^0 span in azimuth angle and 2^0 span in elevation angle).

9.2 Method

In this section, the formulation of the optimization criteria, the optimization procedures, and the information on simulation/evaluation parameters are provided.

9.2.1 Design criteria

Assuming the SNR is moderately high, a Gaussian distribution instead of the Rician distribution (270) can be employed to model MR signal. With a pulsed gradient spin echo experiment, the MR signal with the diffusion tensor and weighting matrix can be written as:

$$S = S_0 \exp(-br^T D_0 r) + \eta \,, \tag{9.1}$$

where S is the measured signal, S_0 is the expected baseline signal intensity, r is the unit vector representing one gradient direction, and b is the scalar value of gradient weighting strength. Moreover, η represents Gaussian noise with a zero mean and a variance of σ_η^2 and D_0 represents (262) the true tensor. Taking the logarithm of both sides of Eq. (9.1) leads to $\ln(S(\tilde{b})) = \ln(S_0) - br^t D_0 r + \ln(1 + \frac{\eta}{\langle S(\tilde{b}) \rangle})$. Subsequently, taking Taylor expansion of the last term and neglecting the higher order terms, we can obtain:

$$\ln(S) = \ln(S_0) - br^T D_0 r + \varepsilon, \tag{9.2}$$

where $\varepsilon = \frac{\eta}{\langle S \rangle}$ and $\langle S \rangle = S_0 \exp(-br^T D_0 r)$.

Thus, $\ln(S)$ is approximately normally distributed with a mean of $\ln(S_0) - br^T D_0 r$ and variance $\sigma_\varepsilon^2 = \frac{\sigma_\eta^2}{\langle S \rangle^2}$ for moderate to large $\langle S \rangle / \sigma_\eta$ (271, 272). Eq. (9.2) can be rewritten using a matrix formulation as:

$$\vec{Y} = X \cdot \vec{\beta} + \vec{\varepsilon} \,, \tag{9.3}$$

where $\vec{Y} = [\log(\tilde{S}_1), \log(\tilde{S}_2), ...\log(\tilde{S}_n)]^T$ represents the measured signal intensities, *n* is the total number of acquisitions at each voxel and $\vec{\beta} = [\log(S_0), (D_0)_{11}, (D_0)_{12}, (D_0)_{13}, (D_0)_{22}, (D_0)_{23}, (D_0)_{33}]^T$. In addition, the i-th row of the design matrix $\vec{X}$ has the form of $(1, -b_i r_{i1}^2, -2b_i r_{i1} r_{i2}, -2b_i r_{i1} r_{i3}, -b_i r_{i2}^2, -2b_i r_{i2} r_{i3}, -b_i r_{i3}^2)$. The unbiased least squares (LS) estimator of $\vec{\beta}$ is $\tilde{\beta}_{LS} = (X^T X)^{-1} X^T \vec{Y}$, and its corresponding covariance matrix is

$$\sum \beta_{LS} = (X^T X)^{-1} (X^T \sum \varepsilon X)(X^T X)^{-1} \tag{9.4}$$

where $\sum_\varepsilon$ is the covariance matrix of ε. Assuming the signal intensities are independent,

$$\sum \beta_{LS} = (\sum_{i=1}^{n} X_i^T X_i)^{-1} \cdot (\sum_{i=1}^{n} X_i^T X_i \frac{\sigma_\eta^2}{\left\langle S(\tilde{b}) \right\rangle^2})(\sum_{i=1}^{n} X_i^T X_i)^{-1} \,. \tag{9.5}$$

By defining $Z_i^T = [-b_i r_{i1}^2, -2b_i r_{i1} r_{i2}, -2b_i r_{i1} r_{i3}, -b_i r_{i2}^2, -2b_i r_{i2} r_{i3}, -b_i r_{i3}^2]$ and $\theta = [(D_0)_{11}, (D_0)_{12}, (D_0)_{13}, (D_0)_{22}, (D_0)_{23}, (D_0)_{33}]$, Eq. (9.5) can be written as

$$\sum \beta_{LS} = \frac{\sigma_\eta^2}{S_0^2} (\sum_{i=1}^{n} X_i^T X_i)^{-1} \cdot (\sum_{i=1}^{n} X_i^T X_i \exp(-2Z_i^T \theta))(\sum_{i=1}^{n} X_i^T X_i)^{-1} \tag{9.6}$$

It should be noted that the same procedures can be used to derive criteria for weighted least squares estimation (36, 272) as outlined in Appendix B.

9.2.2 Incorporating imaging parameters

In the previous section, we derived the design criteria for tensor estimation. In this section, procedures on how imaging parameters can be integrated into Eq. (9.6) will be outlined. A sequence structure (Fig.9.2) similar to that illustrated in Alexander and Barker (258) was employed in our study, although slight modifications were made to

accommodate our optimization process. The durations of the 90^0 and 180^0 pulses were P90 and P180, respectively, δ was the diffusion gradient duration, Δ was the time interval between diffusion gradients, and R and RH were the readout time before and after the echo, respectively. Assuming a fixed image resolution, RH would be fixed and independent of other parameters. Four time intervals, τ1, τ2, τ3, and τ4 were included. The durations of these four time intervals along with P90 and P180 were considered fixed based on the hardware constraints and were independent of other imaging parameters.

The echo time TE was then defined as

$$\text{TE=P90/2+ } \tau_1 + \Delta + \delta + \tau_4 + R \,, \tag{9.7}$$

and the applied b-value was given by

$$b = t \cdot \delta^2 \gamma^2 |g|^2 \,, \tag{9.8}$$

where γ is the gyro-magnetic ratio, g is the gradient strength, $t = \Delta - \frac{\delta}{3}$ is the "effective" diffusion time under the assumption of rectangular gradient pulses and the Gaussian density function of particle displacements (273).

We assume that the expected baseline intensity S_0 is given by

$$S_0 = P_0 \exp(-TE/T2) \,, \tag{9.9}$$

and

$$SNR \propto (R + R_H)^{1/2} \,, \tag{9.10}$$

where P_0 depends on the intrinsic signal of the tissue (spin density). If we further assume that the underlying noise is constant, then the SNR can be incorporated into S_0 as follows:

$$S_0 = P_0 \exp(-TE/T2)(R + R_H)^{1/2} \,. \tag{9.11}$$

Substituting Eq. (9.11) in Eq. (9.6) yields

$$\sum_{\beta_{LS}} = (\frac{P_0^2 \exp(-2TE/T2)(R_H + R)}{\sigma_\eta^2})^{-1} (\sum_{i=1}^{n} X_i^T X_i)^{-1} \cdot (\sum_{i=1}^{n} X_i^T X_i \exp(-2Z_i^T \theta))(\sum_{i=1}^{n} X_i^T X_i)^{-1} . \quad (9.12)$$

Notice the gradient directions are represented in the X and Z matrices. This formulation incorporates most of the important imaging parameters together with the LS approach for tensor estimation and diffusion gradient directions. The trace of $\sum_{\beta_{LS}}$ was then used as the cost function for the following optimization procedures. The main justification for the use of Eq. (9.12) as the cost function for subsequent optimization is due the fact that the main goal of our study is to improve the accuracy and precision of tensor estimates which can be characterized by the bias and covariance of the estimated DT. Therefore, it is common in the field of experimental design to choose the covariance matrix of the estimated DT when the bias of the estimated DT is small (274, 275). Nevertheless, although the trace of the covariance matrix is used in our approach, other measures such as the determinant or smallest eigenvalue are also eligible for this purpose.

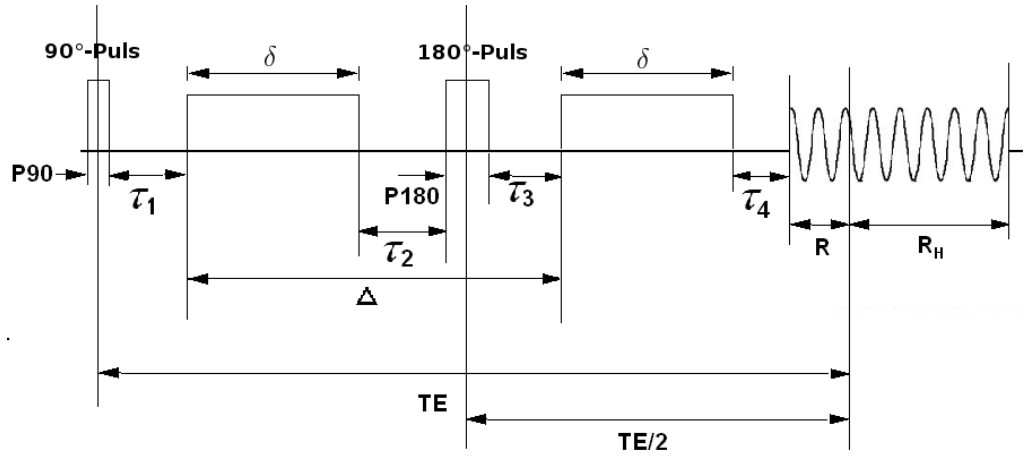

Figure 9.2. The pulsed-gradient spin-echo (PGSE) sequence diagram is shown.

9.2.3 Optimization

The incorporation of fiber orientations into the optimization processes for DTI imaging parameters, gradient directions, and LS tensor estimation is one of the main motives of the present study. Once the values of Δ and R are chosen, the values of δ, TE and b-values can be calculated according to P90, P180, R_H , τ_1, τ_2, τ_3, and τ_4. By further choosing the gradient direction vectors and incorporating the tensor field information, the covariance matrices represented by Eq. (9.12) can be fully determined, allowing the minimization of the cost function – the trace of covariance matrix.

A simulated annealing algorithm (276) was used to minimize the cost function. The optimization procedures are described below.

a) Setting values of P90, P180, R_H, τ_1, τ_2, τ_3, and τ_4 according to the hardware limitations (P90=0.005s; P180=0.004s; τ_1, τ_2, τ_3, and τ_4 =0; Gradient Strength: 40 mT/m; readout time after echo=0.0338s according to our 3.0-T MR imaging unit (Allegra; Siemens Medical Systems, Erlangen, Germany)). T2 was set to be 0.08s.
b) Initializing values of Δ, R and gradient direction vectors which were represented by Nx3 (*N*: number of gradient directions) matrix and were independently simulated from the standard Gaussian distribution.
c) Calculating the values of δ, TE and b-value, respectively.
d) Calculating the covariate matrix as in Eq. (9.12) for each prior DT and then summing the trace of matrices for all DTs in the corresponding tensor field as the cost function values.
e) Updating values of Δ, R and gradient direction vectors according to the random-walk Metropolis algorithm.

f) Repeating the steps c)-e) until the stopping criteria were met.

g) After optimization, the values of Δ, R, δ, TE, b-value and gradient direction vectors that provided the minimal cost function values (minimum×(1+5%)) were defined as the optimal values. Detailed descriptions of the simulated annealing algorithm are given in Appendix A.

9.2.4 Simulation

In this section, parameters for Monte Carlo simulation and how simulated DW images were obtained are provided.

Prior-Knowledge of fiber directions

Three different fiber distributions as represented by the corresponding tensor fields were simulated as prior information: I) CONE1 – fibers orientated in 1 cone area (50 tensors orderly oriented within a diverging angle of 20^0); II) CONE3 – fibers orientated in 3 well separated cone-like areas (50 tensors in each cone and the diverging angle for each cone was 20^0); and III) UNIF – uniformly distributed fibers (100 tensors with random orientations) (Fig.9.3). In each of the tensor fields, a "rice-shaped" diffusion tensor $D = diag(\lambda_1, \lambda_2, \lambda_2)$ with $\lambda_1 = 1.7 \times 10^{-9} m^2 s^{-1}$ and $\lambda_2 = \lambda_2 = 0.2 \times 10^{-9} m^2 s^{-1}$ was selected and different fiber orientations were generated using a rotation around the z axis $D = R^T(\alpha,\phi) diag(\lambda_1, \lambda_2, \lambda_2) R(\alpha,\phi)$, where $R(\alpha,\phi)$ represents the rotation matrix defined by azimuth angle α and elevation angle ϕ.

Three different imaging acquisition schemes were tested, including DIFF6 – M=1/N=6; DIFF12 – M=2/N=12, and DIFF30 – M=5/N=30 for each prior tensor field where M and N are the numbers of b=0 and diffusion weighted images (b>0), respectively.

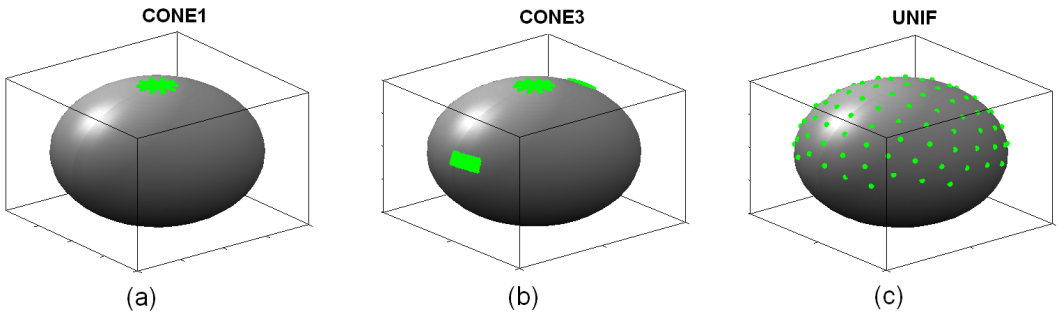

Figure 9.3. Simulations of three different fiber distributions, including (a) a single fiber cone area with 50 fibers, (b) three fiber cone areas with 50 fibers in each cone and (c) the uniform fiber case with 100 randomly distributed fiber orientations.

Reconstruction

The expected baseline signal intensity S_0 was computed from Eq. (9.11) assuming a constant spin density P0. The "ideal" DW signals were then calculated from $\langle S \rangle = S_0 \exp(-br^T D_0 r)$ for each of the corresponding prior tensor fields. Constant complex noise with independent real and imaginary parts each with a normal distribution ($\mu/\sigma = 0/2$) was added to S_0 and $\langle S \rangle$ separately and the magnitude was then calculated to obtain the synthetic measurement for the baseline image intensity and diffusion weighted image intensity, respectively. By assuming a constant noise level, four different P_0 levels [250, 450, 600, 800] were tested to simulate different SNRs. Finally, DTs were reconstructed using LS estimation. This process was repeated 100 times for each experimental setting.

Performance indices

To assess the performance of the proposed optimization procedures, the bias ($B(D)$) and the standard deviations (σ(D)) of the tensor elements, the standard deviation of reconstructed FA ($\sigma(FA)$) and Mean Angular Difference (MAD) (277) of the reconstructed principle eigenvectors were employed. Detailed information on these four parameters is provided below.

- $B(D)$: In each experimental setting, the square error of each DT element was calculated by subtracting the estimated values from the true tensor elements. The square errors of the six independent elements were then added together and averaged over all trials and all experimental settings to obtain a scalar value at each SNR and b-value to assess the accuracy of tensor estimation.
- $\sigma(D)$: Standard deviations of the six independent elements across 100 trials were summed together and averaged over all experimental settings to assess the precision of tensor estimation.
- $\sigma(FA)$: Standard deviations of FA values across 100 trials were averaged over all experimental settings to assess the precision of FA estimation.
- MAD: The MAD was calculated using the following formula (Landman et al., 2007) for each experimental setting: $MAD = \frac{1}{N}\sum_{i=1}^{N}\cos^{-1}(PEV_i \bullet PEV_{tr})$ where N=100 for 100 trials, PEV_i is the reconstructed principle eigenvector of each experimental setting and PEV_{tr} is the "true" principle eigenvector.

9.3 Evaluation of optimal imaging parameters and gradient directions

For each optimization set, an optimal b-value range was obtained as outlined in the optimization section together with the corresponding Δ, R, δ and TE values. To

validate this optimal b-value range, a series of 11 different b-values (Appendix A) together with the corresponding Δ, R, δ, TE and gradient directions were tested through the reconstruction process to produce performance indices at each specific b-value, which provided the comparison across different b-values and hence the validation of the proposed optimal ranges.

In order to determine the performance of the optimal gradient directions in the presence of prior knowledge of the tenor fields, a direct comparison was made between the optimized diffusion gradient directions obtained using the proposed approach and the conventional gradient scheme based on the minimal energy method as proposed by Jones et al (254). For each comparison, the prior tensor field was considered as the "true tensor field." To ensure a fair compassion between the proposed and the conventional scheme, all imaging parameters including b-value were kept identical. The four performance indices as outlined above were employed to compare the two optimization approaches of diffusion gradient directions. In addition, an improvement ratio (performance of the proposed optimization scheme/performance of the conventional scheme) was also calculated.

In order to further assess the directional sensitivity of the proposed gradient scheme, another synthetic tensor field which consisted of 10000 uniformly distributed "test samples" on the sphere was also simulated. The proposed optimization and conventional schemes were used to perform reconstruction at a specific b-value based on this "true" tensor field so that their directional performance can be compared.

9.4 Results

9.4.1 Optimal Δ, R , TE, and b-value

Fig. 9.4 shows the optimal b-value ranges for all combinations of tensor fields and gradient directions. In the UNIF case, the optimal b-value ranges between $0.7\times10^{9}\,s/m^{2}$ and $1.0\times10^{9}\,s/m^{2}$ independent of the number of diffusion gradient directions, consistent with that reported by Alexander and Barker (258) for one fiber case. In contrast, the optimal ranges become both wider and higher for CONE3 and CONE1.

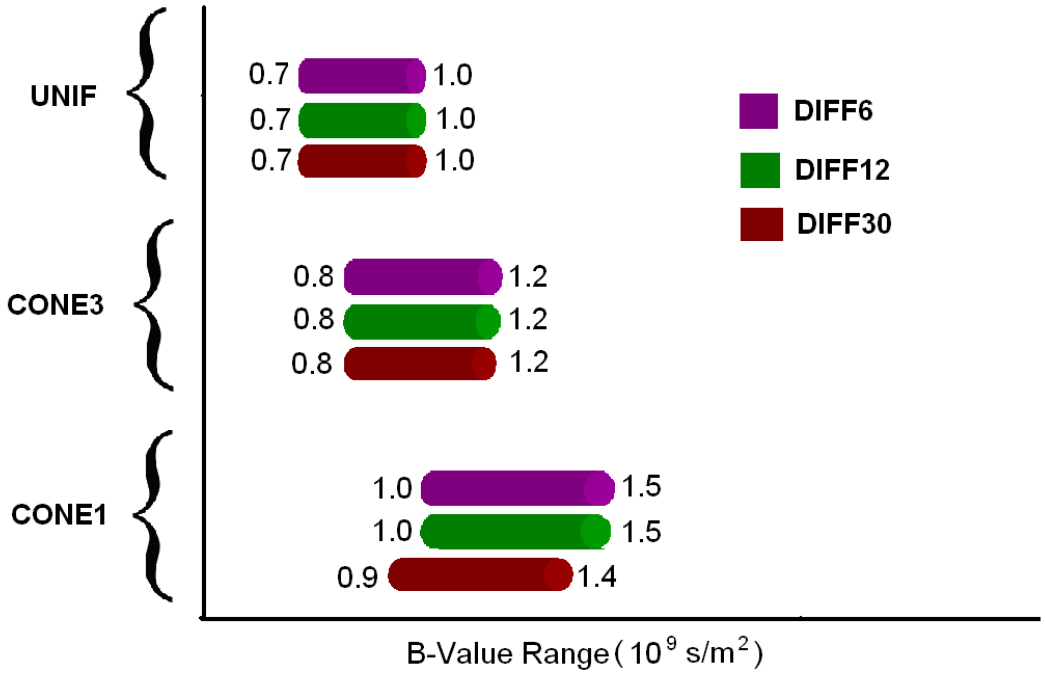

Figure 9.4. Optimal b-value ranges defined by the proposed scheme. CONE1: one cone area; CONE3: three cone areas; and UNIF: uniform fiber case. DIFF6: M/N=1/6, DIFF12: M/N=2/12, DIFF30: M/N=5/30.

Table 9.1 lists the optimal values of Δ, R, and TE (rounded to ms) at the optimal b-value (rounded at 0.1 $\times10^{9}\,s/m^{2}$) which corresponds to the lowest cost function value (the center of the optimal range) of all three prior fiber distributions. It is evident that the optimal parameters are rather stable for each prior tensor distribution independent of the

M/N. In order to better compare our approach and that reported by Alexander and Barker (258), the optimal values calculated based on their approach are listed in parentheses at the same b-values for comparison. It is immediately apparent that the optimal Δ, R, and TE are consistent between both approaches.

The four performance indices with DIFF6 and CONE1 for different SNR are shown in Fig.9.5. The two dotted lines indicate the ranges of the optimal b-values as shown in Fig.9.4. With the exception of σ(FA), the optimal b-value ranges coincide with the "valley" of the $B(D)$, $\sigma(D)$ and MAD curves, demonstrating the effectiveness of the proposed optimization approach which yields reduced biases and SD of tensors and improved accuracy of the estimates of tensor directions. However, the optimal b-value range for FA appears slightly higher than that obtained using the proposed optimization approach. This finding is reasonable since our optimization criteria are based on the variance properties of the six independent tensor elements rather than FA, and a more specific criterion may be needed if one is particularly interested in FA estimation. Similar findings were also reported by Alexander and Barker (258) where they showed that the optimal b-value for FA estimation is higher than that for fiber orientation estimation.

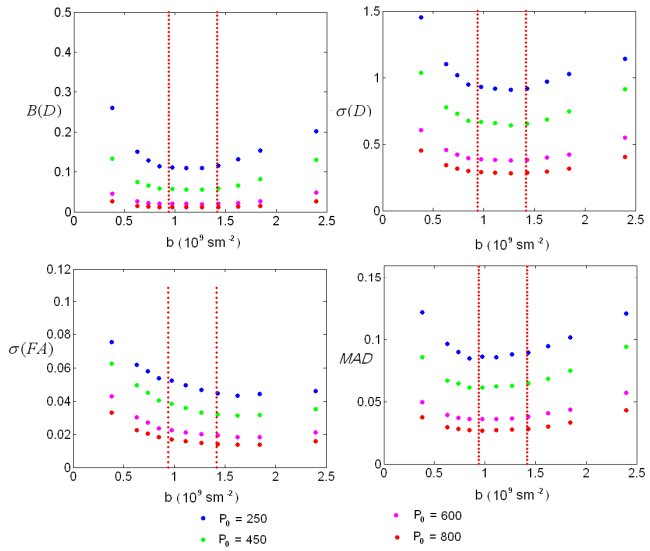

Figure 9.5 Results of the four performance indices: Bias of **D-** $B(D)$, standard deviation of **D-** $\sigma(D)$, standard deviation of FA - $\sigma(FA)$ and mean angular difference-MAD for DIFF6 and CONE1. X-axis represents b-value in $10^9 s/m^2$, y-axis represents the corresponding performance indices values. Red lines indicate the optimal b-value ranges defined by the proposed optimization scheme.

9.4.2 Optimal diffusion gradient directions

Fig.9.6 demonstrates the diffusion gradient directions using the conventional and the proposed optimization schemes, respectively. As expected, the conventional scheme results in a highly uniform coverage of the entire sphere (Fig. 9.6a). However, the gradient scheme using the proposed method shows a very different pattern especially in CONE1 (Fig. 9.6b) and CONE3 (Fig. 9.6c), respectively. In CONE1, the optimized gradient directions exhibit an orderly pattern around the direction of the prior tensor field (red points). Similarly, although the gradient directions spread out, they maintain an orderly pattern around the three tensor fields (red points) in CONE3. Finally, the optimized diffusion gradient directions for UNIF (Fig. 9.6d) using our approach resemble

that obtained using the conventional scheme (Fig. 9.6a); the gradient directions are uniformly distributed across the sphere.

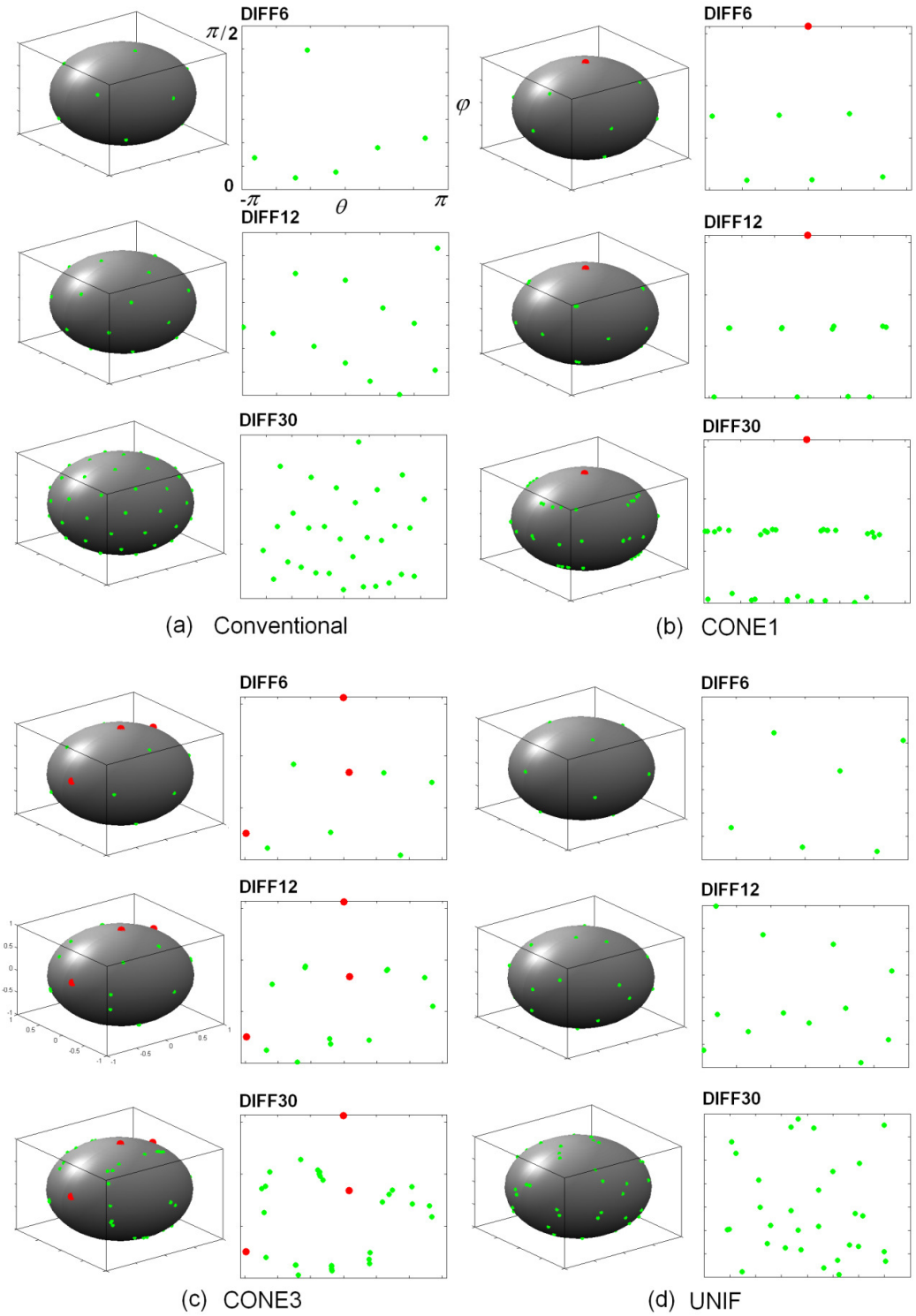

Figure 9.6. Diffusion gradient orientations are shown for the conventional scheme (a) and the proposed optimization scheme in CONE1 (b), CONE3 (c) and UNIF (d), respectively. Red points represent the center directions of the predefined fiber distributions (CONE1 and CONE2). Green points are the orientations of the diffusion gradients. In each panel, the diffusion gradient directions are plotted on a spherical coordinate with azimuth angle θ (X-axis) ranging from $-\pi$ to π and elevation angle φ (Y-axis) from 0 to $\pi/2$.

9.4.3 Comparison of Optimal and Conventional Gradient direction schemes

The improvement ratios (proposed/conventional schemes) for all four performance indices in CONE1 (Fig. 9.7a), CONE3 (Fig. 9.7b) and UNIF (Fig. 9.7c) conditions with P_0=450 (which corresponds to a SNR~30 in our simulation) are shown. The proposed optimization scheme substantially reduces the bias (B(D)) and standard deviation (σ(D)) of the tensors by ~40% - 60% and ~20-30%, respectively within the optimal b-value range (red lines) for CON1 (Fig. 9.7a). It appears that these improvements are independent of the number of diffusion gradients. In contrast, although the proposed scheme remains superior to that of conventional approach, the extent to which σ(FA) and MAD are improved depends on the number of diffusion gradients. Specifically, the largest improvement is observed with DIFF6 (~50%), followed by DIFF12 and DIFF30 for σ(FA) at a b-value of $1.2\text{x}10^9 \text{s/m}^2$. For MAD, a comparable performance is observed between the optimized and the conventional schemes with DIFF6 while a 30% improvement is observed for DIFF12 and DIFF30, suggesting that it is imperative to employ more than 6 diffusion gradient directions in order to obtain an accurate estimate of tensor directions. Comparing to CONE1, the

degree of improvements for CONE3 is reduced for both B(D) and σ(D) (Fig. 7b). In addition, the improvement is minimal for $\sigma(FA)$ and MAD (within 5%). Finally, the performance is comparable for all four measures between the proposed and conventional schemes in UNIF condition (Fig 9.7c).

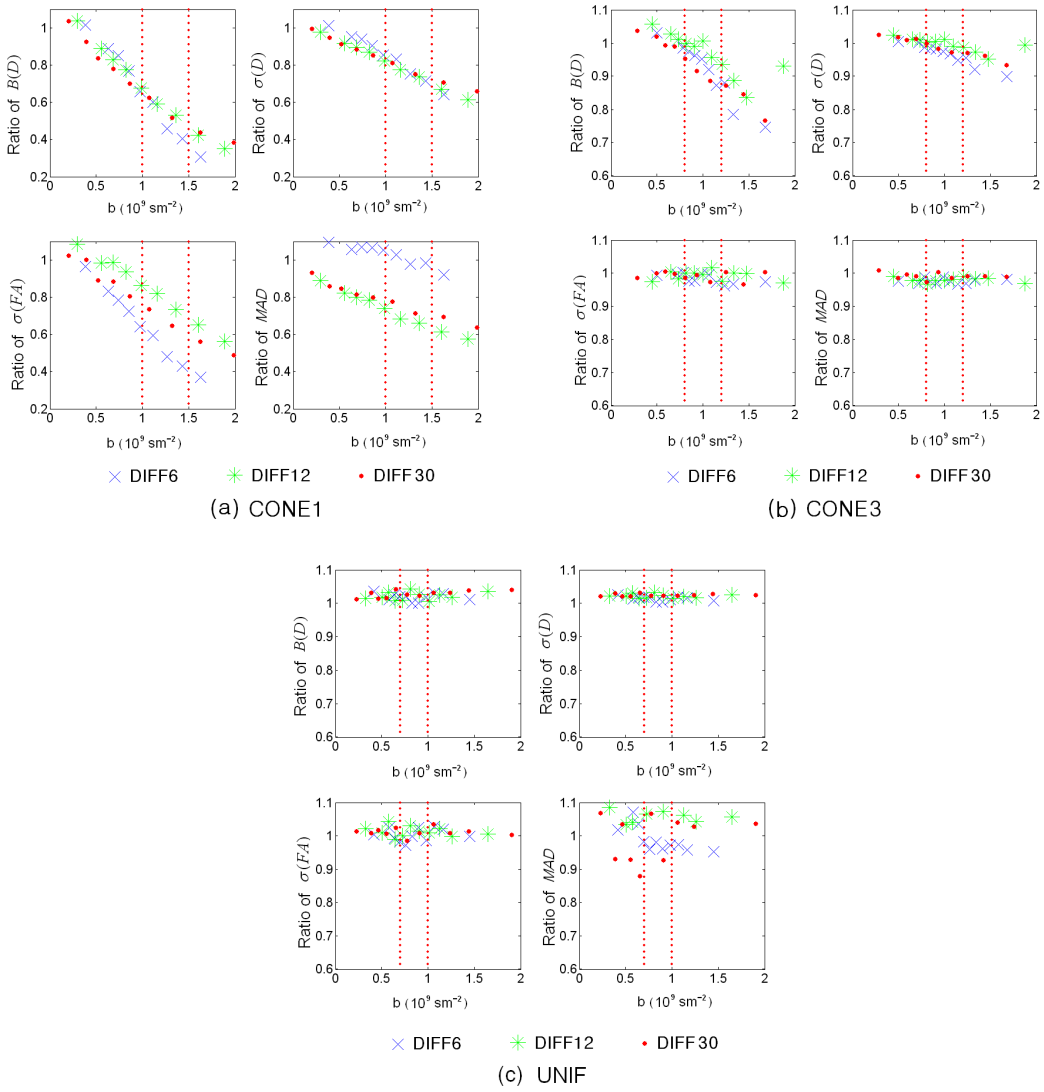

Figure 9.7 Improvement ratios of the four performance indices are shown for CONE1 (a), CONE3, and UNIF (c), respectively, where P_0=450. X-axis represents b-value in $10^9 s/m^2$ and Y-axis represents the performance indices values. Dashed red lines

indicate the rages of optimal b-value using the proposed optimization approach. Blue crosses, green asterisks, and red filled circles represent DIFF6, DIFF12, and DIFF30, respectively.

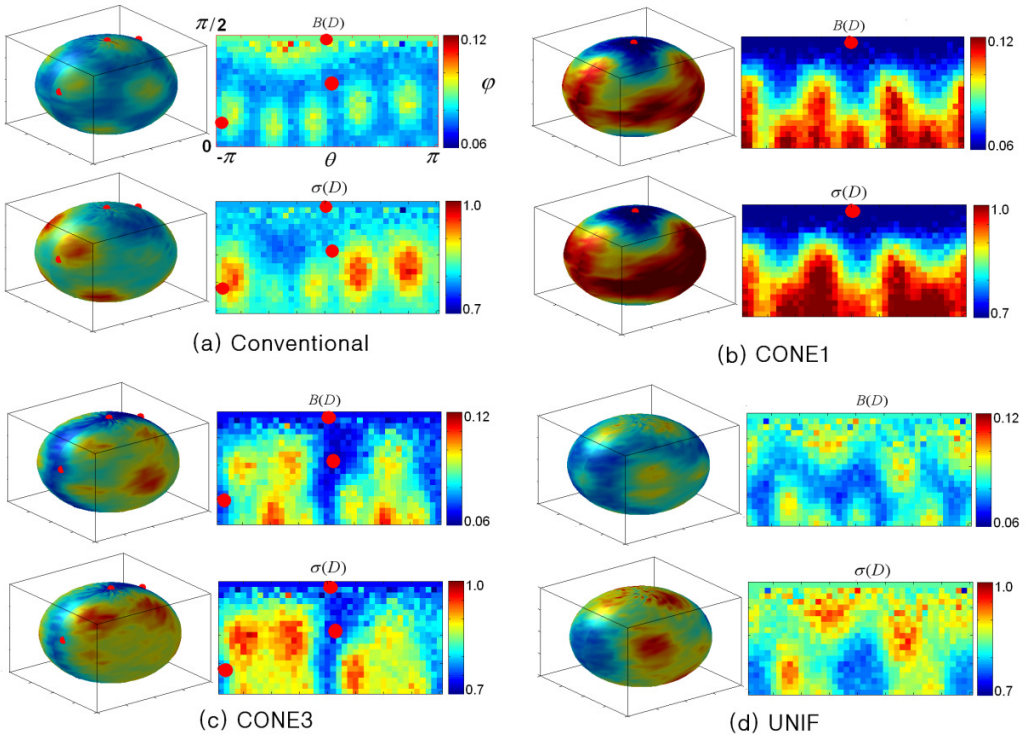

Figure 9.8 Comparison of the directional sensitivity of different schemes (M/N=1/6, b-value=1*10^9 s/m^2, P_0=450) are shown for conventional scheme (a) and the proposed optimization approach for CONE1 (b), CONE3 (c), and UNIF (d), respectively. In each panel, the first row shows the spatial distribution of $B(D)$ and the second row is $\sigma(D)$. Red points represent the center of the prior fiber distribution (CONE1 or CONE3). In each panel, the performance values are plotted on a spherical coordinate with azimuth angle θ (X-axis) ranging from $-\pi$ to π and elevation angle φ (Y-axis) from 0 to $\pi/2$.

The comparison of directional sensitivity between all three different fiber distributions is shown in Fig 9.8 for DIFF6. As expected, the directional dependence of

both bias and precision of tensors are apparent for all schemes. A decreased bias as well as standard deviation of the tensors are observed using the proposed scheme for both CONE1 (Fig. 9.8b) and CONE3 (Fig. 9.8c), suggesting that the optimized diffusion gradient scheme offers a better estimate of the tensors around the fiber distributions. Nevertheless, it is not surprising that both the bias and standard deviations of the tensors are increased away from the cones. Finally, Fig. 9.8d exhibits no obvious improvements between the proposed and the conventional scheme since both schemes are optimized for a uniform fiber distribution. Similar patterns were observed for both DIFF12 and DIFF30.

9.5 Discussion

Most of the existing optimization methods for DTI have separately considered different aspects of a DTI experiment, including either sequence parameters such as gradient duration/separation, read-out time, TE, and b-values (253-258), diffusion gradient orientations (266-269), or the post-processing schemes for tensor estimations (36, 264, 278). While these approaches have yielded improvements on the parameters that were targeted to be optimized, they are prone, potentially, to be trapped in local minima when the cross-talk effects are difficult to be dealt with. Therefore, an approach capable of simultaneously optimizing most of the essential aspects of a DTI experiment is highly desirable. In this study, we proposed a unified optimization approach for DTI to simultaneously consider imaging parameters, fiber distributions and methods through which tensors are calculated. To the best of our knowledge, this is the first reported approach that offers the ability to simultaneously consider most of the important aspects of DTI experiments in the optimization processes. Specifically, with the simulated annealing algorithm (Appendix A), the proposed approach simultaneously optimizes

different parameters in image acquisition (gradient duration/separation, read-out time, TE, and b-values), tensor estimation, and diffusion gradient directions by considering the prior knowledge of tensor fields while minimizing the cross-talk between all parameters so as to enhance the probability of finding the global minimum. Our results show that compared with the conventional scheme (254), the proposed optimization approach substantially reduces the biases and standard deviations of tensor estimations as well as the standard deviations of FA and MAD when a non-uniform fiber distribution prior is assumed, particularly in the CONE1 condition. In addition, our results also demonstrate that a higher and wider range of b-values can be employed without compromising the accuracy and precision of tensor estimates when the information of fiber distribution is considered in the design of diffusion gradient orientations. Finally, an extension of our approach is provided in Appendix B where the weighted least squares approach is employed for tensor estimates, demonstrating the flexibility of the proposed approach in adapting different post-processing schemes for tensor estimation.

Table 9.1

	CONE1			CONE3			UNIF		
	DIFF6	DIFF12	DIFF30	DIFF6	DIFF12	DIFF30	DIFF6	DIFF12	DIFF30
B($10^9 s/m^2$)	1.1	1.2	1.2	1.0	1.0	1.0	0.8	0.8	0.8
TE (ms)	51 (51)	52 (53)	52 (53)	50 (50)	50 (50)	50 (50)	46 (46)	46 (46)	46 (46)
Δ (ms)	27 (28)	28 (28)	28 (28)	27 (27)	27 (27)	27 (27)	25 (25)	25 (25)	25 (25)
R (ms)	<0.01 (0.4)	0.01 (1.2)	<0.01 (1.2)	0.1 (1.1)	<0.01 (1.1)	<0.01 (1.1)	<0.01 (0.2)	<0.01 (0.2)	0.01 (0.2)

Table 9.1 Optimal values of Δ, R, TE at the optimal b-value corresponding to the minimal cost function values (the center of the optimal range) of all three prior fiber distributions

9.5.1 Optimal b values

With the assumption that fibers are uniformly distributed, Alexander and Barker (258) evaluated a series of different b-values in an attempt to identify the optimal b-value ranges for tensor estimation. They found that b-values ranging between 0.7 and 1.0 $\times 10^9 s/m^2$ were optimal for fiber direction estimates in one-fiber case, consistent with the optimal range of b-values obtained using our approach in the UNIF experimental setting (Fig. 9.4). However, the optimal ranges of b-values change when the prior information of non-uniform fiber distributions was incorporated in the design of the diffusion gradients. Specifically, the optimal ranges of b-values become higher and wider for both CONE3 ([0.8, 1.2] $\times 10^9 s/m^2$) and CONE1 ([0.9, 1.5] $\times 10^9 s/m^2$). These findings suggest that by incorporating the prior information of tensor fields for optimizing the diffusion gradient directions, a higher and wider range of b-values can be used without compromising accuracy and precision, potentially facilitating diffusion spectrum imaging (279) where high b-values are needed.

9.5.2 Optimal gradient directions

It is evident that the optimized gradient schemes using the proposed approach for non-uniform fiber distributions (CONE1 and CONE3) (Fig. 9.6) exhibit a very different pattern when compared with that of using the conventional approach (Fig. 9.6) (254). With our approach, the optimized diffusion gradient directions appear to be more symmetrically distributed around the direction of the fibers (Figs. 9.6b and 9.6c). This pattern is particularly apparent in CONE1 (Fig. 9.6b) where the diffusion gradients (green points) tend to align themselves in two lines covering evenly in the elevation dimension while spanning throughout the whole range of the azimuth dimension. With these

optimized gradient direction arrangements, the accuracy ($B(D)$) and precision ($\sigma(D)$) of tensor estimates together with the estimated FAs ($\sigma(FA)$) and fiber orientations (MAD) are substantially improved when compared to that obtained using the conventional approach where a uniformly distributed tensor field was assumed (Fig. 9.7). Nevertheless, the improvement ratios decrease as the number of cones increases (Figs. 9.7a vs. 9.7b). This finding is not surprising since as the number of cones increased, it would eventually approach a uniform distribution and the advantages of incorporating prior information would be diminished (Fig. 9.7c).

It is worth pointing out that some of the optimized diffusion gradient directions using our approach appear to be very close to each other, particularly for DIFF30 (Fig. 9.6) in both CONE1 and CONE3. Although it is plausible that the imperfection of the proposed optimization approach leads to the observed pattern of the diffusion gradient orientations, the most likely explanation may be the utilization of the LS approach for tensor estimation in our study. The LS approach does not account for the noise variance and assumes equal variance. We have also performed the same optimization processes with the exception that WLS was employed for tensor estimates (Appendix B). The results demonstrate that the previously observed clustered pattern using the LS approach no longer existed (result not shown), supporting the notation that the assumption of equal variance for LS accounts for the clustered diffusion gradient directions.

9.5.3 Comparisons with an optimization approach incorporating prior information

Peng and Arfanakis (269) have recently proposed an approach to optimize diffusion gradient directions by taking into account the prior information of the fiber orientations. However, unlike our proposed approach considering most of the essential

aspects of a DTI experiment, only the $\sigma(FA)$ was employed as the criterion for optimization in their approach. Specifically, they considered fibers oriented within a 30^0 cone along the z-axis, which is similar to the CONE1 condition in our studies, allowing a direct comparison between our and Peng and Arfanakis' approaches. Fig. 9.9 shows the improvement ratios of the four performance indices for Peng and Arfanakis' approach over the conventional scheme (Fig. 9.9a) and our over Peng and Arfanakis' schemes (Fig. 9b), respectively. Since their approach specifically optimized FA measurements, it is not surprising that $\sigma(FA)$ is less than 1 with the exception of the lowest b-values evaluated when compared with those obtained using the conventional approach. In contrast, a much poorer performance for MAD is observed using Peng and Arfanakis' approach than that of using the conventional scheme. The performance for both B(D) and σ(D) is largely dependent on the b-values; Peng and Arfanakis' approach outperforms the conventional approach for b $\sim>$ 1.2 $\times 10^9 s/m^2$ or otherwise is worse than the conventional approach. Comparing the improvement ratios between our and Peng and Arfanakis' approaches (Fig. 9.9b), it is evident that with the exception of $\sigma(FA)$ where a comparable performance is observed, our approach outperforms that proposed by Peng and Arfanakis for the remaining three performance indices, underscoring the importance of optimizing the essential aspects of DTI experiments simultaneously and demonstrating the effectiveness of our approach.

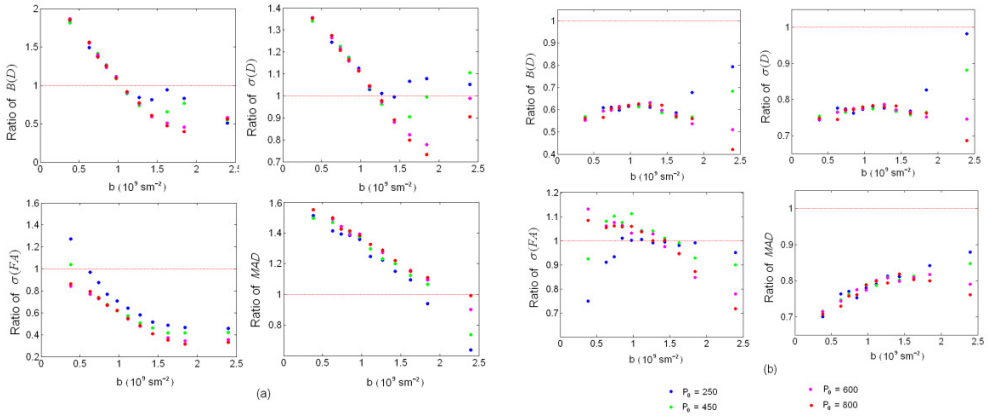

Figure 9.9 Ratios of the four performance indices between Peng and Arfanakis' over the conventional approaches (a) and the proposed over Peng and Arfanakis' approaches are shown, respectively, where results using M/N=1/6 and CONE1 are shown. X-axis represents b-value in $10^9 s/m^2$ and Y-axis represents the ratios of performance index values.

One of the major findings of our study is that the prior tensor information can be employed for the optimization of different gradient orientations so as to improve the accuracy of tensor estimates. While the directional distribution of white matter is most likely to be uniformly distributed throughout the entire sphere in adults, the directional distribution in very young pediatric subjects may have preferential directions and is non-uniform (Fig. 9.1). Under this condition, the prior tensor information should be considered in the optimization of the diffusion gradient directions. This can potentially be accomplished by building a fiber distribution atlas for each age group and from which the proposed optimization approach can be applied to form an optimal set of imaging parameters for each age group. By the same token, in the case when a specific WM tract is of interest, our optimization approach can again be applied to improve the accuracy of the DT estimates of the specific fiber tracts.

Another advantage of our approach is the flexibility of incorporating different DT post-processing approaches into the optimization framework. This flexibility is important considering different estimation methods may become necessary in different conditions. For example, in the case of a low SNR ratio, the Gaussian assumption of MR signal will no longer hold. The expectation of such a "log Rician" distribution could deviate from the real signal intensity, which may lead to systematic biases using the least square estimates (Salvador et al. 2005). In this case, either weighted least square (WLS) estimation (Basser et al., 1994, Zhu et al., 2007) or maximum likelihood estimation of the Rician model (280), (281) can be applied to minimize or correct for this distortion. As demonstrated in Appendix B, the proposed optimization framework can be easily adapted to the WLS approach by modifying the covariance matrix of the estimated DT, demonstrating the potential wide applicability of the proposed approaches.

Finally, while the proposed approach enables the simultaneous optimization of a variety of imaging and DTI parameters, including gradient duration/separation, read-out time, TE, b-value and diffusion gradient directions, these parameters do not include all aspects of a DTI experiment. Both theoretic analysis and experimental tests have been performed to study the effects of the number of diffusion-encoding gradient directions (282) (283) (277) (284), the ratio of M (base line image) and N (diffusion weighted images) (263) and the size/shape of imaging voxels (285). Although it is feasible to potentially incorporate these additional parameters into a more generalized optimization framework, further studies will be needed.

Chapter 10

Conclusions and Future Directions

The study of human brain functional development is of paramount importance not only in improving our understanding of the functional mechanisms underlying the mature brain but also providing essential age-specific information for critical assessment and monitoring of both normal and abnormal brain development (33-35). The primary goals of this dissertation are to delineate the functional development trajectory during the critical first two years' of life and the growth pattern of a variety of different measures ranging from regional interactions to global economic properties as well as the structural underpinnings.

Structurally, we found that WM exhibits a rapid growth during the first year followed by a much slower but steady growth during the second year of life, supporting the essential role of the first postnatal year in structural brain development. Moreover, we found that WM development starts from the central part of the brain (corpus callosum) and gradually propagates to peripheral regions, revealing an interesting spatial pattern of structural development. These significant WM developments during the first two years of life build or strengthen necessary short-/long-range structural connections between different brain regions and provide structural basis for functional development, especially connectivity development.

Functionally, by focusing on one of the most important networks - the "default-mode" network, we demonstrated interesting developmental trajectories regarding both its anatomical covering and functional wiring. Specifically, we found that a primitive default network emerges in neonates but this network covers only the hub regions of the typical adult default network (among other "non-typical" default regions) and is only sparsely connected. Till 1-year-old, the network becomes much more extensive and demonstrates an almost full coverage of all default network regions. In contrast, the default network at 2 years of age becomes similar to that in adults. A consistent pattern for all 3 age groups is the involvement of "non-typical" regions in this network, including occipital/parietal regions in neonates, parietal/superior temporal/anterior cingulate regions in 1yr olds and parietal/inferior temporal regions in 2yr olds, which is consistent with the notion that infant brain often employs a larger area of cortex than those used in adults in performing similar tasks (108) and reinforces the importance of functional specialization to achieve matured functional architecture. Another important finding is the demonstration of the potential hubs of the default network – MPFC and PCC – even in pediatric subjects. As functional roles of the hubs in adult mature default network are well documented, the observation of these two hubs in such young pediatric subjects is more elusive but potentially implies early development of their corresponding functions, which is consistent with the previous reports regarding the development of "self-awareness" (120) as well as episodic memory functions (115, 118).

Going beyond specific networks and focusing on the functional development at the whole brain level offers an overall picture depicting the global functional growth pattern. In this project, extensive inter-regional connection development involving both

synchronization and specialization, dramatic modular structure reorganization, shifts of hub regions, as well as significant improvement of small-world properties are observed during the critical first year. However, the second year witnesses much fewer functional changes but still demonstrates important consolidating, fine-tuning, as well as "bridging" roles through the emergence of intermediate structures. Finally, the adult functional organization is more consistent with the known brain functions. Summarizing the findings from this whole brain developmental examination reveals that the brain develops from more locally clustered to more remotely integrated, from more anatomically constrained to more functionally sensible, and from more sensory-function-directed to more cognitive-function-oriented, implying important principles underlying global functional brain development.

Another important finding in this dissertation is the documentation of the mediating role of the frontal-parietal system on the anti-correlation between two opposing systems: the default and the dorsal attention systems. Converging evidence on this role was derived from regional interactions as well as network level interactions based on the newly developed multivariate approach, strongly supporting the importance of this mediating role in both the maintenance of specific brain state as well as successful transition to different task states. Although this exploration was done in adult subjects, future study is on schedule to examine the developmental process of this mediating role during early years of life.

The interplay of structural and functional development is another important area that deserves future efforts. Different models for the combined developmental process have been proposed including "predetermined epigenesis", which assumes that

there is a unidirectional causal chain from genes, structural changes to psychological function and “probabilistic epigenesis”, which assumes bidirectional interactions between genes, structural brain development and psychological function (108). These are questions of central importance to understand the brain development principles. With our unique pediatric data, we are granted a great opportunity to tackle this problem. Our preliminary results (not shown) seem to suggest that their mutual dependence declines as age grows on a system level. Future efforts are definitely needed to tackle this problem in more depth and details to delineate the interesting interplay between these two channels during development.

Another interesting question regarding the effects of gene or environment on the functional brain development is also of great interest and future efforts will also be dedicated to reveal their specific contributions to functional connectivity development during early years of life using genetically related twin subjects.

Appendix A

Simulated Annealing for Optimal DTI Parameters

The simulated annealing (SA) method is suitable for optimization problems of large scales, especially when the desired global minimum is hidden among many local extremes. The specific elements of the SA algorithm are listed below:

a) Generator of random changes

Δ and R: Δ and R were taken as the square of two numbers A and B setting to random walk to avoid negative b-values at each step. Random numbers choosing from a standard Gaussian distribution scaled by 10^{-3} were added to every A and B, respectively, at each step.

Gradient directions: All 3D vectors of the diffusion gradient directions were first transferred to a spherical coordinate so that each diffusion gradient direction corresponds to two elements: azimuth angle theta and elevation angle phy. At each step, a random number choosing from a scaled standard Gaussian distribution was independently added to each of these two angles of every diffusion gradient direction. For better performance against local minima, the scale factor S (the magnitude of each random number) depended on the current temperature T, i.e., if T>=1000, S=0.001*T and if T<1000, S=0.001. After random walk of each step, these directional vectors in the spherical coordinate were transferred back to the Cartesian coordinate for cost function evaluation.

b) The acceptance-rejection algorithm

The Metropolis-Hastings algorithm (286, 287) was applied for decision making on acceptance or rejection. Specifically, the system altered its configuration from energy

E_1 to E_2 according to the probability $p = \exp(-(E_2 - E_1)/T)$. If $E_2 < E_1$, then the system always accepted E_2, otherwise the system accepted E_2 with a probability $p < 1$. The probability $p = \exp(-(E_2 - E_1)/T)$ became smaller as T increased.

c) Cost function

The cost functions were the sum of the trace of every covariance matrix resulted from each known θ, $\sum_{i=1}^{n} Tr(\sum \beta_{LS})_i$.

d) Default settings

Initial Δ and R : 0.01 ms

Initial gradient directions: 3D vectors with random entries choosing from a standard Gaussian distribution but normalized to be unit vectors;

Initial temperature: 2000 Kelvin ;

Stop temperature: 10^{-18} Kelvin;

Stop energy (value of cost function): infinitely small;

Cooling schedule: 0.98*T (current temperature);

Maximum number of consecutive rejections: 1000;

Maximum number of tries within one temperature: 1000;

Prior information θ was derived from the predefined tensor field;

e) Recording of parameters and cost function values: A term referred to as "E_best" was used to track the most minimal cost function value. After each run, the cost function value was compared to the current E_best and if this value was less than the current E_best, this value was recorded together with the random-walk parameters that result in this value. However, we only kept the latest 10000 sets of values and defined

the optimal ranges of each parameter based on this set. After optimization, a series of 11 different b-values corresponding to the 1st, 1000^{th}, till 10000^{th} at a 1000 interval of the recorded 10000 b-values (sorted) were chosen to evenly cover the whole sampled b-value range and used for optimal b-value range testing.

Appendix B

Derivation of Design Criteria for Weighted Least Square Estimation

Although we only presented results with the LS estimation method, our optimization scheme can be applied with different estimation methods if proper design criteria can be established accordingly. In this section, the derivation of the design criteria for WLS estimation is provided.

The WLS estimator of $\vec{\beta}$ is $\tilde{\beta}_{WLS} = (X^T \Sigma_\varepsilon^{-1} X) \cdot X^T \Sigma_\varepsilon \cdot \vec{Y}$ and its covariance matrix is given by

$$\Sigma_{\beta_{WLS}} = (X^T \Sigma_\varepsilon^{-1} X)^{-1} = (\sum_{i=1}^{n} X_i^T X_i \frac{\left\langle S(\tilde{b}) \right\rangle^2}{\sigma_\eta^2})^{-1} . \quad \text{(B1)}$$

Again by defining $Z_i^T = [-b_i r_{i1}^2, -2b_i r_{i1} r_{i2}, -2b_i r_{i1} r_{i3}, -b_i r_{i2}^2, -2b_i r_{i2} r_{i3}, -b_i r_{i3}^2]$

and $\theta = [(D_0)_{11}, (D_0)_{12}, (D_0)_{13}, (D_0)_{22}, (D_0)_{23}, (D_0)_{33}]$, Eq. (B1) can be written as

$$\Sigma_{\beta_{WLS}} = \frac{\sigma_\eta^2}{S_0^2} \cdot (\sum_{i=1}^{n} X_i^T X_i \exp(2Z_i^T \theta))^{-1} \quad \text{(B2)}$$

The incorporation of other imaging parameters follows the same deduction as that for LS estimation as described in the Method section, which resulted in the following expression:

$$\Sigma_{\beta WLS} = ((\frac{P_0^2 \exp(-2TE/T2)(R_H + R)}{\sigma_\eta^2}) \cdot \sum_{i=1}^{n} X_i^T X_i \exp(2Z_i^T \theta))^{-1} . \quad \text{(B3)}$$

References

1. **Israel Z & Bergman H (2008) Pathophysiology of the basal ganglia and movement disorders: from animal models to human clinical applications. *Neurosci Biobehav Rev* 32: 367-377.**

2. **Serra J, Bostock H, & Navarro X Microneurography in rats: a minimally invasive method to record single C-fiber action potentials from peripheral nerves in vivo. *Neurosci Lett* 470: 168-174.**

3. **Ward MP, Rajdev P, Ellison C, & Irazoqui PP (2009) Toward a comparison of microelectrodes for acute and chronic recordings. *Brain Res* 1282: 183-200.**

4. **Campbell IG (2009) EEG recording and analysis for sleep research. *Curr Protoc Neurosci* Chapter 10: Unit10 12.**

5. **Hrdlicka M (2008) EEG abnormalities, epilepsy and regression in autism: a review. *Neuro Endocrinol Lett* 29: 405-409.**

6. **Rodin E, Constantino T, Rampp S, & Wong PK (2009) Spikes and epilepsy. *Clin EEG Neurosci* 40: 288-299.**

7. **Rose S & Ebersole JS (2009) Advances in spike localization with EEG dipole modeling. *Clin EEG Neurosci* 40: 281-287.**

8. **Heran MK, Heran NS, & Shemie SD (2008) A review of ancillary tests in evaluating brain death. *Can J Neurol Sci* 35: 409-419.**

9. **Sediri H, Bourriez JL, & Derambure P (2007) [Role of EEG in the diagnosis of brain death]. *Rev Neurol (Paris)* 163: 248-253.**

10. **Guerit JM, *et al.* (2009) Consensus on the use of neurophysiological tests in the intensive care unit (ICU): electroencephalogram (EEG), evoked potentials (EP), and electroneuromyography (ENMG). *Neurophysiol Clin* 39: 71-83.**

11. **Young GB (2009) Continuous EEG monitoring in the ICU: challenges and opportunities. *Can J Neurol Sci* 36 Suppl 2: S89-91.**

12. **Bandettini PA, *et al.* (1992) Time course EPI of human brain function during task activation. *Magn Reson Med* 25: 390-397.**

13. **Menon RS, *et al.* (1992) Functional brain mapping using magnetic resonance imaging. Signal changes accompanying visual stimulation. *Invest Radiol* 27 Suppl 2: S47-53.**

14. **Ogawa S & Lee TM (1990) Magnetic resonance imaging of blood vessels at high fields: in vivo and in vitro measurements and image simulation. *Magn Reson Med* 16: 9-18.**

15. **Binder JR, *et al.* (1994) Functional magnetic resonance imaging of human auditory cortex. *Ann Neurol* 35: 662-672.**

16. **Demonet JF, Thierry G, & Cardebat D (2005) Renewal of the neurophysiology of language: functional neuroimaging. *Physiol Rev* 85: 49-95.**

17. **Gaillard WD (2004) Functional MR imaging of language, memory, and sensorimotor cortex. *Neuroimaging Clin N Am* 14: 471-485.**

18. **Kollias SS (2004) Investigations of the human visual system using functional magnetic resonance imaging (FMRI). *Eur J Radiol* 49: 64-75.**

19. **Woods DL & Alain C (2009) Functional imaging of human auditory cortex. *Curr Opin Otolaryngol Head Neck Surg* 17: 407-411.**

20. **Biswal B, Yetkin FZ, Haughton VM, & Hyde JS (1995) Functional connectivity in the motor cortex of resting human brain using echo-planar MRI. *Magn Reson Med* 34: 537-541.**

21. **Buckner RL & Vincent JL (2007) Unrest at rest: default activity and spontaneous network correlations. *Neuroimage* 37: 1091-1096; discussion 1097-1099.**

22. **Damoiseaux JS, *et al.* (2006) Consistent resting-state networks across healthy subjects. *Proc Natl Acad Sci U S A* 103: 13848-13853.**

23. **Fox MD, *et al.* (2005) The human brain is intrinsically organized into dynamic, anticorrelated functional networks. *Proc Natl Acad Sci U S A* 102: 9673-9678.**

24. **Greicius MD, Krasnow B, Reiss AL, & Menon V (2003) Functional connectivity in the resting brain: a network analysis of the default mode hypothesis. *Proc Natl Acad Sci U S A* 100: 253-258.**

25. **Raichle ME (2006) Neuroscience. The brain's dark energy. *Science* 314: 1249-1250.**

26. **Raichle ME, *et al.* (2001) A default mode of brain function. *Proc Natl Acad Sci U S A* 98: 676-682.**

27. **Gusnard DA & Raichle ME (2001) Searching for a baseline: functional imaging and the resting human brain. *Nat Rev Neurosci* 2: 685-694.**

28. **Buckner RL, Andrews-Hanna JR, & Schacter DL (2008) The brain's default network: anatomy, function, and relevance to disease.** ***Ann N Y Acad Sci*** **1124: 1-38.**

29. **Lin W,** ***et al.*** **(2008) Functional connectivity MR imaging reveals cortical functional connectivity in the developing brain.** ***AJNR Am J Neuroradiol*** **29: 1883-1889.**

30. **Fox MD,** ***et al.*** **(2006) Spontaneous neuronal activity distinguishes human dorsal and ventral attention systems.** ***Proc Natl Acad Sci U S A*** **103: 10046-10051.**

31. **Hampson M,** ***et al.*** **(2006) Brain connectivity related to working memory performance.** ***J Neurosci*** **26: 13338-13343.**

32. **Vincent JL,** ***et al.*** **(2006) Coherent spontaneous activity identifies a hippocampal-parietal memory network.** ***J Neurophysiol*** **96: 3517-3531.**

33. **Tau GZ & Peterson BS Normal development of brain circuits.** ***Neuropsychopharmacology*** **35: 147-168.**

34. **D'Agati E, Moavero R, Cerminara C, & Curatolo P (2009) Attention-deficit hyperactivity disorder (ADHD) and tuberous sclerosis complex.** ***J Child Neurol*** **24: 1282-1287.**

35. **Mala E (2008) Schizophrenia in childhood and adolescence.** ***Neuro Endocrinol Lett*** **29: 831-836.**

36. **Basser PJ, Mattiello J, & LeBihan D (1994) Estimation of the effective self-diffusion tensor from the NMR spin echo.** ***J Magn Reson B*** **103: 247-254.**

37. **Basser PJ & Pierpaoli C (1996) Microstructural and physiological features of tissues elucidated by quantitative-diffusion-tensor MRI.** ***J Magn Reson B*** **111: 209-219.**

38. **Haacke EM, Brown RW, Thompson MR, & Venkatesan R (1999)** ***Magnetic Resonance Imaing-Physical Principles and Sequence Design*** **(Wiley-Liss, New York, Chichester, Weinheim, Brisbane, Singapore, Toronto).**

39. **Tuch DS,** ***et al.*** **(2002) High angular resolution diffusion imaging reveals intravoxel white matter fiber heterogeneity.** ***Magn Reson Med*** **48: 577-582.**

40. **Gao W,** ***et al.*** **(2008) Temporal and Spatial Development of Axonal Maturation and Myelination of White Matter in the Developing Brain.** ***AJNR Am J Neuroradiol.***

41. Partridge SC*, et al.* (2004) Diffusion tensor imaging: serial quantitation of white matter tract maturity in premature newborns. *Neuroimage* 22: 1302-1314.

42. Hagmann P*, et al.* (2008) Mapping the structural core of human cerebral cortex. *PLoS Biol* 6: e159.

43. Chua TC, Wen W, Slavin MJ, & Sachdev PS (2008) Diffusion tensor imaging in mild cognitive impairment and Alzheimer's disease: a review. *Curr Opin Neurol* 21: 83-92.

44. Kyriakopoulos M & Frangou S (2009) Recent diffusion tensor imaging findings in early stages of schizophrenia. *Curr Opin Psychiatry* 22: 168-176.

45. Wiegell MR, Larsson HB, & Wedeen VJ (2000) Fiber crossing in human brain depicted with diffusion tensor MR imaging. *Radiology* 217: 897-903.

46. Tuch DS (2004) Q-ball imaging. *Magn Reson Med* 52: 1358-1372.

47. Wandell BA, Dumoulin SO, & Brewer AA (2007) Visual field maps in human cortex. *Neuron* 56: 366-383.

48. De Luca M*, et al.* (2006) fMRI resting state networks define distinct modes of long-distance interactions in the human brain. *Neuroimage* 29: 1359-1367.

49. Logothetis NK*, et al.* (2001) Neurophysiological investigation of the basis of the fMRI signal. *Nature* 412: 150-157.

50. Logothetis NK & Pfeuffer J (2004) On the nature of the BOLD fMRI contrast mechanism. *Magn Reson Imaging* 22: 1517-1531.

51. Logothetis NK & Wandell BA (2004) Interpreting the BOLD signal. *Annu Rev Physiol* 66: 735-769.

52. Fox PT, Raichle ME, Mintun MA, & Dence C (1988) Nonoxidative glucose consumption during focal physiologic neural activity. *Science* 241: 462-464.

53. Caesar K, Akgoren N, Mathiesen C, & Lauritzen M (1999) Modification of activity-dependent increases in cerebellar blood flow by extracellular potassium in anaesthetized rats. *J Physiol* 520 Pt 1: 281-292.

54. Iadecola C (1993) Regulation of the cerebral microcirculation during neural activity: is nitric oxide the missing link? *Trends Neurosci* 16: 206-214.

55. **Li J & Iadecola C (1994) Nitric oxide and adenosine mediate vasodilation during functional activation in cerebellar cortex. *Neuropharmacology* 33: 1453-1461.**

56. **Almeida A, Bolanos JP, & Medina JM (1999) Nitric oxide mediates glutamate-induced mitochondrial depolarization in rat cortical neurons. *Brain Res* 816: 580-586.**

57. **Bredt DS & Snyder SH (1989) Nitric oxide mediates glutamate-linked enhancement of cGMP levels in the cerebellum. *Proc Natl Acad Sci U S A* 86: 9030-9033.**

58. **Dominguez JM, Muschamp JW, Schmich JM, & Hull EM (2004) Nitric oxide mediates glutamate-evoked dopamine release in the medial preoptic area. *Neuroscience* 125: 203-210.**

59. **Alkayed NJ, *et al.* (1997) Role of P-450 arachidonic acid epoxygenase in the response of cerebral blood flow to glutamate in rats. *Stroke* 28: 1066-1072.**

60. **Cholet N, *et al.* (2001) Local injection of antisense oligonucleotides targeted to the glial glutamate transporter GLAST decreases the metabolic response to somatosensory activation. *J Cereb Blood Flow Metab* 21: 404-412.**

61. **Lipton P & Robacker K (1983) Glycolysis and brain function: [K+]o stimulation of protein synthesis and K+ uptake require glycolysis. *Fed Proc* 42: 2875-2880.**

62. **Parker JC & Hoffman JF (1967) The role of membrane phosphoglycerate kinase in the control of glycolytic rate by active cation transport in human red blood cells. *J Gen Physiol* 50: 893-916.**

63. **Prichard J, *et al.* (1991) Lactate rise detected by 1H NMR in human visual cortex during physiologic stimulation. *Proc Natl Acad Sci U S A* 88: 5829-5831.**

64. **Logothetis NK (2003) The underpinnings of the BOLD functional magnetic resonance imaging signal. *J Neurosci* 23: 3963-3971.**

65. **Goense JB & Logothetis NK (2008) Neurophysiology of the BOLD fMRI signal in awake monkeys. *Curr Biol* 18: 631-640.**

66. **Mukamel R, *et al.* (2005) Coupling between neuronal firing, field potentials, and FMRI in human auditory cortex. *Science* 309: 951-954.**

67. **Nir Y, *et al.* (2007) Coupling between neuronal firing rate, gamma LFP, and BOLD fMRI is related to interneuronal correlations. *Curr Biol* 17: 1275-1285.**

68. Bressler SL (2003) Cortical coordination dynamics and the disorganization syndrome in schizophrenia. *Neuropsychopharmacology* 28 Suppl 1: S35-39.

69. Bressler SL & Kelso JA (2001) Cortical coordination dynamics and cognition. *Trends Cogn Sci* 5: 26-36.

70. Bressler SL & Tognoli E (2006) Operational principles of neurocognitive networks. *Int J Psychophysiol* 60: 139-148.

71. Engel AK, *et al.* (1999) Temporal binding, binocular rivalry, and consciousness. *Conscious Cogn* 8: 128-151.

72. Friston KJ, Frith CD, Liddle PF, & Frackowiak RS (1993) Functional connectivity: the principal-component analysis of large (PET) data sets. *J Cereb Blood Flow Metab* 13: 5-14.

73. Singer W (1993) Synchronization of cortical activity and its putative role in information processing and learning. *Annu Rev Physiol* 55: 349-374.

74. Varela F, Lachaux JP, Rodriguez E, & Martinerie J (2001) The brainweb: phase synchronization and large-scale integration. *Nat Rev Neurosci* 2: 229-239.

75. von der Malsburg C (1999) The what and why of binding: the modeler's perspective. *Neuron* 24: 95-104, 111-125.

76. Bressler SL (1995) Large-scale cortical networks and cognition. *Brain Res Brain Res Rev* 20: 288-304.

77. Koenig T, *et al.* (2002) Millisecond by millisecond, year by year: normative EEG microstates and developmental stages. *Neuroimage* 16: 41-48.

78. Goldman-Rakic PS (1988) Topography of cognition: parallel distributed networks in primate association cortex. *Annu Rev Neurosci* 11: 137-156.

79. Bressler SL, Coppola R, & Nakamura R (1993) Episodic multiregional cortical coherence at multiple frequencies during visual task performance. *Nature* 366: 153-156.

80. Liang H, Ding M, Nakamura R, & Bressler SL (2000) Causal influences in primate cerebral cortex during visual pattern discrimination. *Neuroreport* 11: 2875-2880.

81. Engel AK, Kreiter AK, Konig P, & Singer W (1991) Synchronization of oscillatory neuronal responses between striate and extrastriate visual cortical areas of the cat. *Proc Natl Acad Sci U S A* 88: 6048-6052.

82. **Gray CM, Konig P, Engel AK, & Singer W (1989) Oscillatory responses in cat visual cortex exhibit inter-columnar synchronization which reflects global stimulus properties.** ***Nature*** **338: 334-337.**

83. **Freeman WJ & Baird B (1987) Relation of olfactory EEG to behavior: spatial analysis.** ***Behav Neurosci*** **101: 393-408.**

84. **Murthy VN & Fetz EE (1992) Coherent 25- to 35-Hz oscillations in the sensorimotor cortex of awake behaving monkeys.** ***Proc Natl Acad Sci U S A*** **89: 5670-5674.**

85. **Sanes JN & Donoghue JP (1993) Oscillations in local field potentials of the primate motor cortex during voluntary movement.** ***Proc Natl Acad Sci U S A*** **90: 4470-4474.**

86. **Young MP, Tanaka K, & Yamane S (1992) On oscillating neuronal responses in the visual cortex of the monkey.** ***J Neurophysiol*** **67: 1464-1474.**

87. **Kus R, Kaminski M, & Blinowska KJ (2004) Determination of EEG activity propagation: pair-wise versus multichannel estimate.** ***IEEE Trans Biomed Eng*** **51: 1501-1510.**

88. **Vincent JL,** ***et al.*** **(2008) Evidence for a frontoparietal control system revealed by intrinsic functional connectivity.** ***J Neurophysiol*** **100: 3328-3342.**

89. **Nir Y,** ***et al.*** **(2008) Interhemispheric correlations of slow spontaneous neuronal fluctuations revealed in human sensory cortex.** ***Nat Neurosci*** **11: 1100-1108.**

90. **Lewis JW & Van Essen DC (2000) Mapping of architectonic subdivisions in the macaque monkey, with emphasis on parieto-occipital cortex.** ***J Comp Neurol*** **428: 79-111.**

91. **Vincent JL,** ***et al.*** **(2007) Intrinsic functional architecture in the anaesthetized monkey brain.** ***Nature*** **447: 83-86.**

92. **Van Dijk KR,** ***et al.*** **Intrinsic functional connectivity as a tool for human connectomics: theory, properties, and optimization.** ***J Neurophysiol*** **103: 297-321.**

93. **Margulies DS,** ***et al.*** **(2009) Precuneus shares intrinsic functional architecture in humans and monkeys.** ***Proc Natl Acad Sci U S A*** **106: 20069-20074.**

94. **Honey CJ,** ***et al.*** **(2009) Predicting human resting-state functional connectivity from structural connectivity.** ***Proc Natl Acad Sci U S A*** **106: 2035-2040.**

95. **Greicius MD, Supekar K, Menon V, & Dougherty RF (2009) Resting-state functional connectivity reflects structural connectivity in the default mode network. *Cereb Cortex* 19: 72-78.**

96. **Hasson U, Nusbaum HC, & Small SL (2009) Task-dependent organization of brain regions active during rest. *Proc Natl Acad Sci U S A* 106: 10841-10846.**

97. **Kelly AM, *et al.* (2008) Competition between functional brain networks mediates behavioral variability. *Neuroimage* 39: 527-537.**

98. **Stevens WD, Buckner RL, & Schacter DL (2009) Correlated Low-Frequency BOLD Fluctuations in the Resting Human Brain Are Modulated by Recent Experience in Category-Preferential Visual Regions. *Cereb Cortex*.**

99. **Tambini A, Ketz N, & Davachi L Enhanced Brain Correlations during Rest Are Related to Memory for Recent Experiences. *Neuron* 65: 280-290.**

100. **Achard S & Bullmore E (2007) Efficiency and cost of economical brain functional networks. *PLoS Comput Biol* 3: e17.**

101. **Fair DA, *et al.* (2008) The maturing architecture of the brain's default network. *Proc Natl Acad Sci U S A* 105: 4028-4032.**

102. **Gao W, *et al.* (2009) Evidence on the emergence of the brain's default network from 2-week-old to 2-year-old healthy pediatric subjects. *Proc Natl Acad Sci U S A* 106: 6790-6795.**

103. **Biswal BB & Ulmer JL (1999) Blind source separation of multiple signal sources of fMRI data sets using independent component analysis. *J Comput Assist Tomogr* 23: 265-271.**

104. **Fox MD, Zhang D, Snyder AZ, & Raichle ME (2009) The global signal and observed anticorrelated resting state brain networks. *J Neurophysiol* 101: 3270-3283.**

105. **Murphy K, *et al.* (2009) The impact of global signal regression on resting state correlations: are anti-correlated networks introduced? *Neuroimage* 44: 893-905.**

106. **Knickmeyer RC, *et al.* (2008) A structural MRI study of human brain development from birth to 2 years. *J Neurosci* 28: 12176-12182.**

107. **Gottlieb G ed. (1992) *Individual development and evolution* (Oxford University Press, New York).**

108. **Johnson MH (2000) Functional brain development in infants: elements of an interactive specialization framework. *Child Dev* 71: 75-81.**

109. Belfort MB*, et al.* (2008) Infant growth and child cognition at 3 years of age. *Pediatrics* 122: e689-695.

110. Volpe J (2001) *Neurology of the newborn* (WB Saunders, Philadelphia).

111. Haynes RL*, et al.* (2005) Axonal development in the cerebral white matter of the human fetus and infant. *J Comp Neurol* 484: 156-167.

112. Song SK*, et al.* (2003) Diffusion tensor imaging detects and differentiates axon and myelin degeneration in mouse optic nerve after retinal ischemia. *Neuroimage* 20: 1714-1722.

113. Huang H*, et al.* (2006) White and gray matter development in human fetal, newborn and pediatric brains. *Neuroimage* 33: 27-38.

114. Gilmore JH*, et al.* (2007) Early Postnatal Development of Corpus Callosum and Corticospinal White Matter Assessed with Quantitative Tractography. *AJNR Am J Neuroradiol*.

115. Davidson AJ (2007) Awareness, dreaming and unconscious memory formation during anaesthesia in children. *Best Pract Res Clin Anaesthesiol* 21: 415-429.

116. DeCasper AJ & Fifer WP (1980) Of human bonding: newborns prefer their mothers' voices. *Science* 208: 1174-1176.

117. Kolata G (1984) Studying learning in the womb. *Science* 225: 302-303.

118. Fivush R, Hamond, N.R (1990) in *Knowing and remembering in young children*, ed. J.A.Hudson RFa (Cambridge Univ. Press, New York:).

119. Perner J & Ruffman T (1995) Episodic memory and autonoetic consciousness: developmental evidence and a theory of childhood amnesia. *J Exp Child Psychol* 59: 516-548.

120. Amsterdam (1972) Mirror self-image reactions before age two. Developmental Psychology. *Psychology* 5: 297-305.

121. Baldwin DA (1993) Early referential understanding: young children' s ability to recognize referential acts for what they are. *Developmental Psychology* 29: 832-843.

122. Tomasello M, Strosberg R, & Akhtar N (1996) Eighteen-month-old children learn words in non-ostensive contexts. *J Child Lang* 23: 157-176.

123. Tomasello M, & Barton, M. (1994) Learning words in nonostensive contexts. . *Developmental Psychology* 30: 639-650.

124. Akhtar N, & Tomasello, M. (2000) *The social nature of words and word learning* (Oxford University Press., Oxford).

125. Diesendruck G, Markson L, Akhtar N, & Reudor A (2004) Two-year-olds' sensitivity to speakers' intent: an alternative account of Samuelson and Smith. *Dev Sci* 7: 33-41.

126. JAY L. GARFIELD CCP, TRICIA PERRY (2001) Social Cognition, Language Acquisition and The Development of the Theory of Mind. *Mind & Language* 16: 494-541.

127. Dubois J, *et al.* (2008) Microstructural correlates of infant functional development: example of the visual pathways. *J Neurosci* 28: 1943-1948.

128. McGraw P, Liang L, & Provenzale JM (2002) Evaluation of normal age-related changes in anisotropy during infancy and childhood as shown by diffusion tensor imaging. *AJR Am J Roentgenol* 179: 1515-1522.

129. Mukherjee P, *et al.* (2002) Diffusion-tensor MR imaging of gray and white matter development during normal human brain maturation. *AJNR Am J Neuroradiol* 23: 1445-1456.

130. Schneider JF, Il'yasov KA, Hennig J, & Martin E (2004) Fast quantitative diffusion-tensor imaging of cerebral white matter from the neonatal period to adolescence. *Neuroradiology* 46: 258-266.

131. Huppi PS, *et al.* (1998) Microstructural development of human newborn cerebral white matter assessed in vivo by diffusion tensor magnetic resonance imaging. *Pediatr Res* 44: 584-590.

132. Counsell SJ, *et al.* (2006) Axial and radial diffusivity in preterm infants who have diffuse white matter changes on magnetic resonance imaging at term-equivalent age. *Pediatrics* 117: 376-386.

133. Schmithorst VJ, Wilke M, Dardzinski BJ, & Holland SK (2002) Correlation of white matter diffusivity and anisotropy with age during childhood and adolescence: a cross-sectional diffusion-tensor MR imaging study. *Radiology* 222: 212-218.

134. Snook L, *et al.* (2005) Diffusion tensor imaging of neurodevelopment in children and young adults. *Neuroimage* 26: 1164-1173.

135. Mukherjee P, *et al.* (2001) Normal brain maturation during childhood: developmental trends characterized with diffusion-tensor MR imaging. *Radiology* 221: 349-358.

136. Miller JH, *et al.* (2003) Diffusion-tensor MR imaging of normal brain maturation: a guide to structural development and myelination. *AJR Am J Roentgenol* 180: 851-859.

137. Hermoye L, *et al.* (2006) Pediatric diffusion tensor imaging: normal database and observation of the white matter maturation in early childhood. *Neuroimage* 29: 493-504.

138. Zhai G, *et al.* (2003) Comparisons of regional white matter diffusion in healthy neonates and adults performed with a 3.0-T head-only MR imaging unit. *Radiology* 229: 673-681.

139. Basser PJ (1995) Inferring microstructural features and the physiological state of tissues from diffusion-weighted images. *NMR Biomed* 8: 333-344.

140. Basser PJ, *et al.* (2000) In vivo fiber tractography using DT-MRI data. *Magn Reson Med* 44: 625-632.

141. Xue R, *et al.* (1999) In vivo three-dimensional reconstruction of rat brain axonal projections by diffusion tensor imaging. *Magn Reson Med* 42: 1123-1127.

142. Song SK, *et al.* (2005) Demyelination increases radial diffusivity in corpus callosum of mouse brain. *Neuroimage* 26: 132-140.

143. Budde MD, *et al.* (2007) Toward accurate diagnosis of white matter pathology using diffusion tensor imaging. *Magn Reson Med* 57: 688-695.

144. Pierpaoli C & Basser PJ (1996) Toward a quantitative assessment of diffusion anisotropy. *Magn Reson Med* 36: 893-906.

145. Volpe J (1995) *Neurology of newborn* (Saunders, Philadelphia).

146. Ashtari M, *et al.* (2007) White matter development during late adolescence in healthy males: a cross-sectional diffusion tensor imaging study. *Neuroimage* 35: 501-510.

147. Kantor DB & Kolodkin AL (2003) Curbing the excesses of youth: molecular insights into axonal pruning. *Neuron* 38: 849-852.

148. Richards LJ, Plachez C, & Ren T (2004) Mechanisms regulating the development of the corpus callosum and its agenesis in mouse and human. *Clin Genet* 66: 276-289.

149. Bockhorst KH, *et al.* (2008) Early postnatal development of rat brain: in vivo diffusion tensor imaging. *J Neurosci Res* 86: 1520-1528.

150. Cuenca N, *et al.* (1987) Postnatal development of microtubules and neurofilaments in the rat optic nerve: a quantitative study. *J Comp Neurol* 263: 613-617.

151. Hebb DO (1949) *The Organization of Behavior: A Neurophysiological Theory* (Wiley, New York).

152. Tononi G, McIntosh AR, Russell DP, & Edelman GM (1998) Functional clustering: identifying strongly interactive brain regions in neuroimaging data. *Neuroimage* 7: 133-149.

153. Gao W, *et al.* (in press) Emergence of the brain's default network: Evidence from two-week-old to 2-year-old healthy pediatric subjects. *Proc Natl Acad Sci U S A*.

154. Shulman GL FJ, Corbetta M, Buckner RL, Miezin FM (1997) Common blood flow changes across visual tasks: II.: decreases in cerebral cortex. *J. Cogn. Neurosci* 9: 648-663.

155. Gusnard DA, Akbudak E, Shulman GL, & Raichle ME (2001) Medial prefrontal cortex and self-referential mental activity: relation to a default mode of brain function. *Proc Natl Acad Sci U S A* 98: 4259-4264.

156. Mazoyer B, *et al.* (2001) Cortical networks for working memory and executive functions sustain the conscious resting state in man. *Brain Res Bull* 54: 287-298.

157. Fransson P (2005) Spontaneous low-frequency BOLD signal fluctuations: an fMRI investigation of the resting-state default mode of brain function hypothesis. *Hum Brain Mapp* 26: 15-29.

158. Shannon BJ (2006) *Functional anatomic studies of memory retrieval and the default mode* (Washington University in St. Louis, St. Louis).

159. Rombouts SA, *et al.* (2005) Altered resting state networks in mild cognitive impairment and mild Alzheimer's disease: an fMRI study. *Hum Brain Mapp* 26: 231-239.

160. Morcom AM & Fletcher PC (2007) Does the brain have a baseline? Why we should be resisting a rest. *Neuroimage* 37: 1073-1082.

161. Uddin LQ, *et al.* (2008) Functional connectivity of default mode network components: Correlation, anticorrelation, and causality. *Hum Brain Mapp*.

162. Fransson P, *et al.* (2007) Resting-state networks in the infant brain. *Proc Natl Acad Sci U S A* 104: 15531-15536.

163. Gilmore JH, *et al.* (2007) Regional gray matter growth, sexual dimorphism, and cerebral asymmetry in the neonatal brain. *J Neurosci* 27: 1255-1260.

164. Shen D & Davatzikos C (2002) HAMMER: hierarchical attribute matching mechanism for elastic registration. *IEEE Trans Med Imaging* 21: 1421-1439.

165. Bell AJ, Sejnowski, T.J., (1995) An information maximisation approach to blind separation and blind deconvolution. . *Neural Comput* 7: 1129–1159.

166. Li YO, Adali T, & Calhoun VD (2007) Estimating the number of independent components for functional magnetic resonance imaging data. *Hum Brain Mapp* 28: 1251-1266.

167. Calhoun VD, Adali T, Pearlson GD, & Pekar JJ (2001) A method for making group inferences from functional MRI data using independent component analysis. *Hum Brain Mapp* 14: 140-151.

168. Tzourio-Mazoyer N, *et al.* (2002) Automated anatomical labeling of activations in SPM using a macroscopic anatomical parcellation of the MNI MRI single-subject brain. *Neuroimage* 15: 273-289.

169. Greicius MD, Srivastava G, Reiss AL, & Menon V (2004) Default-mode network activity distinguishes Alzheimer's disease from healthy aging: evidence from functional MRI. *Proc Natl Acad Sci U S A* 101: 4637-4642.

170. Benjamini Y YY (2001) The contorl of the false discovery rate in multilpe testing under dependency. *Ann Statist* 29: 1165-1188.

171. Ebbels TM, Buxton BF, & Jones DT (2006) springScape: visualisation of microarray and contextual bioinformatic data using spring embedding and an 'information landscape'. *Bioinformatics* 22: e99-107.

172. Hampson M, *et al.* (2006) Connectivity-behavior analysis reveals that functional connectivity between left BA39 and Broca's area varies with reading ability. *Neuroimage* 31: 513-519.

173. Brandes U (2001) A faster algorithm for betweenness centrality. *J Math Sociol* 25: 163-177.

174. Mitchell JP, Macrae CN, & Banaji MR (2006) Dissociable medial prefrontal contributions to judgments of similar and dissimilar others. *Neuron* 50: 655-663.

175. Buckner RL & Carroll DC (2007) Self-projection and the brain. *Trends Cogn Sci* 11: 49-57.

176. Flavell JH (1999) Cognitive development: Children's knowledge about the mind. *Annu Rev Psychol* 50: 21-45.

177. Lou HC, *et al.* (2004) Parietal cortex and representation of the mental Self. *Proc Natl Acad Sci U S A* 101: 6827-6832.

178. Corbetta M & Shulman GL (2002) Control of goal-directed and stimulus-driven attention in the brain. *Nat Rev Neurosci* 3: 201-215.

179. Cabeza R, Ciaramelli E, Olson IR, & Moscovitch M (2008) The parietal cortex and episodic memory: an attentional account. *Nat Rev Neurosci* 9: 613-625.

180. Henson RN, *et al.* (1999) Recollection and familiarity in recognition memory: an event-related functional magnetic resonance imaging study. *J Neurosci* 19: 3962-3972.

181. Uncapher MR & Wagner AD (2009) Posterior parietal cortex and episodic encoding: insights from fMRI subsequent memory effects and dual-attention theory. *Neurobiol Learn Mem* 91: 139-154.

182. Wheeler ME & Buckner RL (2004) Functional-anatomic correlates of remembering and knowing. *Neuroimage* 21: 1337-1349.

183. Sridharan D, Levitin DJ, & Menon V (2008) A critical role for the right fronto-insular cortex in switching between central-executive and default-mode networks. *Proc Natl Acad Sci U S A* 105: 12569-12574.

184. Koechlin E, *et al.* (1999) The role of the anterior prefrontal cortex in human cognition. *Nature* 399: 148-151.

185. Kompus K, *et al.* (2009) Distinct control networks for cognition and emotion in the prefrontal cortex. *Neurosci Lett* 467: 76-80.

186. Furman O, *et al.* (2007) They saw a movie: long-term memory for an extended audiovisual narrative. *Learn Mem* 14: 457-467.

187. Iacoboni M, *et al.* (2004) Watching social interactions produces dorsomedial prefrontal and medial parietal BOLD fMRI signal increases compared to a resting baseline. *Neuroimage* 21: 1167-1173.

188. Koechlin E & Hyafil A (2007) Anterior prefrontal function and the limits of human decision-making. *Science* 318: 594-598.

189. Ramnani N & Owen AM (2004) Anterior prefrontal cortex: insights into function from anatomy and neuroimaging. *Nat Rev Neurosci* 5: 184-194.

190. Cole MW & Schneider W (2007) The cognitive control network: Integrated cortical regions with dissociable functions. *Neuroimage* 37: 343-360.

191. Posner MI & Rothbart MK (2007) Research on attention networks as a model for the integration of psychological science. *Annu Rev Psychol* 58: 1-23.

192. Roberts KL & Hall DA (2008) Examining a supramodal network for conflict processing: a systematic review and novel functional magnetic resonance imaging data for related visual and auditory stroop tasks. *J Cogn Neurosci* 20: 1063-1078.

193. Crone EA, Wendelken C, Donohue SE, & Bunge SA (2006) Neural evidence for dissociable components of task-switching. *Cereb Cortex* 16: 475-486.

194. Sapir A, *et al.* (2005) Brain signals for spatial attention predict performance in a motion discrimination task. *Proc Natl Acad Sci U S A* 102: 17810-17815.

195. Buschman TJ & Miller EK (2007) Top-down versus bottom-up control of attention in the prefrontal and posterior parietal cortices. *Science* 315: 1860-1862.

196. Blood AJ, Zatorre RJ, Bermudez P, & Evans AC (1999) Emotional responses to pleasant and unpleasant music correlate with activity in paralimbic brain regions. *Nat Neurosci* 2: 382-387.

197. Pallesen KJ, *et al.* (2009) Cognitive and emotional modulation of brain default operation. *J Cogn Neurosci* 21: 1065-1080.

198. Keightley ML, *et al.* (2003) An fMRI study investigating cognitive modulation of brain regions associated with emotional processing of visual stimuli. *Neuropsychologia* 41: 585-596.

199. Hariri AR, Bookheimer SY, & Mazziotta JC (2000) Modulating emotional responses: effects of a neocortical network on the limbic system. *Neuroreport* 11: 43-48.

200. Jafri MJ, Pearlson GD, Stevens M, & Calhoun VD (2008) A method for functional network connectivity among spatially independent resting-state components in schizophrenia. *Neuroimage* 39: 1666-1681.

201. Hotelling H (1936) Relations between two sets of variants. *Biometrika*: 312-377.

202. Fisher RA (1950) *Statistical Methods for Research Workers* (Oliver and Boyd, London).

203. Lazar NA, Luna B, Sweeney JA, & Eddy WF (2002) Combining brains: a survey of methods for statistical pooling of information. *Neuroimage* 16: 538-550.

204. Tukey JW (1949) Comparing individual means in the analysis of variance. *Biometrics* 5: 99-114.

205. Salvador R, *et al.* (2005) Neurophysiological architecture of functional magnetic resonance images of human brain. *Cerebral Cortex* 34: 387-413.

206. Watts DJ & Strogatz SH (1998) Collective dynamics of 'small-world' networks. *Nature* 393: 440-442.

207. He Y, *et al.* (2009) Uncovering intrinsic modular organization of spontaneous brain activity in humans. *PLoS One* 4: e5226.

208. Meunier D, Achard S, Morcom A, & Bullmore E (2009) Age-related changes in modular organization of human brain functional networks. *Neuroimage* 44: 715-723.

209. Liu Y, *et al.* (2008) Disrupted small-world networks in schizophrenia. *Brain* 131: 945-961.

210. Supekar K, *et al.* (2008) Network analysis of intrinsic functional brain connectivity in Alzheimer's disease. *PLoS Comput Biol* 4: e1000100.

211. Fair DA, *et al.* (2009) Functional brain networks develop from a "local to distributed" organization. *PLoS Comput Biol* 5: e1000381.

212. Supekar K, Musen M, & Menon V (2009) Development of large-scale functional brain networks in children. *PLoS Biol* 7: e1000157.

213. Andersen SL (2003) Trajectories of brain development: point of vulnerability or window of opportunity? *Neurosci Biobehav Rev* 27: 3-18.

214. Barkovich AJ, Kjos BO, Jackson DE, Jr., & Norman D (1988) Normal maturation of the neonatal and infant brain: MR imaging at 1.5 T. *Radiology* 166: 173-180.

215. Barnea-Goraly N, *et al.* (2005) White matter development during childhood and adolescence: a cross-sectional diffusion tensor imaging study. *Cereb Cortex* 15: 1848-1854.

216. Bourgeois JP & Rakic P (1993) Changes of synaptic density in the primary visual cortex of the macaque monkey from fetal to adult stage. *J Neurosci* 13: 2801-2820.

217. Lund JS & Lewis DA (1993) Local circuit neurons of developing and mature macaque prefrontal cortex: Golgi and immunocytochemical characteristics. *J Comp Neurol* 328: 282-312.

218. Newman ME (2006) Modularity and community structure in networks. *Proc Natl Acad Sci U S A* 103: 8577-8582.

219. Gomez S, Jensen P, & Arenas A (2009) Analysis of community structure in networks of correlated data. *Phys Rev E Stat Nonlin Soft Matter Phys* 80: 016114.

220. Latora V & Marchiori M (2001) Efficient behavior of small-world networks. *Phys Rev Lett* 87: 198701.

221. Parker GJ, *et al.* (2005) Lateralization of ventral and dorsal auditory-language pathways in the human brain. *Neuroimage* 24: 656-666.

222. Saur D, *et al.* (2008) Ventral and dorsal pathways for language. *Proc Natl Acad Sci U S A* 105: 18035-18040.

223. Happaney K, Zelazo PD, & Stuss DT (2004) Development of orbitofrontal function: current themes and future directions. *Brain Cogn* 55: 1-10.

224. Haber SN & Calzavara R (2009) The cortico-basal ganglia integrative network: the role of the thalamus. *Brain Res Bull* 78: 69-74.

225. Freeman L (1977) A set of measures of centrality based on betweenness. *Sociometry* 40: 35-41.

226. Tsujimoto S (2008) The prefrontal cortex: functional neural development during early childhood. *Neuroscientist* 14: 345-358.

227. Achard S, *et al.* (2006) A resilient, low-frequency, small-world human brain functional network with highly connected association cortical hubs. *J Neurosci* 26: 63-72.

228. Salvador R, Suckling, J., Coleman, M., Pickard, J. D., Menon, D., Bullmore, & E. (2005) Neurophysiological architecture of functional magnetic resonance images of human brain. *Cerebral Cortex* 34: 387-413.

229. M.Standley J (1998) Pre and Perinatal Growth and Development:Implications of Music Benefits for Premature Infants. *International Journal of Music Education* 31: 1-13.

230. Johnson MH (2001) Functional brain development in humans. *Nat Rev Neurosci* 2: 475-483.

231. Levitt P (2003) Structural and functional maturation of the developing primate brain. *J Pediatr* 143: S35-45.

232. Paus T, *et al.* (2001) Maturation of white matter in the human brain: a review of magnetic resonance studies. *Brain Res Bull* 54: 255-266.

233. Benes FM, Turtle M, Khan Y, & Farol P (1994) Myelination of a key relay zone in the hippocampal formation occurs in the human brain during childhood, adolescence, and adulthood. *Arch Gen Psychiatry* 51: 477-484.

234. Huttenlocher PR (1979) Synaptic density in human frontal cortex - developmental changes and effects of aging. *Brain Res* 163: 195-205.

235. Huttenlocher PR & Dabholkar AS (1997) Regional differences in synaptogenesis in human cerebral cortex. *J Comp Neurol* 387: 167-178.

236. Huttenlocher PR, de Courten C, Garey LJ, & Van der Loos H (1982) Synaptogenesis in human visual cortex--evidence for synapse elimination during normal development. *Neurosci Lett* 33: 247-252.

237. Sowell ER, *et al.* (2003) Mapping cortical change across the human life span. *Nat Neurosci* 6: 309-315.

238. Thompson PM, *et al.* (2004) Mapping cortical change in Alzheimer's disease, brain development, and schizophrenia. *Neuroimage* 23 Suppl 1: S2-18.

239. Luria AR (1973) *The working brain: An introduction to neuropsychology* (Basic Books, New York).

240. Golden CJ (1981) *The Luria-Nebraska children's battern: Theory and formulation* (Grune&Stratton, New York).

241. Piage J (1954) *The construction of reality in the child* (Basic Books, New York).

242. Grossmann T & Johnson MH Selective prefrontal cortex responses to joint attention in early infancy. *Biol Lett.*

243. Goursaud AP & Bachevalier J (2007) Social attachment in juvenile monkeys with neonatal lesion of the hippocampus, amygdala and orbital frontal cortex. *Behav Brain Res* 176: 75-93.

244. Bowlby J (1969) *Attachment* (Basic Books, New York).

245. Eslinger PJ, Flaherty-Craig CV, & Benton AL (2004) Developmental outcomes after early prefrontal cortex damage. *Brain Cogn* 55: 84-103.

246. Afif A*, et al.* (2007) Development of the human fetal insular cortex: study of the gyration from 13 to 28 gestational weeks. *Brain Struct Funct* 212: 335-346.

247. Streeter GL (1912) *The development of the nervous system* (Lippincott, Philadelphia).

248. Goodkin F (1980) The development of mature patterns of head-eye coordination in the human infant. *Early Hum Dev* 4: 373-386.

249. Rothbart MK (1990) *Regulatory mechanisms in infant development* (Elsevier/North-Holland, Amstardam).

250. Landing BH*, et al.* (2002) The development of structure and function in the postnatal human cerebral cortex from birth to 72 months: changes in thickness of layers II and III co-relate to the onset of new age-specific behaviors. *Pediatr Pathol Mol Med* 21: 321-342.

251. Meyer A (1961) A note on the postnatal development of the human cerebral cortex. *Cereb Palsy Bull* 3: 263-268.

252. Conel JL (1939-1963) *The Postnatal Development of Human Cerebral Cortex* (Harvard University Press, Cambridge).

253. Xing D*, et al.* (1997) Optimised diffusion-weighting for measurement of apparent diffusion coefficient (ADC) in human brain. *Magn Reson Imaging* 15: 771-784.

254. Jones DK, Horsfield MA, & Simmons A (1999) Optimal strategies for measuring diffusion in anisotropic systems by magnetic resonance imaging. *Magn Reson Med* 42: 515-525.

255. Armitage PA & Bastin ME (2001) Utilizing the diffusion-to-noise ratio to optimize magnetic resonance diffusion tensor acquisition strategies for improving measurements of diffusion anisotropy. *Magn Reson Med* 45: 1056-1065.

256. Kingsley PB & Monahan WG (2004) Selection of the optimum b factor for diffusion-weighted magnetic resonance imaging assessment of ischemic stroke. *Magn Reson Med* 51: 996-1001.

257. Brihuega-Moreno O, Heese FP, & Hall LD (2003) Optimization of diffusion measurements using Cramer-Rao lower bound theory and its application to articular cartilage. *Magn Reson Med* 50: 1069-1076.

258. Alexander DC & Barker GJ (2005) Optimal imaging parameters for fiber-orientation estimation in diffusion MRI. *Neuroimage* 27: 357-367.

259. Gao W, Zhu H, & Lin W (2009) A unified optimization approach for diffusion tensor imaging technique. *Neuroimage* 44: 729-741.

260. Naganawa S, *et al.* (2004) Optimization of diffusion-tensor MR imaging data acquisition parameters for brain fiber tracking using parallel imaging at 3 T. *Eur Radiol* 14: 234-238.

261. Lee JW, *et al.* (2006) Optimization of acquisition parameters of diffusion-tensor magnetic resonance imaging in the spinal cord. *Invest Radiol* 41: 553-559.

262. Andreisek G, *et al.* (2008) Diffusion tensor imaging and fiber tractography of the median nerve at 1.5T: optimization of b value. *Skeletal Radiol*.

263. Hasan KM (2007) A framework for quality control and parameter optimization in diffusion tensor imaging: theoretical analysis and validation. *Magn Reson Imaging* 25: 1196-1202.

264. Salvador R, *et al.* (2005) Formal characterization and extension of the linearized diffusion tensor model. *Hum Brain Mapp* 24: 144-155.

265. Stieltjes B, *et al.* (2003) [Diffusion tensor imaging. Theory, sequence optimization and application in Alzheimer's disease]. *Radiologe* 43: 562-565.

266. Papadakis NG, *et al.* (1999) A comparative study of acquisition schemes for diffusion tensor imaging using MRI. *J Magn Reson* 137: 67-82.

267. Skare S, Hedehus M, Moseley ME, & Li TQ (2000) Condition number as a measure of noise performance of diffusion tensor data acquisition schemes with MRI. *J Magn Reson* 147: 340-352.

268. Hasan KM, Parker DL, & Alexander AL (2001) Comparison of gradient encoding schemes for diffusion-tensor MRI. *J Magn Reson Imaging* 13: 769-780.

269. Peng H & Arfanakis K (2007) Diffusion tensor encoding schemes optimized for white matter fibers with selected orientations. *Magn Reson Imaging* 25: 147-153.

270. Rice SO (1944) Mathematical analysis of random noise. *Bell Syst Technol J* 23: 282-332.

271. Anderson AW (2001) Theoretical analysis of the effects of noise on diffusion tensor imaging. *Magn Reson Med* 46: 1174-1188.

272. Zhu HT, Zhang, H.P., Ibrahim, J.G., Peterson, B.S. (2007) Statistical analysis of diffusion tensors in diffusion-weighted magnetic resonance imaging data. *Journal of the American Statistical Association* 102: 1085-1102.

273. Callaghan PT (1991) *Principles of Magnetic Resonance Microscopy.* (Oxford Science Publications, Oxford, UK).

274. Atkinson AC, Doney, A.N. (1992) *Optimum Experimental Designs* (Oxford University Press, Oxford, U K).

275. Federov VV (1972) *Theory of Optimal Experiments* (Academic Press. , New York).

276. Kirkpatrick S, Gelatt CD, Jr., & Vecchi MP (1983) Optimization by Simulated Annealing. *Science* 220: 671-680.

277. Landman BA, *et al.* (2007) Effects of diffusion weighting schemes on the reproducibility of DTI-derived fractional anisotropy, mean diffusivity, and principal eigenvector measurements at 1.5T. *Neuroimage* 36: 1123-1138.

278. Pajevic S & Basser PJ (2003) Parametric and non-parametric statistical analysis of DT-MRI data. *J Magn Reson* 161: 1-14.

279. Wedeen VJ, *et al.* (2008) Diffusion spectrum magnetic resonance imaging (DSI) tractography of crossing fibers. *Neuroimage* 41: 1267-1277.

280. Goodlett C, Fletcher PT, Lin W, & Gerig G (2007) Quantification of measurement error in DTI: theoretical predictions and validation. *Med Image Comput Comput Assist Interv Int Conf Med Image Comput Comput Assist Interv* 10: 10-17.

281. Andersson JL (2008) Maximum a posteriori estimation of diffusion tensor parameters using a Rician noise model: why, how and but. *Neuroimage* 42: 1340-1356.

282. Papadakis NG, *et al.* (2000) Minimal gradient encoding for robust estimation of diffusion anisotropy. *Magn Reson Imaging* 18: 671-679.

283. Jones DK (2004) The effect of gradient sampling schemes on measures derived from diffusion tensor MRI: a Monte Carlo study. *Magn Reson Med* 51: 807-815.

284. Ni H, *et al.* (2006) Effects of number of diffusion gradient directions on derived diffusion tensor imaging indices in human brain. *AJNR Am J Neuroradiol* 27: 1776-1781.

285. Oouchi H, *et al.* (2007) Diffusion anisotropy measurement of brain white matter is affected by voxel size: underestimation occurs in areas with crossing fibers. *AJNR Am J Neuroradiol* 28: 1102-1106.

286. Hastings WK (1970) Monte Carlo Sampling Methods Using Markov Chains and Their Applications. *Biometika* 57: 97-109.

287. Metropolis N, Rosenbluth, A.W., Rosenbluth, M. N., Teller. A. H., Teller, E. (1953) Equations of State Calculations by Fast Computing Machines. *Jorirrlol of Cherniciil Physics* 21: 1087-1081 1092.